Bimetallic Ir-based Catalysts for Ring Opening and Hydrodesulfurization Reactions

by

Hessam Ziaeiazad

A thesis submitted in partial fulfillment of the requirements for the degree of

Doctor of Philosophy

in

Chemical Engineering

Department of Chemical and Materials Engineering

University of Alberta

Abstract

Activity, selectivity and stability enhancements often observed in bimetallic catalysts make them an inseparable part of today's chemical industry. However, it is usually problematic to understand the real interactions resulting in such improvements due to the lack of control over the bimetallic particle's surface structure. The main goal of the current thesis is to realize and explain this type of functioning, which is usually referred as synergism. A method, i.e. colloid chemistry, is applied for the preparation of catalytic materials, which allows manipulating the surface structure and enables the calculation of catalytic activity per specific surface atoms so that an explanation for bimetallic interactions is substantiated.

Refining industry is targeted for the current study, which nowadays faces significant challenges of growing demand for premium quality fuels as well as stringent environmental standards limiting the maximum allowable pollutants (like sulfur) in the final products. Two processes are discussed: ring opening (RO) of indane and hydrodesulfurization (HDS) of 4,6-dimethyldibenzothiophene (4,6-DMDBT). Due to the limited resources of Pt as well as the high demand for this metal in different areas, a Pt-free approach is applied here.

The structure-controlled synthesis of polyvinylpyrrolidone (PVP)-stabilized Ir-Pd and Ir-Ni bimetallic nanoparticles of alloy and core-shell is explained in the current thesis. Various particles in the range of $1.6 - 3.5$ nm were synthesized by the colloid chemistry method and supported on a weak acidic material, i.e. γ-Al_2O_3. The nanoparticles and supported catalysts were characterized by several techniques including TEM, UV-vis spectroscopy, TPR, XPS, CO-DRIFTS, ISS, CO chemisorption, XANES and CO_2-TPD,

which verified the formation of new bimetallic particles and showed structural differences between the catalysts of alloy and core-shell structures.

Removal of PVP residues from the surface of supported catalysts was studied thermally by calcining the samples under air. Only part of the PVP remnants was removed after calcination at $200^{o}C$, while treatment at $400^{o}C$ completely eliminated all the residual polymers. Minor structural changes as well as sintering and size increase of samples with Pd or Ni enriched surfaces occurred at $400^{o}C$.

The catalytic activity of supported Ir-Pd and Ir-Ni catalysts was studied in ring opening of indane at $336^{o}C$ and atmospheric pressure. Monometallic Ni or Pd showed insignificant activity, whereas enhancement of activity was observed for bimetallic catalysts compared to monometallic Ir. However, calculating activity values per surface atoms revealed no intrinsic changes in catalytic behaviour of Ir atoms, which indicates the role of Pd or Ni as only being the surface diluent in bimetallic alloys or the dispersing agent in core-shell catalysts, providing a 100% surface coverage for Ir. Having investigated the effect of PVP residues on catalytic activity of Ir-Pd catalysts for the SRO of indane, a more pronounced activity improvement was observed after the complete removal of PVP from Pd-rich samples, an effect that was sluggish though for Ir-rich ones.

Furthermore, the HDS of 4,6-DMDBT was studied over Ir-Pd catalysts at $300^{o}C$ and 5 MPa. Providing the necessary hydrogenation properties, monometallic Pd suffered from severe sintering after $400^{o}C$ calcination, which dramatically reduced its dispersion. Addition of Ir enhanced the activity and selectivity toward sulfur-free products, also improved the selectivity contribution of the direct desulfurization (DDS) pathway by five times because of its proven hydrogenolysis tendency. Similar calculations for finding the

activity values per surface atoms indicated the superior performance of bimetallic Ir-Pd catalysts to be a consequence of the observed synergism and not the significant changes in the intrinsic behaviour of Pd atoms. This means that Ir has helped to disperse Pd atoms and prevented and/or reduced their agglomeration. The high pressure hydrogenation of indane at 280-320°C and 5 MPa was also briefly studied, where the addition of Ir similarly improved the activity of Pd catalysts. However, when a mixture of indane and 4,6-DMDBT was fed to the system, the hydroconversion behaviour of bimetallic Ir-Pd catalysts was manipulated by the HDS of 4,6-DMDBT, an insignificant conversion was observed for hydrogenation of indane. The catalyst stability was studied for 3 days under a mixture containing 300 ppm sulfur as 4,6-DMDBT.

Preface

The Materials presented in the current thesis are part of the research project, which has been funded by Imperial Oil – Alberta Ingenuity Institute for Oil Sands Innovation (IOSI) at the University of Alberta.

The introduction and background information provided in chapter 1 is my own work. Chapter 2 of the thesis has been published as: H. Ziaei-Azad, C.-X. Yin, J. Shen, Y. Hu, D. Karpuzov and N. Semagina, "Size- and structure-controlled mono- and bimetallic Ir-Pd nanoparticles in selective ring opening of indan", *Journal of Catalysis* 300 (2013) 113–124. Dr. Cindy-Xing Yin collected TEM images and assisted with XANES analysis. Mrs. Jing Shen performed synthesis and TEM, UV-vis and AAS analyses, and collected the reaction data, that were also reported in her M.Sc. thesis "Bimetallic catalysts for low-pressure ring opening", University of Alberta (2011). Dr. Yongfeng Hu performed XANES and helped me with data analysis. Dr. Dimitre Karpuzov performed XPS and ISS and helped me with data analysis. NAA analysis was performed by Becquerel Laboratories Inc. Ontario, and STEM–EDX analysis was completed by the Department of Chemistry, University of Toronto. The rest of data collection, analysis and interpretation of the results as well as writing the manuscript are my own work.

Chapter 3 of the thesis has been published as: Hessam Ziaei-Azad and Natalia Semagina, "Bimetallic catalysts: requirements for stabilizing PVP removal depend on the surface composition", *Journal of Applied Catalysis A: General* 482 (2014) 327–335. NAA analysis has been performed by University of Alberta, SLOWPOKE facility. The rest of the work is mine.

Chapter 4 of the thesis has been published as: Hessam Ziaei-Azad, and Natalia Semagina, "Nickel boosts ring opening activity of iridium", *ChemCatChem* 6 (2014) 885–894. NAA analysis was done by University of Alberta, SLOWPOKE facility, and XPS was performed by Alberta Center for Surface Science and Engineering (ACSES). The rest of data collection and interpretation as well as writing the paper are my own original work.

Chapter 5 of the thesis includes using a high pressure device that was built in collaboration with Dr. Long Wu. NAA analysis was performed by University of Alberta, SLOWPOKE facility. Mr. Les Dean performed programming of the lab view software to communicate with the HDS system and helped in proper operation of electrical parts. Mr. Walter Boddez also helped with electrical issues. Mrs. Jing Shen helped with the maintenance of GC and Mr. Harshal Goyal assisted in BET and pore size distribution analyses. Dr. Xiaoli Tan and Mr. Jeremiah Bryksa helped with CHN analysis. The rest of the work is mine.

Dr. Natalia Semagina, my PhD program supervisor, provided the feedback for conducting all the experiments, supervised the process of data collection and interpretation, and performed the final revising of all publications and writings indicated above.

Dedication

To my lovely *Mom* and *Dad* and to my sweet sister *Sadaf*

Acknowledgements

I would have not been able to complete this thesis without the help and contribution of many people. First and foremost, I would like to express the deepest gratitude to my supervisor, Dr. Natalia Semagina, who gave me the opportunity to join her group, provided me with the chance of trying my own ideas and offered me endless care and support during my PhD program.

Secondly, I would like to thank Dr. Long Wu for his help to improve our low pressure ring opening device as well as his great contribution in building the high pressure HDS system.

Next, I would like to thank my colleague and friend, Mrs. Jing Shen, whom I spent the past four years with doing research as a team and shared so many great moments.

I am also indebted to many others, including:

Dr. Xuejun Sun and all his colleagues at Alberta Cross-Cancer Institute for helping with TEM analysis.

Members at the Institute for Oil Sands Innovations (IOSI) at University of Alberta: Dr. Xiaoli Tan, Mr. Jeremiah Bryksa and Mrs. Lisa Brandt for their constant support, trainings provided and facilitating the use of various resources I worked with.

Dr. Dimitre Karpuzov and his colleagues (Dr. Anquang He and Mr. Shihong Xu) at Alberta Centre for Surface Engineering and Science for doing the XPS and ISS analyses.

Dr. Yongfeng Hu at Canadian Light Source Inc. in Saskatoon for doing XANES analysis.

Dr. John Duke at the University of Alberta SLOWPOKE facility for performing NAA analysis.

Table of Contents

List of Tables

Lists of Figures or Illustrations

List of abbreviations

AAS	Atomic absorption spectroscopy
AL	Alloy
BET	Brunauer-Emmett-Teller
BJH	Barrett-Joyner-Halenda
C (c)	Core
C/S (c/s)	Core-shell
DBT	Dibenzothiophene
DDS	Direct desulfurization
DMBCH	Dimethylbicyclohexyl
DMBP	Dimethylbiphenyl
DMCHB	Dimethylcyclohexylbenzene
DMDBT	Dimethyldibenzothiophene
DMHHDBT	Dimethylhexahydrodibenzothiophene
DMPHDBT	Dimethylperhydrodibenzothiophene
DMTHDBT	Dimethyltetrahydrodibenzothiophene
DRIFTS	Diffuse reflectance infrared Fourier transform spectroscopy
EDX	Energy-dispersive X-ray
EG	Ethylene glycol
ET	Ethyltoluene
EXAFS	Extended X-ray absorption fine structure spectroscopy
fcc	Face-centered cubic
FID	Flame ionization detector

GC	Gas chromatography
HDS	Hydrodesulfurization
HYD	hydrogenation
ISS	Ion scattering spectroscopy
MCP	Methylcyclopentane
NAA	Neutron activation analysis
PAH	Polycyclic aromatic hydrocarbons
PB	Propylbenzene
PVP	Poly-(vinylpyrrolidone)
RO	Ring opening
S (s)	Shell
SRO	Selective ring opening
SSA	Specific surface area
STEM	Scanning transmission electron microscopy
TEM	Transmission electron microscopy
TGA	Thermogravimetric analysis
TOF	Turnover frequency
TPD	Temperature programmed desorption
TPR	Temperature programmed reduction
UV	Ultra-Violet
WHSV	Weight hourly space velocity
XANES	X-ray absorption near edge structure
XPS	X-ray photoelectron spectroscopy

Chapter 1: Introduction

1.1. Background and hypothesis

We are living a modern life. Technological improvements are finding their way into every facet of our lives, providing us with the experience of an easier and more comfortable life than our ancestors have lived. Twentieth century must have seen the highest technological improvements of all time in human history; an endless appetite for creativity, novelty and progress that nothing, even two world wars, could stop it. But, the reality is that we are spending of one big pocket, the Earth, and world's resources are being depleted every year, yet some of them could not replenish themselves to the original condition. At the same time, we have started paying more attention to our environment, partly because of itself, also because we have realized that environmental issues are returning to ourselves as health threats. The recent years have been the time to ask for the creativity, economical thinking combined with practicality, as well as the time to regulate the activities that threaten sustainability.

Internal combustion engines are still the main source of transportation and it is not predicted to be significantly replaced in the coming years [1]. On the other hand, environmental standards are being regulated everywhere around world and becoming tighter to control the emissions from these engines. For example, for a diesel fuel to be used in road transportation in several developed countries, it needs to have a minimum cetane number of 51, less than 11% of polyaromatics and the maximum sulfur level of 10 ppm [2,3]. In addition, after several years of extraction and refining of crude oil resources, the remaining oil has become poorer in quality, which has brought new challenges to refining industry [4]. Nowadays, refiners are facing the increasing demand of premium

quality transportation fuels on one side and the necessity for new upgrading technologies to effectively deal with current crude oils on the other side. Such technologies target two classes of processes: i) those adding more final products into the transportation fuel blends and ii) those that aim at increasing the quality of these blends. Among the several processes that fit in either class, two catalytic processes are concerned in the current thesis: selective ring opening and deep hydrodesulfurization.

On the other hand, the area of catalysis has been improving during the past decades, trying to benefit from the progresses in other fields such as nanotechnology and advanced materials to utilize the knowledge for building more efficient catalysts. One of such improvements is the synthesis of materials with controlled structures. Owing to the nanotechnology based technique of colloid chemistry, it has become possible to prepare bimetallic nanoparticles with different structures in solution and deposit them on support materials to synthesize supported catalysts. The current thesis applies such a technique to prepare a series of bimetallic catalysts to be studied in the reactions mentioned above. As opposed to the traditional methods like impregnation, the current technique allows one to realize the bimetallic functioning and the interactions (synergism) happening between metals.

Our hypothesis for the current thesis is that the synergism (bimetallic interactions), which is usually discussed for bimetallic catalysts can only be observed by changes occurring in activity or selectivity values; however, the explanation and indication of the reasons responsible for these changes such as electronic or geometric factors may be achieved only by careful calculation of activities based on the catalyst's surface structure.

According to what mentioned above, a number of topics including: supported bimetallic catalysts, structure-controlled synthesis of nanoparticles with colloid chemistry, catalytic selective ring opening and deep hydrodesulfurization reactions are going to be discussed in the current thesis. Therefore, a brief overview about each topic is provided in the rest of this chapter to provide the reader with some background information required.

1.2. Supported bimetallic catalysts in chemical industry

Since the very primitive application of Pt wires in the development of miners' safety lamps by Humphrey Davy in 1817 [5], the field of heterogeneous catalysis has gone through significant advancements. The idea of alloying two metals, whether or not they are both active, is one of the major breakthroughs that the heterogeneous catalysis has benefited from. Systematic studies on alloys coined during the years between the first and second world wars [6]; however, it was in 1960s, when the alloyed catalysts received the first significant commercial interest for their use in hydrocarbon reforming units [7], and it was John Sinfelt, who introduced the term "bimetallic" catalysts as a better substitute for the classical alloy term [8].

Bimetallic catalysts play a distinctive role in today's chemical industry [9]. They are a new class of catalytic materials with different and usually enhanced activity, stability and selectivity compared to their monometallic counter parts [7]. Addition of a second metal like Au, Ag, Cu or Pb to Pd for selective hydrogenation processes, or the modification of reforming Pt-based catalysts by Ir and Re are few examples regarding the vast industrial application of the bimetallic catalysts [10-12]. Classically, electronic and geometric effects and sometimes the occurrence of new sites are suggested as the main reasons for changes happening in bimetallic catalysts [6]. Electronic effects are quite

common and typically described as the charge transfer and/or redistribution happening between two metals, which can affect the mode and the strength of adsorption on the catalyst surface that alter the catalytic properties. Geometric factors concern the way surface atoms are positioned in a bimetallic structure, and sometimes result in enrichment or dilution of one species on surface sites. And mixed sites are described as new active sites with improved properties compared to those of the pure metals [6].

Traditionally, heterogeneous catalysts are prepared by the direct addition of metallic precursors to supports materials using techniques such as impregnation or precipitation [13,14], which is still widely used in chemical industries [15]. However, since the formation of metallic species takes place on the support material, interactions between particles and support affect the formation and growth process [16]. This usually leads to a poor control over particle size as well as the close vicinity between metals, resulting in a family of mono- and bimetallic particles of inhomogeneous composition to coexist on the surface [6]. At such conditions, the surface of a bimetallic catalyst is barely known, which makes it difficult to precisely understand the interaction(s) that alter the catalytic behaviour. However, if one knows the surface composition, the metal functioning can be described and it will help to explain the bimetallic interactions (sometimes referred as synergism). This way, it will be possible to design the desired structure, which yields the optimum catalytic behaviour for any specific reaction. The comparison between impregnation method and structured-controlled technique for the synthesis of supported catalysts is presented in Figure 1.1.
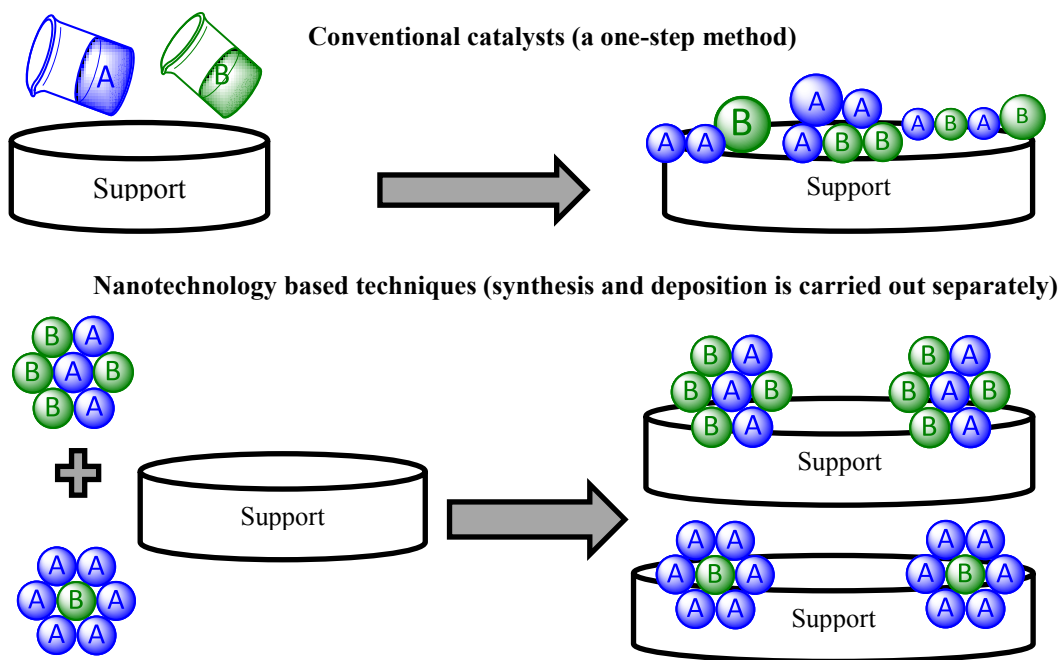
Figure 1.1. A schematic representation of impregnation and nanotechnology based techniques in synthesis of bimetallic supported catalysts.

1.3. Structure-controlled synthesis of nanoparticles for catalytic applications

According to what mentioned above, there is a growing interest in bimetallic catalysts with a robust control on their structure for catalytic applications. Several recent attentions have been devoted to the colloid chemistry based techniques for the synthesis of mono- and bimetallic nanoparticles, where an extensive and detailed study can be found in literature [17]. These methods, which initially utilized for the synthesis of monometallic nanoparticles of different size and shapes [18], soon found their way in the formation of structured bimetallic nanoparticles [19-21]. The chance of synthesizing a bimetallic particle with desired structure in separate step(s) and then deposit it on a supporting material, may account as one of the most important advantages of this technique over the traditional methods [16].

1.3.1. Colloid chemistry for the synthesis of metallic nanoparticles

Colloid chemistry is categorized under the "bottom up" techniques for the synthesis of nanomaterials. It is a wet method of synthesis, which relies on the reduction of metallic precursor(s) in the presence of a protecting agent to make zero-valent metallic colloids [22]. Historically, the first study concerning the synthesis of a metallic colloid in the presence of a stabilizer dates back to the work of Faraday in 1857 for the synthesis of gold particles [22]. However, the first standard reproducible procedure for the preparation of metallic colloids was reported by Turkevich in early 1950s in the synthesis of 20 nm gold particles, which is still valid in essence by today [23]. This procedure follows a nucleation and growth trend, where initial nuclei of 13 metal atoms are formed irreversibly by reaching the supersaturation concentration, and is further followed by the diffusion-controlled growth process of the remaining metallic atoms that are taken up by the existing nuclei in the solution [22]. The resulting metallic colloids have the ability to be redispersed in water or organic solvents; therefore either of them (or both) can be used as the solvent medium. The reduction is achieved by a liquid or a solid reducing agent, depending on the type of metallic precursor that is being reduced [24].

Alcohols are among the frequently used reducing materials, where several literatures report the utilization of alcohol reduction method for the synthesis of mono- and/or bimetallic nanoparticles [25-30]. During the course of reduction, an alcohol with α-hydrogen atoms is oxidized to the corresponding aldehyde and provides the required electrons for reduction of metallic ions [22]. Since the metallic colloids are solvable in alcohols, alcohols can act as a double agent providing the dissolving and reducing media for the synthesis of metallic colloids. In such a situation, they can be used separately or

together with water depending on the type of reducing medium desired. Different types of alcohols with either one OH group (like methanol or ethanol) or those with various OH functions (i.e. polyols such as ethylene glycol) have been reported in literature [31,32]. Studies on how an alcohol type, structure and/or quantity can affect the size of resulting particles can be found elsewhere [31-33]; however, as a general rule of thumb smaller sized particles are favoured by stronger alcohols and/or with those of higher boiling points. Based on that, the alcohol reduction technique is usually practiced by refluxing the synthesis mixture at the alcohol's boiling point for a faster reduction and a smaller particle size [22].

The use of solid reducing agents, mainly sodium citrate, $NaBH_4$, or KBH_4 has also been reported in literature [34-37]. The use of these reducing agents has been increased recently for the reduction of non-noble metal ions such as Ni, which are resistive to reduction by alcohols [38,39].

Stabilizers are the other ingredients for the synthesis of nanoparticles by colloid chemistry. Nanoparticles possess a huge external surface area owing to their small particle sizes, and thereby having an excess surface free energy, which make them thermodynamically unstable and highly potential to coagulate. Stabilizers prevent this agglomeration by exerting repulsive electrostatic and/or steric forces to prevail the attractive van der Waals forces [22]. Different materials have been studied as stabilizing agents for the synthesis of nanoparticles. They are usually categorized as: electrostatic, steric, electrosteric, ligand and solvent stabilizers [22]. In the current thesis the steric stabilization is used for the synthesis of nanoparticles. This type of stabilization is provided by large organic molecules like polymers that can adsorb to the surface of nanoparticles

[40]. Polymers are reported to form several weak bonding with a nanoparticle's surface rather than making strong bonds at specific locations [22]. Figure 1.2 presents two major families of polymers that are used for stabilization purpose: poly-(N-vinyl-2-pyrrolidone) (PVP) and poly-(phenylene oxide) (PPO).

Apart from the protecting role, the use of stabilizers affects the particle size and the surface accessibility of the resulting nanoparticles, which are determining factors for catalytic behaviours. Size effects happening by varying the amount of a stabilizer (like PVP) is less pronounced in making huge particle size changes during the alcohol reduction method compared to altering the reduction temperature or the type of alcohol that is being used [31]. In such cases, a threshold ratio of stabilizer to metal that ensures the prevention of nanoparticles from agglomeration is good, where above that ratio sizes are generally decreased by increasing the amount of stabilizer [32]. For instance, in the synthesis of Ru nanoparticles, a 5.5 nm difference is reported by varying the reduction temperature from 160 to 285°C (using different polyols). However changing the ratio of PVP to metal by 50 times (at a constant temperature) causes an only 2 nm size difference [31].

PVP
poly(vinylpyrrolidone)

PPO
poly(2,5-dimethylphenylene oxide)
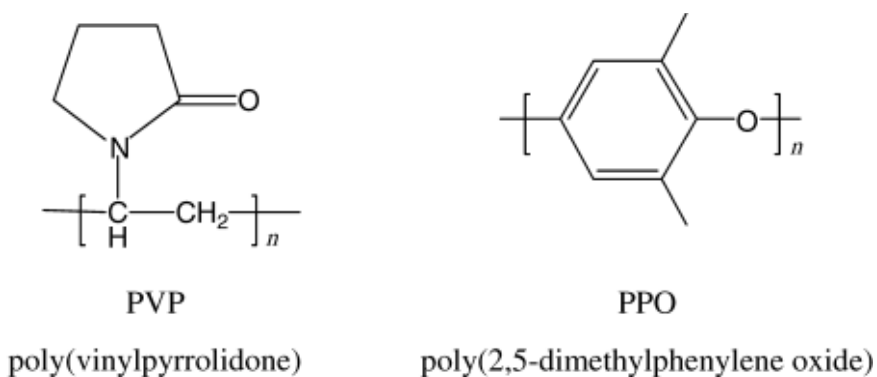
Figure 1.2. Schematic structure of PVP and PPO polymeric stabilizers. Reprinted from [41] with permission of John Wiley and Sons (© 2005 WILEY-VCH Verlag GmbH & Co. KGaA, Weinheim).

Poly(N-vinyl-2-pyrrolidone), or PVP, is used through the current thesis for the synthesis of mono- and bimetallic nanoparticles. PVP is a water-soluble amine-based polymer, which has been studied in the synthesis of several monometallic nanoparticles like: Au, Pd, Ru, Pt and Ni [31-33,42,43], as well as bimetallic ones such as PdPt, NiPt, AuPd, PtCu, NiPd and RuIr [26,44-47].

Synthesized nanoparticles can be precipitated from the solution by using a chemical like acetone [31]. This way it is possible to deposit them on a support material after the synthesis by leaving the mixture of support, nanoparticles and acetone to stir for a while (typically 1-2 h), which is later followed by removal of the supernate solution and drying the resulting supported catalysts. A schematic view of the synthesis of nanoparticles by the colloid chemistry is observed in Figure 1.3.

Metal Precursor(s)
+
Solvent and
reducing agent
+

PVP

Heat and vigorous stirring

Nucleation
and growth

PVP-stabilized
nanoparticles

Deposition of nanoparticles
on g-Al$_2$O$_3$ with acetone

Step 1: Synthesis of polymer-stabilized nanoparticles by alcohol
reduction technique

Step 2: preparation of
supported catalysts
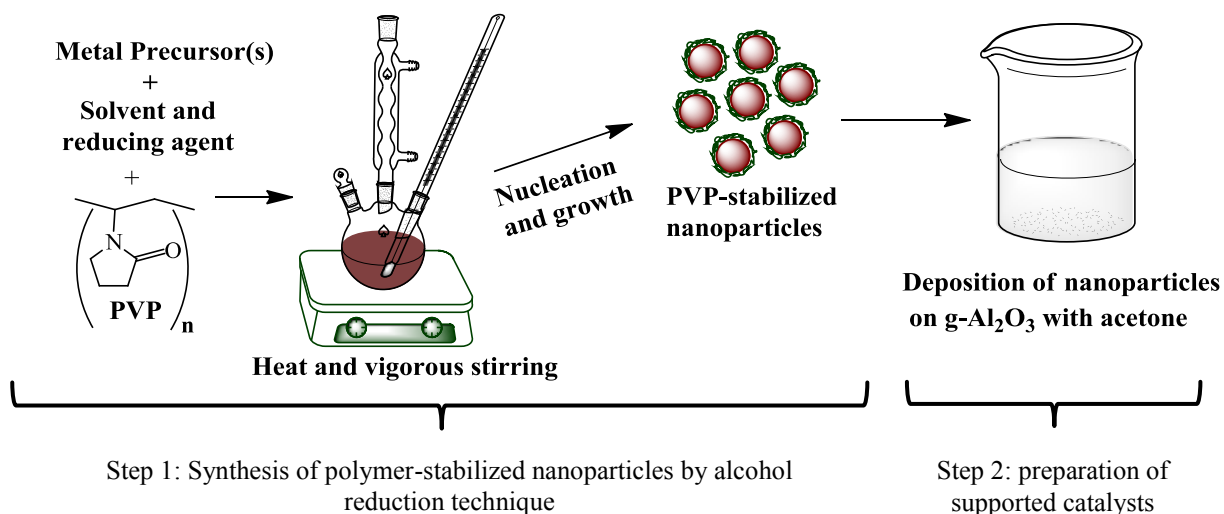
Figure 1.3. Schematic presentation of nanoparticles formation, and deposition on the support material with acetone.

1.3.2. Structure-controlled synthesis of bimetallic nanoparticles

In addition to the synthesis of monometallic nanoparticles, colloid chemistry can be applied to prepare bimetallic nanoparticles in solution. Colloidal techniques like alcohol

reduction provide a robust control over the synthesis of bimetallic particles and one can control the structure of bimetallic particles forming in solution before depositing them on to the support material, which is one of the most interesting advantages of this technique. Two types of bimetallic structures are usually studied, which differ in terms of atoms positioning: "random alloy" or just "alloy" structure having a random position of metallic atoms within the structure, and "core-shell" structure, typically referred to the layered positioning of one metallic atom on top of the particles of another metal [24]. These types of structures are schematically presented in Figure 1.4.
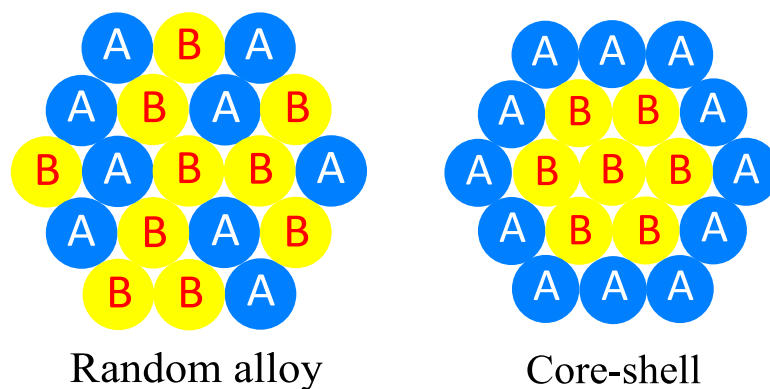
Figure 1.4. Possible structures of bimetallic nanoparticles synthesized by colloidal methods.

The simultaneous (co-) reduction of metallic precursors is the typical way of preparing the random alloy bimetallic nanoparticles. In this procedure, both metallic precursors are reduced at the same time. Metals may catalyze the reduction of each other in this method. Particles may also form a layered (core-shell) structure via the simultaneous reduction. This usually occurs when the reduction takes place under a mild condition and/or when there is a significant difference between the redox potential of the metals being reduced [19]. In simultaneous reduction, the metal with higher redox potential is reduced first and forms a core, where the second metal one with lower redox potential

build a layer (i.e. a shell) on top of this already formed core. Several bimetallic nanoparticles with alloy type structures have been prepared and studied for different catalytic processes. Examples include: NiIr and RuPt for hydrogen generation [48,49], AuPd and AgAu for CO oxidation [50,51], NiPd, PtPd, RuPd, PdM (M = Pt, Zn and Au) and CuPd in hydrogenation reactions [19,20,28,45,52-55], AgAu, AuPd and NiPt for reduction reactions [56-58], FePt and FeRu in studies of single-walled carbon nanotubes [59], and AuPt and NiPt for electro-oxidation reactions [60,61].

As mentioned above, formation of core-shell bimetallic particles is possible with the simultaneous reduction of metallic precursors. However, the idea of using a core-shell structure is usually to save a more active metal on surface positions and builds the core with a less active and possibly a cheap metal. In most cases, such formulations include using a noble or a more expensive metal with a higher redox potential in shell positions, which is not favoured during the simultaneous reduction, as the metal with a higher redox potential tends to reduce first and enrich the core. To overcome this mechanistic contradiction, a successive reduction of metallic precursors is typically practiced. However, successive reduction is not enough by itself, because as soon as the metallic ions with a higher redox potential come in contact with metallic nanoparticles of the lower redox potential, the oxidation of the latter is likely to happen in expense of the reduction of the former [24]. To overcome this phenomenon, a slightly modified version of successive reduction is usually used, which is known as hydrogen sacrificial (protective) reduction method. This technique utilizes hydrogen for treating the already formed core particles in solution to form metal hydrides [26]. Several noble metals and non-noble transition metals have the ability to dissociate hydrogen and forming metal hydrides in solution [26,62].

Hydrides species can provide the required electron for the reduction of second metallic ions (with typically higher redox potential) and prevent the oxidation of already formed particles. A schematic view of hydrogen sacrificial reduction method is presented in Figure 1.5. Different bimetallic nanoparticles with controllable core-shell structures have been synthesized and studied in catalytic reactions; examples include: Ni/Pt and Ni/Pd as catalyst for fuel cell applications [63,64], Pd/Pt for methane combustion [65], M/Pt (M = Ru, Rh, Ir, Pd or Au) for preferential oxidation of CO in hydrogen streams [66], Ni/Pd, Au/Pd, Pd/Pt and Ag/Pd for hydrogenation [21,67-70] and Pt/Sn for aromatization reaction [71].
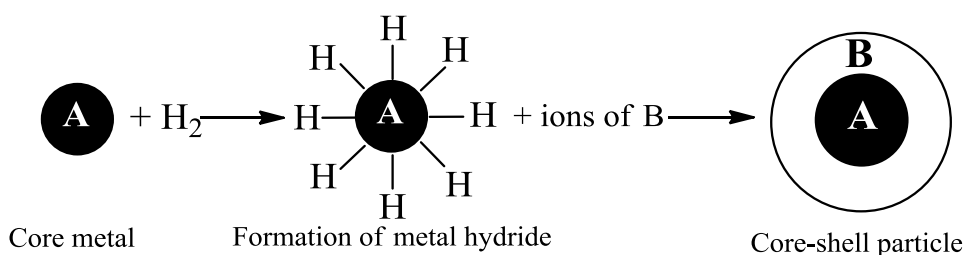
Figure 1.5. Schematic presentation of hydrogen sacrificial reduction method for synthesis of core-shell nanoparticles.

It is clarified here that the above mentioned structures are the ideal possible forms. However, in practice one may achieve structures in between like alloys without homogenous surface distribution of metals (i.e. surface enrichment with one species) or core-shell particles with an incomplete shell (i.e. using less amount of the second metal that is required for forming a full shell); also changes in structure may happen after the deposition of nanoparticles on the support material and/or during the thermal treatments and/or catalytic reactions. Consequently, a detailed characterization of nanoparticles at different stages (i.e. as-prepared, supported and after reaction) is required, when trying to

correlate the catalytic activity with bimetallic structure and calculating parameters activity numbers per surface atoms.

1.3.3. Polymeric stabilizers and heterogeneous catalysis

As mentioned earlier in section 1.3.1, stabilizers serve during the colloidal synthesis to prevent the agglomeration and size increase of nanoparticles forming in the solution. However, their role is finished for heterogeneous catalysis as soon as the synthesis is completed. In fact, further presence of stabilizers on supported catalysts brings the challenge of surface accessibility of metallic centers, which is usually detrimental for catalytic activity in heterogeneous reactions [72,73]. It is reported that about 50-70% of nanoparticles' surface is still covered with stabilizers after the colloidal synthesis [74]. A study on PVP-stabilized Pt nanoparticles showed up to 4 nm differences in Pt particle sizes measured by chemisorption and XRD techniques, where the former method was affected by the stabilizer left overs [42]. Therefore, removal of the remaining stabilizer is necessary for cleaning the surface of metallic centers in a supported catalyst. Various techniques including thermal treatment [75-77], irradiation [78], chemical treatment [79,80], UV-ozone treatment [81,82] and plasma treatment [83,84] have been studied in literature for the removal of stabilizing agents. Among them, thermal treatment has been utilized more frequently [16], where the oxidative removal of stabilizers (usually as CO_2 and H_2O) has been found to be most effective [85]. However, oxidative treatment is not always favoured since a reduced active metal is desired for some reactions. In those occasions, a further thermal treatment under a reductive atmosphere is also required after the stabilizer removal. Thermal treatments may practice under an inert or a reductive atmosphere depending on the nature of metal(s) and the catalytic reaction that is being studied, which would require a

13

different temperature to reach the same stabilizer removal. For instance, the oxidative decomposition of PVP begins at about 330°C in air, while it will happen at 100-120°C higher under nitrogen [86]. Also, the presence of a metal can catalyze the removal of a stabilizer. The removal of PVP from PVP-stabilized Pt nanoparticles is reported to happen 130°C lower under air than its non-catalyzed removal; the reason is attributed to the enhanced catalytic dissociation of oxygen on clean Pt surface sites [75]. Furthermore, stabilizer removal by thermal treatments often demands moderate to high temperatures, which may result in destabilization of metallic particles and/or structural changes [87]. Metal oxides usually have lower melting points compared to their metallic counterparts, and processes like sintering may be favoured as the nanoparticles lose the stabilizer protection during the treatment [16]. Consequently, the thermal removal of a stabilizer from a supported catalyst needs to be considered as a trade-off between the level of surface cleaning and the possible size and structural changes.

Last but not the least about stabilizers, some recent studies, mainly focused on non-polymeric stabilizers (i.e. dodecyl amine, $C_{12}H_{25}NH_2$), have found advantages for leaving the stabilizers on supported catalysts [16]. Benefits like: protection of nanoparticles' surface from oxidation [88], modifying the metal-support interactions [89], agglomeration prevention at high metal loadings [16] and a better anchoring of nanoparticles on support materials [90] are among those positive effects reported.

1.4. Ring opening (RO) reactions over metal supported catalysts

As mentioned in section 1.1, selective ring opening (SRO) of naphthenic molecules is one of the possible reactions for upgrading purposes, which is studied in the current thesis. During the SRO, an endocyclic C-C bond of a naphthenic ring is cleaved only once

thus retaining the same molecular weight in the products as that of the reacting molecule [91]. Ring opening of naphthenic molecules results in volume increase (density reduction), which is favourable for oil market. Also, it can contribute to cetane number improvement; however the opening needs to occur at substituted carbon positions (i.e. selective) to avoid branching increase [92].

Ring opening on metal supported catalysts is a metal(s)-driven chemistry, which is carried out by hydrogenolysis. The role of support is usually limited to skeletal isomerization of rings with more than five carbons (ring contraction), since the activity of metals for opening of those rings is reduced noticeably. Therefore, those supports having a low to moderate acidity are favoured; where those of the high acidity like zeolites promote the excessive cracking of side chains and/or alkane products, and present a low yield of RO [91]. Various metals including noble metals (Pt, Ir, Pd, Rh and Ru) as well as other transition metals such as Ni, Cu, Ag, Os and Re have been studied in the RO of naphthenic rings [4,91,93-102]. Literature is quite unanimous about the superior activity of Ir among the other metals for RO reactions [93,98,100].

Three mechanisms, mostly differ in the chemisorption mode of the reacting molecule, have been proposed for the RO over supported catalysts: i) dicarbene, ii) π-adsorbed olefin and iii) metallocyclobutane [104]. A schematic picture of these mechanisms is depicted in Figure 1.6. Dicarbene mode involves the perpendicular adsorption of two carbon atoms on a metal surface, resulting in the cleavage of unsubstituted secondary-secondary carbon atoms, whereas the π-adsorbed olefin mechanism requires the flat adsorption of three neighbouring carbon atoms, and yields to the cleavage of C-C bonds at substituted positions. The metallocyclobutane is another

alternate mechanism, involving a metal and four carbon atoms, which is capable of RO at substituted C-C positions if an external methyl group is involved in the intermediate. The latter mechanism usually competes with dicarbene; however it has a higher activation energy and is favoured only when the dicarbene path is blocked [104].

(I) Dicarbene
mode

(II) π- Adsorbed
olefin mode

(III) Metallocyclobutane
mode
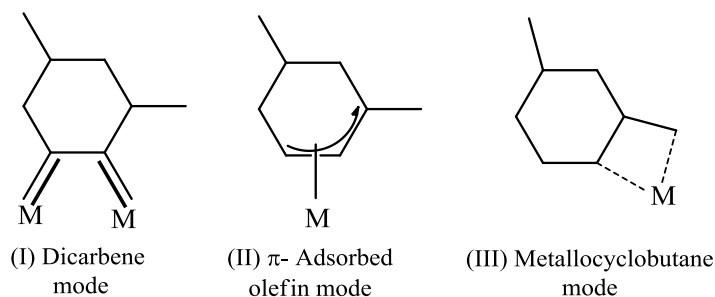
Figure 1.6. A schematic representation of possible reaction mechanisms for ring opening reaction. Reprinted from [104] with permission from Elsevier.

Nature of the metals being used is a major parameter affecting the mechanism by which the RO takes place. Metals like Ir, Ru and Rh as well as bimetallic compounds such as Pt-Ir, Pt-Co, Pt-Mo and Pt-Ru favour the RO at unsubstituted positions, while others such as: Pt, Pd and Ni as well as others such as Pt-Pd, Pt-Ni and Pt-W show tendency for the cleavage at substituted positions [93]. However, other parameters can affect the mechanistic tendency and/or the catalytic activity of a metal. Size is an important factor; RO of methylcyclopentane (MCP) over Pt is well-known for size sensitivity. Particles with sizes below 2 nm are capable of cleavage at substituted and unsubstituted C-C bonds (referred as statistical distribution), while larger sized particles promote the RO only at substituted positions [96]. Elsewhere, the activity of Ru particles for the SRO of methylcyclohexane (MCH) was found to be higher on larger particles (3 nm) than smaller ones (1.2 nm) [97]. Literature on RO is rich with case studies investigating the effects of different parameters on the activity or selectivity of metals these reactions. Examples of

such parameters include: loading of the active metal, blockage or poisoning of active sites and/or the type of support, which can be found elsewhere [95,98,105].

The current thesis deals with the ring opening of benzocyclopentane (also known as indane, C_9H_{10}) as the model compound of RO studies. There are several reported studies on relatively small molecules like MCP (boiling point: 72°C), which are quite far from components of diesel cut [94,95,106,107]. Indane with a benzene ring attached to its five membered naphthenic ring stands as a more representative molecule to heavier blends than a small one like MCP. The reaction pathway in the hydrogenolysis of indane has been studied previously using a series of Pt-Ir supported catalysts [4,108]. We found and confirmed the same products when studying the RO of indane at atmospheric pressure [109]. A schematic view of such reaction pathway is presented in Figure 1.7. It is observed that the reaction can follow either α or β paths, the former results in opening at substituted and the latter at unsubstituted positions. Based on that, the possible ring opening products one can obtain are n-propylbenzene and 2-ethyltoluene. Further ring opening results in cleavage of more C-C bonds and reduces the molecular weight that is not favoured in ring opening. Thus, the selective ring opening term, here refers to the production of n-propylbenzene and 2-ethyltoluene as opposed to the other possible products.
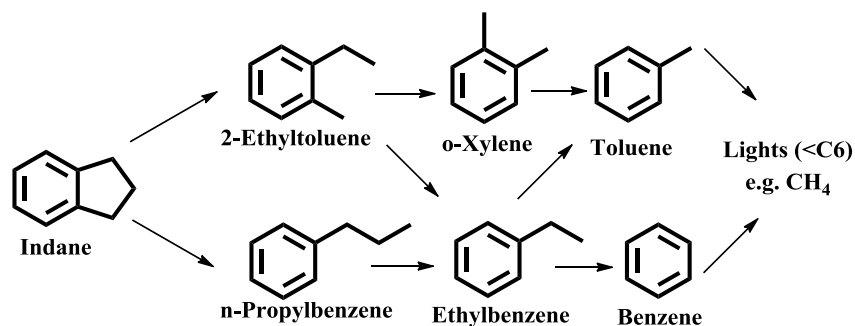
Figure 1.7. Reaction pathway for the ring opening of indane at atmospheric pressure. Reprinted from [4] with permission from Elsevier.

In addition to the SRO of indane at atmospheric pressure, the high pressure hydrogenation of this model compound was also briefly discussed in literature. At high pressures, however, the reaction is favoured toward hydrogenation into hexahydroindane (C_9H_{16}) and not to the SRO products [108].

1.5. Deep hydrodesulfurization (HDS) with metal supported catalysts

Deep HDS is the other catalytic reaction that is studied in the current thesis to evaluate the catalytic activity of the synthesized catalysts. As mentioned in section 1.1, the environmental standards are becoming more stringent and the sulfur reduction at such levels mainly deals with the elimination of refractory sulfurous compounds [110]. Thus, when it comes to the removal of the very enduring sulfurous molecules, also referred to deep and ultra-deep HDS, an appropriate choice of a model compound that reasonably represents the real pool becomes important.

The existing sulfur in oil fractions is divided into two categories of non-heterocyclic and heterocyclic. The former includes thiols, sulfides and disulfides, while the latter mainly contains thiophenes of different aromatic rings and their alkyl- or aryl-substituted derivatives. The sulfur of heavier fractions mostly contains thiophenic rings, which is more difficult to be removed compared to the non-heterocyclic sulfur. Generally speaking, it is reported that the reactivity of the thiophenic sulfur reduces in the form of: thiophene > alkylated thiophenes > benzothiophenes > alkylated benzithiophenes > dibenzothiophene (DBT) and alkylated DBTs without substituents at positions 4 and 6 > alkylated DBTs with one substituent at either position 4 or 6 > alkylated DBTs with substituents at positions 4 and 6 [111-113]. Thus, a dibenzothiophene with alkyl derivatives at 4 and 6 positions is among the most refractory molecules and is a good

candidate for deep HDS studies. Based on that, 4,6-dimethyldibenzothiophene (i.e. 4,6-DMDBT) is selected as the model compound in the current thesis.

A large amount of literature has been published on HDS mechanism of DBTs and its alkylated derivatives. Two reaction pathways are suggested for this process: i) direct desulfurization (DDS), the path of direct hydrogenolysis of a C–S bond of the reacting molecule, which results in the formation of sulfur-free aromatic products and ii) hydrogenation (HYD), the path relying on the initial hydrogenation of an aromatic ring before sulfur removal, which goes through a mixture of sulfurous intermediates as well as sulfur-free aromatic and/or saturated products [114-119]. From the chemisorption point of view, DDS requires a perpendicular adsorption of the reacting molecule (i.e. σ mode) [120,121], while HYD is carried out after a parallel bonding of the reactant on the catalytic surface (i.e. π mode) [121,122]. Unlike DBT with a preference for DDS than HYD, the HDS of 4,6-DMDBT is mostly achieved via the HYD route, since the presence of methyl groups adjacent to the sulfur atom pose a steric hindrance toward the perpendicular adsorption of DMDBT on the surface and the DDS contribution for the HDS of DMDBT is limited [120,121]. This makes it very important for choosing a metal with a strong hydrogenation ability for catalysis of 4,6-DMDBT [123]. An schematic view of the reaction network for the HDS of 4,6-DMDBT is presented in Figure 1.8.

Literature on HDS is quite voluminous; where a large number of studies have utilized transition metal supported catalysts, among them mostly Co/Mo and Ni/Mo [119,121,122,125-132]. In contrast, the use of noble metals are less frequent and those literatures devoted to the HDS of 4,6-DMDBT with noble metal supported catalysts are limited mostly on Pt-Pd [2,123,124,133-138]. Transition metals are transformed into

sulfide species in the presence of sulfur and this reduces their activity. On the other hand, noble metals have a better sulfur resistance, which can be modified by alloying or using of an acidic support material such as zeolites [123,124]. However, exposure to a large concentration of sulfur can ultimately poison and reduce the catalytic activity of every catalyst. Therefore, and due the cost and availability concerns tied to noble metals, they are usually suggested for usage in the very last stages of a hydrotreating process, where the concentration of sulfurous species have been already reduced to values below 500 ppm [2]. This allows saving the excellent catalytic behaviour of noble metals for the ultra-deep HDS of the most refractory sulfur-containing molecules.
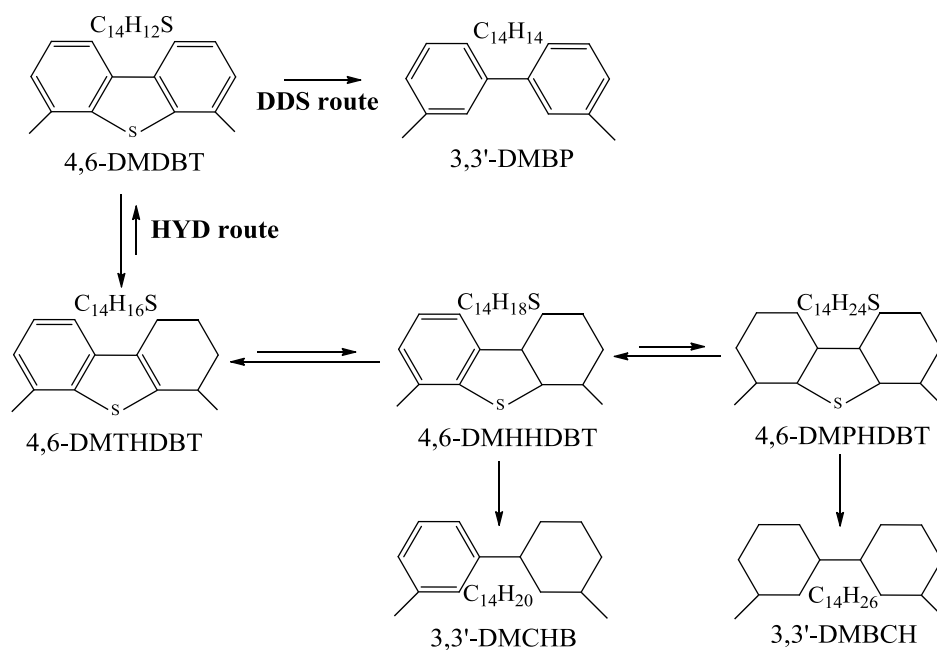
Figure 1.8. The DDS and HYD reaction pathways in the HDS of 4,6-DMDBT at 300°C and 5 MPa. Reprinted from [124] with permission from Elsevier.

1.6. Objectives and outline of the thesis

The objective of this thesis is to understand the role of each metal in selected Ir-based bimetallic catalysts in industrially important ring opening and hydrodesulfurization

reactions. The novelty of the work is the use of structure-controlled synthesis of bimetallic nanoparticles. As opposed to the traditional impregnation technique for catalyst preparation, the approach allows controlling the active-site architecture and correlating the surface composition with catalytic activity and selectivity. The fundamental thesis hypothesis is that it is possible to differentiate between the intrinsic and observed synergism (when the observed changes happen only to a different metal dispersion) in bimetallic catalysis using the structure-controlled nanoparticles. The practical goal is to develop active and selective Pt-free catalysts for ring opening and ultra-deep hydrodesulfurization.

Three quarter of the thesis concerns the RO of indane as the model reaction, which as mentioned earlier relies strongly on the hydrogenolysis activity of the catalysts. Our approach was to find an active Pt-free formulation (due to cost and S-susceptibility concerns); therefore, iridium was the first metal of choice due to its superb hydrogenolysis activity as mentioned in section 1.4. Pd was also selected as the second metal since it has an outstanding hydrogenation activity, which could effectively serve for HDS. γ-Al$_2$O$_3$, with weakly acidic properties, was used as the support material in line with the specifications mentioned in section 1.4. After the role of each metal in SRO of indane was realized in chapter 2 (specifically, only dispersing action of Pd on Ir functioning), we also tested Ni instead of Pd, which is cheaper and can be a good candidate for filling the core (inside) positions, providing a high dispersion for surface Ir atoms.

The outline of the remaining chapters is summarized as follows:

Chapter 2 discusses the structure-controlled synthesis of Pd-Ir bimetallic nanoparticles and their catalysis for SRO of indane. It was shown that monodispersed bimetallic nanoparticles (1.6 nm − 2.7 nm) with random alloy and core-shell structures

could be successfully prepared by the colloid chemistry method. The as-prepared nanoparticles as well as the supported catalysts were studied using several characterization techniques to confirm the nanoparticle bimetallicity and surface structure; the bimetallic functioning was analyzed to explain the exact role of each metal in catalytic reaction. It was realized that the presence of contiguous surface Ir atoms is necessary for maintaining a high catalytic activity through the dicarbene mechanism. With the use of the activity calculations based on surface atoms (also known as turnover frequency numbers), the role of Pd was explained as being the inert surface diluting agent in alloy samples as well as the dispersing agent for core-shell catalyst providing a complete Ir dispersion (geometrical effects). Within this type of functioning, the best catalyst activity and the highest yield of SRO products were observed with the Pd(core)Ir(shell) sample, where all the surface was covered with Ir and it was highly active for atmospheric ring opening. Therefore, any changes in the intrinsic activity of the metals interacting were ruled out and the activity differences were ascribed to the observed synergism only.

The Pd-Ir bimetallic catalysts discussed in chapter 2 were studied in chapter 3 in view of how the presence and/or removal of the polymeric stabilizer used during the synthesis affected their catalysis in atmospheric ring opening of indane. Physicochemical properties of the supported catalysts were examined by appropriate characterization techniques like TEM, CO chemisorption and CO-DRIFTS and the catalytic activity of the catalysts was studied after different thermal treatments corresponding to the complete or partial removal of the stabilizing polymer from the catalyst's surface. It was shown that a thorough polymer removal is necessary for samples with Pd-rich surface to present a high catalytic performance; however, those samples with Ir-rich surface were less affected by

the presence of PVP remnants. Therefore, it is realized that the necessity for removal of the residual polymeric stabilizer before catalysis depends on nature of metals as well as their surface (and not bulk) structure in bimetallic catalysts.

After realizing the dilution and/or dispersing roles of Pd in bimetallic Pd-Ir catalysts in chapter 2 and finding the appropriate thermal treatment to clean the surface of catalysts in chapter 3, chapter 4 deals with the structure-controlled synthesis of another series of bimetallic nanoparticles, i.e. Ni-Ir, and their catalysis in the atmospheric SRO of indane. This chapter aims at utilizing a cheaper metal than Pd (like Ni) to successfully provide the same role and be used as a more economical catalyst. Our results in this chapter indicated that Ni could similarly save the expensive Ir atoms on the outer shell without negatively affecting its outstanding performance for SRO reaction. In fact, using two bimetallic catalysts with 1:1 molar ratio of Ni:Ir, the significant increase of the catalytic activity was observed for the sample with Ni(core)Ir(shell) structure. In addition, characterization techniques confirmed that Ir enhanced the thermal stability of Ni atoms toward sintering.

It is worth mentioning that the our group previous results investigated and showed the differential reactor behaviour to remain valid for the ring opening of indane in the conversion range of 5-70% [109]. This finding was considered when discussing the activity values in chapter 2-4 of the current thesis.

In chapter 5, a series of Pd-Ir bimetallic nanoparticles with core-shell and alloy structures were studied in the HDS of 4,6-DMDBT as well as the high-pressure hydrogenation of indane. Ir was shown to be more active than Pd in the HDS of 4,6-DMDBT due to the severe sintering of monometallic Pd nanoparticles during the catalyst

pretreatment, while the activity per surface atoms was significantly higher for Pd. Activity calculations per surface species helped to realize the bimetallic functioning and explain the main role of Ir as being the diluting agent for Pd atoms to prevent the severe sintering that Pd suffers from. The addition of Ir to Pd was found to increase the HDS activity of the bimetallic catalysts in both paths of DDS and HYD mainly due to the high tendency of Ir for hydrogenolysis and the smaller size of Ir-enriched samples. In addition, hydrogenation of indane at high pressure was studied at the end of this chapter, where the activity of Pd is similarly increased when combined with Ir. However, in a mixture containing both indane and 4,6-DMDBT, it is the latter that wins the competition for hydroconversion and no or insignificant hydrogenation of indane is observed in the presence of 300 ppm sulfur as 4,6-DMDBT. Thus, the Pd-Ir catalysts can be used to remove the highly-refractory sulfur without significantly affecting the cetane/octane number of the fuel. The HDS catalyst stability was evaluated for 3 days on stream with S removal down to < 15 ppm. Is it mentioned here that chapter 5 shows a preliminary results of the catalysts studied in the HDS of 4,6-DMDBT. More in depth characterizations will be tested by other group members to investigate parameters such as sintering and/or size changes of the catalysts after the catalytic reaction.

And finally, chapter 6 provides some concluding remarks about the materials covered in the thesis as well as some suggestions for possible future works.

1.7. References

[1] M. Booth, J.G. Buglass, J.F. Unsworth, Top. Catal. 16/17 (2001) 39–46.

[2] M. Lewandowski, P. Da Costa, D. Benichou, C. Sayag, Appl. Catal. B 93 (2010) 241–249.

[3] V. Calemma, R. Giardino, M. Ferrari, Fuel Process. Technol. 91 (2010) 770–776.

[4] U. Nylen, L. Sassu, S. Melis, S. Jaras, M. Boutonnet, Appl. Catal. A 299 (2006) 1–13.

[5] M. W. Roberts, Catal. Lett. 67 (2000) 1–70.

[6] B. Coq, F. Figueras, J. Mol. Catal. A: Chem. 173 (2001) 117–134.

[7] W. Yu, M. D. Porosoff, J. G. Chen, Chem. Rev. 112 (2012) 5780−5817.

[8] J. H. Sinfelt, Bimetallic Catalysts: Discoveries, Concepts and Applications, John Wiely & Sons, Inc., New York, (1983).

[9] C. H. Bartholomew, R. J. Farrauto, Fundamentals of industrial catalytic processes, Wiley Interscience, Hoboken, New Jersey, (2006).

[10] G.C. Bond, A.F. Rawle, J. Mol. Catal. A: Chem. 109 (1996) 261−271.

[11] L. Guczi, Z. Schay, Gy. Stefler, L.F. Liotta, G. Deganello, A.M. Venezia, J. Catal. 182 (1999) 456−462.

[12] J.L. Carter, G.B. McVicker, W. Weissman, W.S. Kmak, J.H. Sinfelt, Appl. Catal. 3 (1982) 327−346.

[13] A. J. van Dillen, R. J.A.M. Terorde, D. J. Lensveld, J. W. Geus, K. P. de Jong, J. Catal. 216 (2003) 257–264.

[14] F. Schuth, M. Hesse, K. K. Unger, in: G. Ertl, H. Knozinger, F. Schuth and J. Weitkamp (Eds.), Handbook of Heterogeneous Catalysis, Wiley-VCH, Weinheim, (2008) 100–119.

[15] E. F. Gallei, M. Hesse and E. Schwab, in: G. Ertl, H. Knozinger, F. Schuth and J. Weitkamp (Eds.), Handbook of Heterogeneous Catalysis, Wiley-VCH, Weinheim, (2008) 57–66.

[16] P. Sonstrom, M. Baumer, Phys. Chem. Chem. Phys. 13 (2011) 19270–19284.

[17] G. Schmid, N. Toshima, B. Corain (Eds.), Metal Nanoclusters in Catalysis and Material Science: The Issue of Size Control, Elsevier Science, Amesterdam (2008).

[18] N. Semagina, L. Kiwi-Minsker, Catal. Rev. 51 (2009) 147–217.

[19] N. Toshima, T. Yonezawa, K. Kushihash, J. Chem. Soc., Faraday Trans. 89 (1993) 2537–2543.

[20] B. Zhao, N. Toshima, Chem. Express 5 (1990) 721–724.

[21] G. Schmid, H. West, J.O. Halm, J.O. Bovin, C. Grenthe, Chem. Eur. J. 2 (1996) 1099–1103.

[22] H. Bonnemann, K. S. Nagabhushana, in: G. Schmid, N. Toshima, B. Corain (Eds.). Metal Nanoclusters in Catalysis and Material Science: The Issue of Size Control, Elsevier Science, Amesterdam, (2008) 21–48.

[23] J. Turkevich, P. C. Stevenson, J. Hillier, Discuss. Faraday Soc. 11 (1951) 55–75.

[24] N. Toshima, H. Yan, Y. Shiraishi, in: G. Schmid, N. Toshima, B. Corain (Eds.). Metal Nanoclusters in Catalysis and Material Science: The Issue of Size Control, Elsevier Science, Amesterdam, (2008) 49–75.

[25] H. Hirai, Y. Nakao, N. Toshima, K. Adachi, Chem. Lett. 5 (1976) 905–910.

[26] Y. Wang, N. Toshima, J. Phys. Chem. B 101 (1997) 5301–5306.

[27] D. G. Duff, P. P. Edwards, B. F. G. Johnson, J. Phys. Chem. 99 (1995) 15934–15944.

[28] C.-R. Bian, S. Suzuki, K, Asakura, L. Ping, N. Toshima, J. Phys. Chem. B 106 (2002) 8587–8598.

[29] N. Toshima, M. Kanemaru, Y. Shiraishi, Y. Koga, J. Phys. Chem. B 109 (2005) 16326–16331.

[30] Y. Chen, K. Y. Liew, J. Li, Mater. Lett. 62 (2008) 1018–1021.

[31] X. Yan, H. Liu, K.Y. Liew, J. Mater. Chem. 11 (2001) 3387–3391.

[32] T. Teranishi, M. Miyake, Chem. Mater. 10 (1998) 594–600.

[33] F. Bonet, V. Delmas, S. Grugeon, R. Herrera Urbina, P-Y. Silvert, K. Tekaia-Elhsissen, Nanostruct. Mater. 11 (1999) 1277–1284.

[34] A. Henglein, C. Brancewicz, Chem. Mater. 9 (1997) 2164–2167.

[35] M. Liu, W. Yu, H. Liu, J. Zheng, J. Colloid Interface Sci. 214 (1999) 231–237.

[36] J. Yang, J. Y. Lee, L. X. Chen, H. P. Too, J. Phys. Chem. B 109 (2005) 5468–5472.

[37] H. M. Chen, R. S. Liu, L. Y. Jang, J. F. Lee, S. F. Hu, Chem. Phys. Lett. 421 (2006) 118–123.

[38] Y. Chen, F. Yang, Y. Dai, W. Wang, S. Chen, J. Phys. Chem. C 112 (2008) 1645–1649.

[39] J. M. Khurana, K. Vij, Catal. Lett. 138 (2010) 104–110.

[40] N. Toshima, M. Harada, T. Yonezawa, K. Kushihashi, K. Asakura, J. Phys. Chem. 95 (1991) 7448–7453.

[41] D. Astruc, F. Lu, J.R. Aranzaes, Angew. Chem. Int. Ed. 44 (2005) 7872–7872.

[42] R. M. Rioux, H. Song, J. D. Hoefelmeyer, P. Yang, G. A. Somorjai, J. Phys. Chem. B 109 (2005) 2192–2202.

[43] G. G. Couto, J. J. Klein, W. H. Schreiner, D. H. Mosca, A. J.A. de Oliveira, A. J.G. Zarbin, J. Colloid Interface Sci. 311 (2007) 461–468.

[44] F. Papa, C. Negrila, G. Dobrescu, A. Miyazaki, Ioan Balint, J. Nat. Gas Chem. 20 (2011) 537–542.

[45] P. Lu, T. Teranishi, K. Asakura, M. Miyake, N. Toshima, J. Phys. Chem. B 103 (1999) 9673–9682.

[46] S. Bhlapibul, K. Pruksathorn, P. Piumsomboon, Renewable Energy 41 (2012) 262–266.

[47] J. Shen, X. Yin, D. Karpuzov, N. Semagina, Catal. Sci. Technol. 3 (2013) 208–221.

[48] S.K. Singh, Q. Xu, Chem. Commun. 46 (2010) 6545–6547.

[49] N. Toshima, K. Hirakawa, Appl. Surf. Sci. 121 (1997) 534–537.

[50] L. Guczi, A. Beck, A. Horvath, Z. Koppany, G. Stefler, K. Frey, I. Sajo, O. Geszti, D. Bazin, J. Lynch, J. Mol. Catal. A: Chem. 204 (2003) 545–552.

[51] A.Q. Wang, C.M. Chang, C.Y. Mou, J. Phys. Chem. B 109 (2005) 18860–18867.

[52] P. Lu, N. Toshima, Bull. Chem. Soc. Jpn. 73 (2000) 751–758.

[53] N. Toshima, Y. Wang, Langmuir 10 (1994) 4574–4580.

[54] N. Toshima, Y. Shiraishi, T. Teranishi, M. Miyake, T. Tominaga, H. Watanabe, W. Brijoux, H. Bonnemann, G. Schmid, Appl. Organomet. Chem. 15 (2001) 178–196.

[55] L.M. Bronstein, D.M. Chernyshov, I.O. Volkov, M.G. Ezernitskaya, P.M. Valetsky, V.G. Matveeva, E.M. Sulman, J. Catal. 196 (2000) 302–314.

[56] T. Endo, T. Yoshimura, K. Esumi, J. Colloid Interface Sci. 286 (2005) 602–609.

[57] T. Endo, T. Kuno, T. Yoshimura, K. Esumi, J. Nanosci. Nanotechol. 5 (2005) 1875–1882.

[58] S.K. Ghosh, M. Mandal, S. Kundu, S. Nath, T. Pal, Appl. Catal. A 268 (2004) 61–66.

[59] X. Wang, W.B. Yue, M.S. He, M.H. Liu, J. Zhang, Z.F. Liu, Chem. Mater. 16 (2004) 799–805.

[60] Y. Lou, M.M. Maye, L. Han, J. Luo, C.-J. Zhong, Chem. Commun. 5 (2001) 473–474.

[61] T.C. Deivaraja, J.Y. Lee, J. Electrochem. Soc. 151 (2004) A1832–A1835.

[62] J. Lapujoulade, K. S. Neil, Surf. Sci. 35 (1973) 288–301.

[63] S. Bhlapibul, K. Pruksathorn, P. Piumsomboon, Renewable Energy, 41 (2012) 262–266.

[64] Y. Zhao, X. Yang, J. Tian, F. Wang, L. Zhan, Int. J. Hydrogen Energy 35 (2010) 3249–3257.

[65] S.J. Cho, S.K. Kang, Catal. Today 93 (2004) 561–566.

[66] A.U. Nilekar, S. Alayoglu, B. Eichhorn, M. Mavrikakis, J. Am. Chem. Soc. 132 (2010) 7418–7428.

[67] K. Nagaveni, A. Gayen, G. N. Subbanna, M. S. Hegde, J. Mater. Chem. 12 (2002) 3147–3151.

[68] Y. Mizukoshi, T. Fujimoto, Y. Nagata, R. Oshima, Y. Maeda, J. Phys. Chem. B 104 (2000) 6028–6032.

[69] N. Toshima, Y. Shiraishi, A. Shiotsuki, D. Ikenaga, Y. Wang, Eur. Phys. J. D, 16 (2001) 209–212.

[70] J. He, I. Ichinose, T. Kunitake, A. Nakao, Y. Shiraishi, N. Toshima, J. Am. Chem. Soc. 125 (2003) 11034–11040.

[71] S.J. Cho, R. Ryoo, Catal. Lett. 97 (2004) 71–75.

[72] J. N. Kuhn, C.-K. Tsung, W. Huang and G. A. Somorjai, J. Catal. 265 (2009) 209–215.

[73] C. A. Korgel, B. A. Stowell, Nano Lett. 5 (2005) 1203–1207.

[74] X. Fu, Y. Wang, N. Wu, L. Gui and Y. Tang, J. Colloid Interface Sci. 243 (2001) 326–330.

[75] R.M. Rioux, H. Song, M. Grass, S. Habas, K. Niesz, J.D. Hoefelmeyer, P. Yang, G.A. Somorjai, Top. Catal. 39 (2006) 167–174.

[76] A. Singh and B. D. Chandler, Langmuir 21 (2005) 10776–10782.

[77] Z.L. Wang, J.M. Petroski, T.C. Green, M.A. El-Sayed, J. Phys. Chem. B 102 (1998) 6145–6151.

[78] D. W. Vinokur, E. I. Werst, J. Phys. Chem. B 105 (2001) 1587–1593.

[79] J. Monzo, M.T.M. Koper, P. Rodriguez, ChemPhysChem 13 (2012) 709–715.

[80] S.O. Blavo, E. Qayyum, L.M. Baldyga, V.A. Castillo, M.D. Sanchez, K. Warrington, M.A. Barakat, J.N. Kuhn, Top. Catal. 56 (2013) 1835–1842.

[81] C. Aliaga, J.Y. Park, Y. Yamada, H.S. Lee, C.K. Tsung, P. Yang, G.A. Somorjai, J. Phys. Chem. C 113 (2009) 6150–6155.

[82] W. Chen, J. Kim, S. Sun and S. Chen, Phys. Chem. Chem. Phys. 8 (2006) 2779–2786.

[83] L. Cademartiri, A. Ghadimi, G. A. Ozin, Acc. Chem. Res. 41 (2008) 1820–1830.

[84] H. Wang, H. Tang, J. He, Q. Wang, Mater. Res. Bull. 44 (2009) 1676–1680.

[85] D. S. Deutsch, G. Lafaye, D. Liu, B. Chandler, C. T. Williams and M. D. Amiridis, Catal. Lett. 97 (2004) 139–143.

[86] C. Peniche, D. Zaldivar, M. Pazos, S. Paz, A. Bulay, J. San Roman, J. Appl. Polym. Sci. 50 (1993) 485–493.

[87] T. O. Hutchinson, Y. P. Liu, C. Kiely, C. J. Kiely, M. Brust, Adv. Mater. 13 (2001) 1800–1803.

[88] X. Wang, P. Sonstro m, D. Arndt, J. Stover, V. Zielasek, H. Borchert, K. Thiel, K. Al-Shamery and M. Baumer, J. Catal. 278 (2011) 143–152.

[89] P. Sonstrom, D. Arndt, X. Wang, V. Zielasek, M. Baumer, Angew. Chem., Int. Ed. 50 (2011) 3888–3891.

[90] P. Sonstrom, B. Jurgens, S. Tambou Djakpou, B. Ritz, K. Ahrenstorf, G. Grathwohl, H. Weller and M. Baumer, Catal. Sci. Technol. 1 (2011) 830–838.

[91] G. B. McVicker, M. Daage, M. S. Touvelle, C. W. Hudson, D. P. Klein, W. C. Baird Jr., B. R. Cook, J. G. Chen, S. Hantzer, D. E. W. Vaughan, E. S. Ellis, O. C. Feeley, J. Catal. 210 (2002) 137–148.

[92] R.C. Santana, P.T. Do, M. Santikunaporn, W.E. Alvarez, J.D. Taylor, E.L. Sughrue, D.E. Resasco, Fuel 85 (2006) 643–656.

[93] H. Du, C. Fairbridge, H. Yang, Z. Ring, Appl. Catal. A 294 (2005) 1–21.

[94] W.E. Alvarez, D.E. Resasco, J. Catal. 164 (1996) 467–476.

[95] D. Teschner, K. Matusek, Z. Paal, J. Catal. 192 (2000) 335–343.

[96] F. Luck, J.L. Schmitt, G. Maire, React. Kinet. Catal. Lett. 21 (1982) 219–224.

[97] C.G. Walter, B. Coq, F. Figueras, M. Boulet, Appl. Catal. A 133 (1995) 95–102.

[98] S. Dokjampa, T. Rirksomboon, D.T.M. Phuong, D.E. Resasco, J. Mol. Catal. A: Chem. 274 (2007) 231–240.

[99] S. Lecarpentier, J.V. Gestel, K. Thomas, J.-P. Gilson, M. Houalla, J. Catal. 254 (2008) 49–63.

[100] R. Moraes, K. Thomas, S. Thomas, S.V. Donk, G. Grasso, J.-P. Gilson, M. Houalla, J. Catal. 286 (2012) 62–77.

[101] D. Kubicka, N. Kumar, P. Maki-Arvela, M. Tiitta, V. Niemi, H. Karhu, T. Salmi, D.Yu. Murzin, J. Catal. 227 (2004) 313–327.

[102] D. Kubicka, T. Salmi, M. Tiitta, D.Yu. Murzin, Fuel 88 (2009) 366–373.

[103] J.-W. Park, K. Thomas, J.V. Gestel, J.-P. Gilson, C. Collet, J.-P. Dath, M. Houalla., Appl. Catal. A 388 (2010) 37–44.

[104] P.T. Do, W.E. Alvarez, D.E. Resasco, J. Catal. 238 (2006) 477–488.

[105] J.G. Van Senden, E.H. Van Broekhoven, C.T.J. Wreesman, V. Ponec, J. Catal. 87 (1984) 468–477.

[106] A. Djeddi, I. Fechete, F. Garin, Appl. Catal. A 413 (2010) 340–349.

[107] F. Garin, P. Girard, F. Weisang, G. Maire, J. Catal. 70 (1981) 215–220.

[108] U. Nylen, J.F. Delgado, S. Jaras, M. Boutonnet, Appl. Catal. A 262 (2004) 189–200.

[109] J. Shen, Bimetallic catalysts for low pressure ring opening [M.Sc. thesis], University of Alberta, Edmonton, Canada (2011).

[110] S. K. Bej, S. K. Maity, U. T. Turaga, Energy Fuels 18 (2004) 1227–1237.

[111] R. Shafi, G. J. Hutchings, Catal. Today 59 (2000) 423–442.

[112] T. Kabe, A. Ishihara, Q. Zhang, Appl. Catal. A 97 (1993) L1–L9.

[113] B. C. Gates, M. J. Girgis, Ind. Eng. Chem. Res. 30 (1991) 2021–2058.

[114] M. Houalla, D.H. Broderick, A.V. Sapre, N.K. Nag, V.H.J. de Beer, B.C. Gates, H. Kwart, J. Catal. 61 (1980) 523–527.

[115] M. J. Girgis, B. C. Gates, Ind. Eng. Chem. Res. 30 (1991) 2021–2058.

[116] P. T. Vasudevan, J. L. G. Fierro, Catal. Rev.-Sci. Eng. 38 (1996) 161–188.

[117] B. C. Gates, Henrik Topsoe, Polyhedron 16 (1997) 3213–3217.

[118] D.D. Whitehurst, T. Isoda, I. Mochida, Adv. Catal. 42 (1998) 345–471.

[119] F. Bataille, J.-L. Lemberton, P. Michaud, G. Perot, M. Vrinat, M. Lemaire, E. Schulz, M. Breysse, S. Kasztelan, J. Catal. 191 (2000) 409–422.

[120] S. K. Bej, S. K. Maity, U. T. Turaga, Energy Fuels 18 (2004) 1227–1237.

[121] T. Kabe, A. Ishihara, Q. Zhang, Appl. Catal. A 97 (1993) L1–L9.

[122] V. Lamure-meille, E. Schulz, M. Lemaire, M. Vrinat, Appl. Catal. A 131 (1995) 143–157.

[123] Y. Sun, H. Wang, R. Prins, Catal. Today 150 (2010) 213–217.

[124] A. Niquille-Röthlisberger, R. Prins, J. Catal. 242 (2006) 207–216.

[125] V. Meille, E. Schulz, M. Lemaire, M. Vrinat, J. Catal. 170 (1997) 29–36.

[126] D.R. Kilanowski, H. Teeuwen, B.C. Gates, V.H.J.D. Beer, G.C.A. Schuit, H. Kwart, J. Catal. 55 (1978) 129–137.

[127] Q. Zhang, W. Qian, A. Ishihara, T. Kabe, J. Jpn. Petrol. Inst. 40 (1997) 185–191.

[128] T. Kabe, K. Akamatsu, A. Ishihara, S. Otsuki, M. Godo, Q. Zhang, W. Qian, Ind. Eng. Chem. Res. 36 (1997) 5146–5152.

[129] A. B. Bjerre, E. Sorensen, Ind. Eng. Chem. Res. 31 (1992) 1577–1580.

[130] X.L. Ma, K. Sakanishi, I. Mochida, Ind. Eng. Chem. Res. 35 (1996) 2487–2494.

[131] M. Egorova, R. Prins, J. Catal. 225 (2004) 417–427.

[132] H. Wang, R. Prins, J. Catal. 264 (2009) 31–43.

[133] A. Röthlisberger, R. Prins, J. Catal. 235 (2005) 229–240.

[134] A. Ishihara, F. Dumeignil, J. Lee, K. Mitsuhashi, E. W. Qian, T. Kabe, Appl. Catal. A 289 (2005) 163–173.

[135] A. Niquille-Rothlisberger, R. Prins, Catal. Today 123 (2007) 198–207.

[136] H. Guo, Y. Sun, R. Prins, Catal. Today 130 (2008) 249–253.

[137] Y. Sun, R. Prins, Angew. Chem. Int. Ed. 47 (2008) 8478–8481.

[138] T. Klimova, P. M. Vara, I. P. Lee, Catal. Today 150 (2010) 171–178.

Chapter 2: Size- and structure-controlled mono- and bimetallic Ir-Pd nanoparticles in selective ring opening of indane[1,2]

2.1. Introduction

Bimetallic catalysts play a significant role in the chemical industry as the addition of a second metal may promote the performance of monometallic materials. The alloying of Pd with Au, Ag, Cu, or Pb for the selective hydrogenations or the promotion of Pt-based catalysts with Ir and Re in the reforming units are just a few of the most prominent examples in this area [1-4]. Bimetallicity can change the activity, selectivity, and stability of monometals *via* electronic and geometric effects and the occurrence of mixed sites [5]. Electronic effects can be explained as the redistribution of charge in a metal, or charge transfer between two metals in a bimetallic composition, that can modify the catalytic properties through the mode and adsorption strength of the reaction participants. Geometric effects mostly concern the positioning of surface atoms in bimetallic catalysts and sometimes can result in the dilution of surface active sites with those of an inactive metal. Finally, a mixed-site may be interpreted as an active site where both metals participate in the catalytic action [5].

---

[1] A version of the materials in this chapter has been published in: H. Ziaei-Azad, C.-X. Yin, J. Shen, Y. Hu, D. Karpuzov and N. Semagina, *Journal of Catalysis* 300 (2013) 113–124; as well as H. Ziaei-Azad, C.-X. Yin, J. Shen, Y. Hu, D. Karpuzov and N. Semagina, *Journal of Catalysis* 304 (2013) 149 (as a Corrigendum). Both reprinted with permission from Elsevier.

[2] Large part of this chapter includes experimental results previously reported by our group member Jing Shen in her M.Sc. thesis "Bimetallic catalysts for low-pressure ring opening", University of Alberta (2011); used with permission by Jing Shen. Jing performed synthesis, UV-vis and TEM analysis of nanoparticles, and their catalytic testing. However, no characterizations on nanoparticle bimetallicity and surface composition were performed, thus, no analysis was made. This chapter was a first goal of my work, i.e., to evaluate the possibility of linking the nanoparticle structure to its performance. I performed additional characterization, performed TOF analyses, wrote the chapter, analyzed data and proposed the major outcome that Pd serves only as a dispersing agent for Ir.

Traditionally, heterogeneous catalysts are prepared by the deposition of molecular precursors on supports followed by thermal treatments in various atmospheres. This technique usually results in a poor control over the particle size, structure, and the close vicinity between the two metals, giving rise to a wide family of monometallic and bimetallic particles with different compositions that coexist at the surface [5]. As the surface composition in most cases is not controlled and/or known, the changes in catalytic behaviour are typically assigned to synergism effects between the two metals, and the role of each metal in the bimetallic formulations is difficult to explain. On the contrary, if the surface bimetallic composition is well known, the metal functions can be quantitatively described and either confirm or reject intrinsic synergism hypothesis.

In recent years, much attention has been paid to the size and shape controlled synthesis of metallic nanoparticles for catalytic applications [6]. This interest mainly originates from the quantum size effects created in nanoparticles as a result of a significant reduction in the particle size (below 5 nm), which can alter the chemical activity and selectivity of the metallic nanoparticles [6]. Colloid chemistry techniques have been applied for the controlled synthesis of bimetallic nanoparticles, such as so-called "random alloy" and the "core/shell" structures. Steric stabilizers like polyvinylpyrrolidone (PVP) are usually used during the synthesis to protect nanoparticles from excessive growth [7]. Numerous examples of such bimetallic catalytic nanoparticles have been documented in literature, such as the application of alloy-like structures NiPd, CuPd, PtPd, PdM (M = Au, Pt, Zn) and PdRh for hydrogenation [8-15], NiIr and PtRu for hydrogen generation [16,17], AuPt and NiPt for electrooxidation [18,19], AgAu, AuPd and NiPt for reduction [20-22], AuPd and AgAu for CO oxidation [23,24], FeRu and FePt for the formation of single-

walled carbon nanotubes (SWNTs) [25], along with those of the core/shell structures Au/Pd, Pd/Pt and Ag/Pd for hydrogenation [26-29], M/Pt (M = Ru, Rh, Ir, Pd, or Au) for preferential CO oxidation in hydrogen [30], Pt/Sn for aromatisation [31], Au/M (M = Pd, Pt, Rh) for hydrogen generation [32,33], Pd/Pt for methane combustion [34] and Pd/Pt for electrooxidation [35].

In the plethora of catalytic processes, the refining industry is one of the most important areas in which bimetallic nanoparticles play a key role. One of the pioneering examples in this category dates back to the 1970s, when Exxon introduced the Pt-Ir bimetallic catalysts to the reforming units with improved activity and sulfur resistance compared to the monometallic Pt previously used [4,36]. On the other hand, internal combustion engines are still the main source of road transportation and the role of catalysis in increasing the yield of premium quality fuels produced in the refineries is vital. The catalytic selective ring opening (SRO) of polyaromatic and naphthenic compounds found in the heavy oil fractions is one of the key processes in increasing the quality of fuels, as during the process a C-C bond on the ring is cleaved only once, retaining the same number of the carbon atoms in the product [37,38]. In terms of the cetane number improvement, it is important that the cleavage occurs at the substituted C-C bonds [39]. Most of the literature studies on SRO have been focused on relatively small molecules like methylcyclopentane (MCP), which has a boiling point ($\sim$72°C) far from the diesel cut [40-43]. Another model compound, indane (benzocyclopentane, C_9H_{10}), with one aromatic and naphthenic ring also has been applied as a test substance for the SRO [37].

Since the 1970s, the ring opening of cyclic compounds has been studied extensively using Pt-group supported catalysts [37,41,42,44-54]. It is reported that the RO of

naphthenic rings relies on a metal-driven chemistry, and that the Ir has always stood out as the most active metal for these reactions, although its high cracking propensity may reduce the yield of the single cleavage products [44,45,48,50,55]. Not only the metal nature but also the size of the catalytic nanoparticles can alter the way they behave in RO reactions due to the reaction structure sensitivity. RO of MCP is well-known for its structure sensitivity: Pt nanoparticles larger than 2 nm lead to cleavage only on substituted carbons, while below that, cleavage on unsubstituted carbons is also possible. Such behaviour is related to the metal crystal surface statistics, as the presence of at least two contiguous edge atoms in bigger particles facilitate the formation of complexes that yield 2-methylpentane (2MP) and 3-methylpentane (3MP) [41,46]. Size effect can also change the activity of a specific metal for RO reactions. For example, the RO of MCP over Rh, which operates on the unsubstituted carbons, showed higher specific activity on higher loading Rh particles (10% Rh/Al_2O_3) than the lower loading samples (0.3% Rh/Al_2O_3), which was ascribed to the corrugate flat morphology (higher proportion of face atoms) in larger Rh particles [42]. Similarly, larger Ru (3 nm) turned out to be more active than the smaller ones (1.2 nm) in the SRO of methylcyclohexane, where the strength of H_2 chemisorption played the key role [47]. The blocking and/or poisoning of the active sites can also change the behaviour in RO reactions. For instance, the RO of MCP over Ir, which happens only on the unsubstituted carbons, is reported not to be size sensitive; however, the presence of the carbonaceous layer on the Ir particles can result in the production of n-hexane as well as 2MP and 3MP. This behaviour reportedly happens due to the elimination of a large number of contiguous sites (face atoms) attacked by the carbon layer, which could facilitate the production of 2MP and 3MP. The resistance to self-poisoning by carbon

deposits is reportedly higher in smaller particles, which contain more edges and corner atoms than face atoms [56].

Thus, to correlate the catalytic behaviour with nanoparticle metal nature of some definite size, nanoparticles' monodispersity is of crucial importance. The issue becomes even more important when it comes to the comparison of mono- and bimetallic nanoparticles, as the size effect should not influence a researcher's hypothesis on the role of the second metal in bimetallic formulations. The colloidal techniques of nanoparticle size and structure control become particularly advantageous in elucidating mechanisms over bimetallic catalysts.

The present study is devoted to the development of size- and structure-controlled mono- and bimetallic Ir-Pd nanoparticles with high catalytic activity and selectivity in SRO. A Pt-free catalyst was targeted due to the relatively high cost of Pt and its low sulfur tolerance. The work stands out of the numerous investigations on Ir-based SRO catalysts due to the enhanced control over the nanoparticle size and structure, which makes it possible to correlate the bimetallic nanoparticle composition with its catalytic properties. We believe that such approach should become routine in bimetallic catalysis to elucidate intrinsic or observed synergism between the two metals.

Iridium is selected due to its known high ring opening activity, and palladium due to its excellent hydrogenation activity as a probable candidate for platinum replacement. Obtaining different bimetallic structures allowed us to obtain insight into the bimetallic catalyst functioning; moreover, it is advantageous to be able to place the atoms of Ir, which is one of rarest elements on Earth, only at the outer shell of nanoparticles for an optimum catalyst formulation. We report both random alloys and Pd(core)-Ir(shell) nanoparticles as

efficient catalysts in indane ring opening (sulfur-free, as a model reaction). The comparison of the catalytic behaviour of the developed catalysts and that one of the industrial Pt-Ir counterpart allows suggesting them as prominent advanced materials for SRO.

2.2. Experimental

2.2.1. Materials

Hydrogen hexachloroiridate (IV) hydrate ($H_2IrCl_6 \cdot xH_2O$, Sigma-Aldrich), dihydrogen tetrachloropalladate (II) (H_2PdCl_4, 5% w/v solution, Acros Organics), polyvinylpyrrolidone (PVP, average molecular weight 40,000, Sigma-Aldrich), gamma alumina (γ-Al_2O_3, average pore size 58 Å, SAA 155 m^2/g, Sigma-Aldrich), ethanol (95 vol.%, Fischer Scientific), and acetone (>99.7%, Fischer Scientific) were used as received. Nitrogen, argon, and hydrogen of ultra-high purity (99.999%) were purchased from Praxair. Milli-Q water (18.2 MΩ·cm) was used throughout the work. Benzocyclopentane (indane, 95% vol., Sigma-Aldrich) was distilled once. A batch of Pt-Ir industrial catalyst was used to compare the catalytic behaviour; its composition and other properties are not reported due to the confidentiality issues.

2.2.2. Catalyst preparation

Pd and Ir mono- and bimetallic nanoparticles were preformed in a colloidal dispersion before deposition on γ-Al_2O_3. Alcohol reduction is known as a simple and effective way to produce well-dispersed nanoparticles [32]. Pd and Ir monometallic nanoparticles were synthesised by the one-step alcohol reduction method, which has been described elsewhere for Pd [57]. Briefly, 50 ml of the 2 mM solution of either H_2PdCl_4 or

H$_2$IrCl$_6$ in Milli-Q water together with 0.22 g of PVP (PVP/metal = 20:1 mol/mol) were added to a 250-ml three-neck flask and mixed with 120 ml of water and ethanol solution (3:2 v/v). The resulting mixture was stirred and heated until it came to boil, and then refluxed in air under vigorous stirring for 3 h to complete the synthesis of PVP-protected nanoparticles. A dark but transparent and homogeneous colloidal dispersion of nanoparticles was obtained at the end of synthesis without any precipitate.

Bimetallic nanoparticles were synthesised with two different methods of co-reduction and hydrogen-sacrificial reduction to produce random alloy and core-shell particles, respectively. For the co-reduction synthesis of Pd and Ir nanoparticles, 50 ml of the 2 mM solution of metal precursors with two different molar ratios of Pd:Ir = 1:1 and Pd:Ir = 1:3 were prepared and added to a 250-ml three-neck flask. As the final Pd:Ir molar ratios in the resulting catalysts were found as 2:1 and 1:1, respectively, the catalysts hereafter are referred as Pd2Ir1 and Pd1Ir1. A certain amount of PVP (PVP/metals = 10:1 mol/mol) was added as well, and the rest of the process was exactly the same as that of monometallic nanoparticles. The mixture of metal precursors was simultaneously reduced in a one-step process in the alcohol-water solution using the co-reduction technique. The resulting colloidal solution obtained was macroscopically homogeneous and transparent without any precipitate.

In addition to the Pd2Ir1 and Pd1Ir1 nanoparticles, another bimetallic structure Pd(core)-Ir(shell) with a Pd:Ir molar ratio of 1:1 (hereafter referred as Pd(c)Ir(s)) was synthesised using the hydrogen-sacrificial reduction method. Pd monometallic core nanoparticles were synthesised as *vide supra*. After the refluxing time, the solution was allowed to cool down to room temperature followed by purging with hydrogen for 1.5 h.

This procedure creates Pd hydride, which further serves to reduce Ir and form an Ir shell around the preformed Pd nanoparticle. To create an Ir shell, 50 ml of 2 mM $H_2IrCl_6 \cdot xH_2O$ solution in water was added via a dropping funnel; the precursor solution was constantly purged with N_2, while the Pd-Ir dispersion with H_2. The final dispersion was left under hydrogen overnight. No precipitation was observed at the end of synthesis and the resulting colloidal dispersion was macroscopically homogeneous and transparent.

All the synthesised nanoparticles were supported on predried γ-Al_2O_3. The nanoparticles were precipitated using acetone in the presence of alumina [58]. The resulting powder was dried in the fumehood overnight to form the so-called fresh catalysts, which were then calcined in air at 200°C for 1 h.

2.2.3. Catalyst characterization

The actual Pd loadings on γ-Al_2O_3 was determined by a Varian SpectrAA 220FS atomic absorption (AA) spectrometer after Pd dissolution in hot nitric acid. The loading of Ir-containing nanoparticles was determined by neutron activation analysis (NAA). Samples were irradiated for 110 s in the Cd shielded, epi-thermal site of the reactor core. They were counted for 30 min each on an Aptec CS11-A31C gamma detector, approximately 12 h after irradiation.

UV visible spectroscopy was performed on nanoparticles in the colloidal solution with a Varian Cary 50 Scan UV visible spectrometer, 1 cm quartz cell.

Thermogravimetric analysis (TGA) was done using a TA instrument Q500 TGA device. Ca. 10-20 mg of sample was used for TGA measurements. TGA analyses performed on a selected catalyst (Ir/γ-Al_2O_3) under different conditions, i.e. i) fresh, ii) calcined in air at 200°C for 1 h, and iii) calcined in air at 200°C for 1 h followed by the

reduction in hydrogen at 359°C for 1 h. Some predried γ-Al$_2$O$_3$ was also tested for comparison. During the analysis, the temperature was increased from ambient to 110°C under N$_2$ flow, held for 10 min, then N$_2$ was switched to air and the temperature was further increased to 600°C with a heating rate of 5°C/min. Samples studied by TGA were also analysed by an Elementar Vario Micro elemental analyser for CHN percentage.

TEM images were recorded using a JEOL JEM2100 TEM device operating at 200 kV. Samples for TEM analysis were prepared by placing a drop of the colloidal dispersion of nanoparticles onto a carbon-coated copper grid, followed by the evaporation of the solvent at room temperature. The average diameter and the standard deviation were calculated by counting over 200 particles using the ImageJ software.

Scanning transmission electron microscopy (STEM) coupled with energy dispersive X-ray (EDX) spectroscopy was performed using a Hitachi HD-2000 operating at 200 kV on selected fresh catalysts calcined in air at 200°C for 1 h.

Hydrogen temperature programmed reduction (H$_2$-TPR) was performed using an AutoChem 2950 HP device (Micromeritics) under atmospheric pressure. About 500 mg of the catalysts calcined in air at 200°C for 1 h was used for the analysis. Before the TPR spectra were collected, samples were initially reduced in 10 ml/min mixture of 10% H$_2$ in Ar up to 375°C for 1 h and then oxidized in 10 ml/min of 10% O$_2$ in He mixture up to 400°C for 2 h. The active gases were switched to He and Ar after the reduction and oxidation steps, respectively; the samples were allowed to cool down to ambient temperature. The TPR spectra were collected in 10 ml/min mixture of 10% H$_2$ in Ar from ambient temperature to 300°C with a heating rate of 5°C/min.

X-ray photoelectron spectroscopy (XPS) was performed using a Kratos Axis 165 X-ray photoelectron spectrometer with a Mono Al Kα source operating at 15 mA and 14 kV. The XPS analysis was done on the pelletized samples which were calcined in air at 200°C for 1 h followed by the reduction in hydrogen at 359°C for 1 h. Background subtraction (Shirley-type), smoothing, and peak fitting were performed using the CasaXPS software package. All the core-level spectra were corrected with C 1s at 284.6 eV.

Ion scattering spectra of selected samples were obtained using a Kratos Axis 165 X-ray photoelectron spectrometer equipped with an ion scattering spectrometer, operated using noble gas ion beams (He$^+$) at 1 keV and scattering angle of 135 degrees. ISS of metallic silver foil was used to reference the energy scale. Similar catalysts but with higher metal loading (about 1 wt.%) was used for the analysis since an ISS detector requires relatively high metal loading for powdered samples. Prior to the analysis, samples underwent the calcination and reduction pretreatment as described above for the XPS studies.

The Pd L$_3$-edge XANES of the various samples were recorded at the Soft X-ray Microanalysis Beamline (SXRMB) 06B1-1 of the Canadian Light Source (CLS; Saskatoon, Canada) using a Si (111) double crystal monochromator (energy range, 1.7-10 keV; resolution, 1×10^{-4} ΔE/E). The same calcination and reduction pretreatment as for the XPS analyses was done on the samples prior to this analysis. Samples in powder form were mounted on the double-sided conducting carbon tape. Measurements were performed in total electron yield (TEY) mode by recording the drain sample current, and in fluorescence yield (FY) using a Si(Li) drift detector, all at room temperature. Both TEY and FY spectra were similar, but only TEY results will be presented here. Standard reference Pd foil was

also measured for the respective edge and used as the reference for comparison. The resulting XANES spectra were normalised using the Athena software.

2.2.4. Catalytic behaviour in indane ring opening

Catalytic studies on the indane (benzocyclopentane) ring opening were performed at 336°C (internal temperature) and atmospheric pressure in a flow stainless steel reactor (length of 16 in., i.d. ½ in.). Catalysts, calcined in air at 200°C for 1 h, were diluted with 2 g of #150 mesh SiC. 1.2 mg of the active metal(s) was used for each run (unless indicated otherwise). Gas flows were regulated with calibrated mass flow controllers (Sierra Instruments). The system was purged with Ar before and after each test. The catalysts were initially pre-treated with hydrogen *in situ*, 80 ml/min with temperature ramp from ambient to 359°C at 5°C/min, held for 1 h. At the end of pretreatment, the reactor temperature and the hydrogen flow rate were lowered to 350°C and 50 ml/min, respectively. The catalytic reaction started by bubbling hydrogen through the bubbler with indane that was kept at the constant temperature water bath of 10°C. An indane flow rate of 2.8 $\times$ 10^{-5} g/min was confirmed using GC, which was calibrated with a Gilson HPLC pump with a known indane flow rate. The reactor up- and down- streamlines were heated to 220°C to preheat the reactants and avoid product condensation. The reaction products were analysed online every 30 minutes with a 430 Varian Gas chromatograph equipped with an FID detector. The GC capillary column was a WCOT fused silica column, 50 m length $\times$ 0.32 mm inside diameter $\times$ 1.2 mm thickness. Initially, the oven temperature was stabilized at 40°C for 2.5 min; and then it started to increase at a rate of 30°C/min until the temperature reached 110°C and then it was maintained at 110°C for 20 min. FID and injector temperature were 280°C. The split ratio was 1. Helium flow rate was constant at 25 mL/min. Each catalyst

was tested for 240 min on stream. For the online product analysis, after a steady state was achieved (at 150 min time on stream), no more than 5% deviation in the mass balance was observed (typically, within 2%) as compared to the mass flow of incoming indane. The absence of external and internal mass transfer limitations was verified experimentally by varying the flow rate and estimating the Weisz-Prater criterion.

The reaction products, as well as indane impurities were identified via GC-MS that was performed with an Agilent Technologies 7890 GC coupled with a 5975C MSD. The GC column used is a ZB-50 (Phenomenex) column, 30 m length × 25 mm i.d. × 25-μm thickness. Oven temperature was stabilized at 40°C for 0.5 min, then increased to 110°C at 30°C/min, and then increased to 280°C at 50°C/min. The desired single cleavage products of ring opening are 2-ethyltoluene and *n*-propylbenzene. Main dealkylation products are *o*-xylene, ethylbenzene, toluene, and benzene. Compounds with GC retention times less than that of benzene were named as "lights", and products other than the major products and lights were called "others". The same main products were reported in the indane ring opening over Pt-Ir catalysts literature (see Scheme 2.1[1]) [37]. Raw GC results were corrected for indane impurities, and all calculations for indane conversion and product selectivities were based on the corrected GC results. Indane purified by distillation contains 0.09% benzene, 0.15% *n*-propylbenzene, 0.02% *2*-ethyltoluene, 0.02% lights, and 2.91% other.

---

[1] Scheme 2.1 is not part of the published materials indicated in the beginning of the chapter 2. It is added for clarification purpose only.
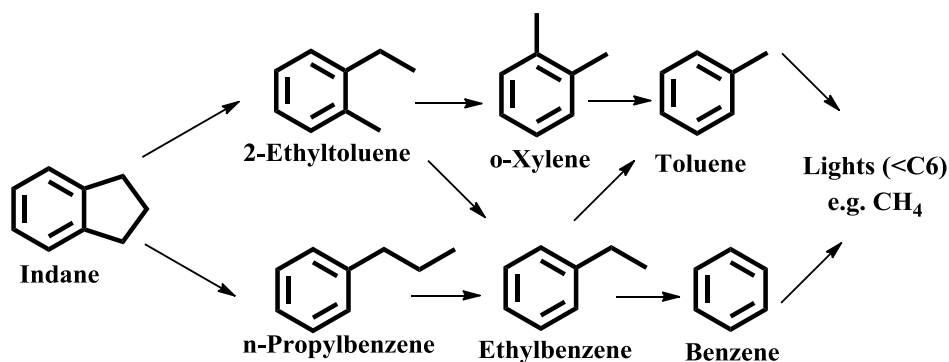
Scheme 2.1. Reaction pathway for the ring opening of indane at atmospheric pressure. Reprinted from [37] with permission from Elsevier[1].

Selectivities are reported on a mass basis as molar selectivity can give a distorted picture of indane utilisation because up to 9 moles of methane may be produced per mole of indane. The FID detector is a mass-sensitive analyser that responds to the number of carbon atoms entering per unit of time; thus, for each RO opening product, the selectivity was determined as the GC area of each product dividing by the difference between total GC area and the GC area of indane. Single cleavage selectivity is defined as the sum of the 2-ethyltoluene and *n*-propylbenzene formed divided by the amount of indane that has reacted. Selective RO yield is defined as the sum of 2-ethyltoluene and n-propylbenzene formed per the total amount of indane fed. For each catalyst, 10 data points were obtained at 90, 120, 150, 180, and 210 minutes of time on stream with a duplicate experiment. The carbon balance error never exceeded 10% and was typically within 3%. Within the indicated times on stream the catalysts did not show significant deactivation as will be seen from the conversion and selectivity versus time-on-stream profiles *vide infra*.

2.3. Results and discussion

2.3.1. Catalyst characterization

The formation of nanoparticles in the colloidal dispersion was confirmed by UV visible spectroscopy (Fig. 2.1). The Pd precursor solution presents a peak at about 206 nm, which has been reported as the characteristic peak of $PdCl_2$ [59]. During the synthesis of Pd nanoparticles, this peak disappeared and the colour of the medium changed from yellow (before the reflux) to dark brown (after the reaction). In the case of iridium, the starting solution shows two distinct peaks at 433 nm and 488 nm, which are in agreement with the literature data and can be ascribed to the ligand-to-metal charge-transfer (MLCT) absorption of $[IrCl_6]^{2-}$ ions [16]. Similarly, during the synthesis of Ir nanoparticles, the above-mentioned peaks disappeared, the absorption in the visible region increased, and the solution turned from pale yellow to dark brown after the reflux. This can be ascribed to the nanoparticles' formation as metal nanoparticles have the ability of absorbing photons in the UV visible region due to the coherent oscillation of their conduction band electrons [60]. As an example of bimetallic nanoparticles, the spectrum of the Pd(c)Ir(s) colloidal dispersion also confirms the nanoparticle formation, both for Pd and Ir counterparts[1].

---

[1] The nanoparticles used for UV-vis analysis were synthesized by Mrs. Jing Shen and the analysis was also performed by her. The UV-vis results have been taken from Jing Shen MSc. Thesis: "Bimetallic catalysts for low-pressure ring opening" submitted to University of Alberta (2011).
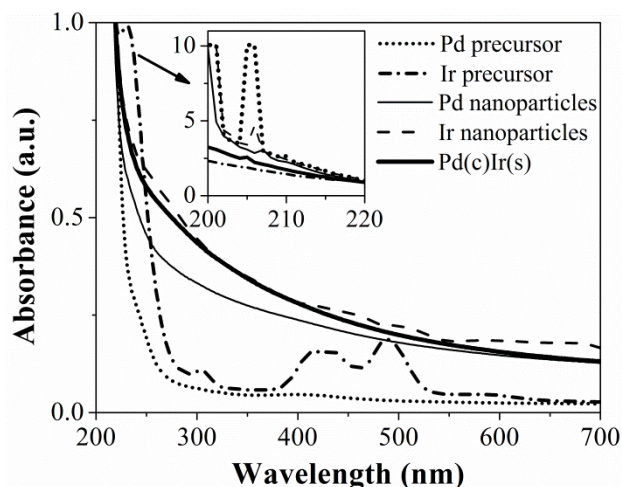
Fig. 2.1. UV–vis spectra of the selected PVP-stabilized nanoparticles and the starting solutions of metal precursors.

One of the important issues about the use of PVP-stabilized nanoparticles in a catalytic reaction is the removal of the protective polymer before assessing the catalyst performance. It is reported that part of the main chain of PVP can be adsorbed on the metal surface as a result of hydrophobic interactions [57]. According to Somorjai et al., an oxidation-reduction cycle is known to remove PVP from metal nanoparticles at lower temperature than free PVP decomposition. Maximum activity for ethylene hydrogenation with PVP-containing catalysts was shown after an oxidation-reduction pretreatment at 200°C [61]. Fig. 2.2 presents the results of thermogravimetric studies on the Ir/γ-Al$_2$O$_3$ catalyst sampled under different conditions, i.e. i) fresh, ii) calcined in air at 200°C for 1 h, and iii) calcined in air at 200°C for 1 h followed by the reduction in hydrogen at 359°C for 1 h. The third sample is the one which was further used for the catalytic reaction. The observed weight losses can be divided into three different regions: initially, below 200°C, the mass loss is mostly connected to the desorption of water physically adsorbed to the surface in the wet chemistry of synthesis. Between 200°C and 400°C, designated as the "slope change region", the largest mass loss occurs due to the thermal decomposition of

48

PVP which has been reported to occur between 200°C and 375°C under air in the presence of Pt nanoparticles [61]. Catalyst calcination at 200°C before the TGA reduces the mass loss only by 0.3 wt.%; when the calcined catalyst is further pretreated in hydrogen, the mass loss during the TGA increases to about 2.1 wt.%. Since the amount of PVP used for the synthesis of Ir/γ-Al$_2$O$_3$ nanoparticles was about 3.5 wt.%, the oxidation-reduction pretreatment performed in this study had a great impact on reducing the PVP residues from the samples. It should be mentioned that the weight increase due to the oxidation during the calcination at 200°C is negligible (< 0.01 wt.%). Besides, as the metal loadings in catalysts are very low (~0.1-0.3 wt.%), the metal oxidation weight increase is negligible as compared to the total observed ~2-3 wt.% mass loss. The CHN analysis was also done to strengthen the TGA results. The C wt.% for γ-Al$_2$O$_3$, fresh, calcined and the calcined-reduced catalysts were found to be 0.04, 2.0, 1.9 and 1.1 wt.%, respectively, which again shows the role of oxidation-reduction pretreatment to reduce the amount of PVP. The final range in the TGA profile is above 400°C, where similar mass losses for all the samples (including alumina) occurred and most likely originated from γ-Al$_2$O$_3$ than from PVP. The TGA and CHN analyses performed in this study suggest that the aforementioned oxidation-reduction treatment can be successfully applied to the fresh catalysts before the catalytic reaction to remove the protecting polymer.

Fig. 2.3 presents the TEM images of the synthesised nanoparticles. No large agglomerates (above 5 nm) were observed, and the nanoparticles are near-spherical with narrow size distribution. Monometallic Ir nanoparticles are the smallest in size (1.6 ± 0.2 nm)[1]. The bimetallic Pd2Ir1 and Pd1Ir1 particles (2.2 nm diameter) are close in size to

---

[1] The ± sign and the numbers on its right hand side refer to one standard deviation in average TEM sizes that are reported.

monometallic Pd (2.3 ± 0.4 nm) but with wider size distribution (up to 1.0 nm). Pd(c)Ir(s)

sample shows the largest average size of 2.7 ± 0.5 nm indicating that the preformed core

Pd nanoparticles of 2.3 ± 0.4 nm diameter are coated with Ir atoms[1].
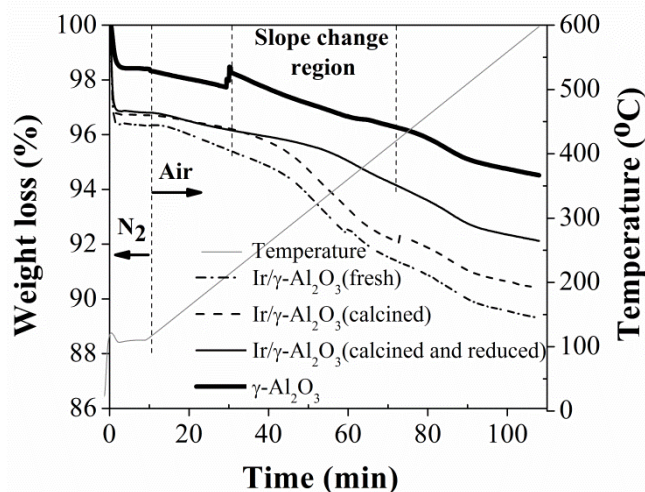
Fig. 2.2. TGA profiles of Ir/γ-Al$_2$O$_3$ pretreated at different conditions, i.e. (i) fresh, (ii) calcined in
air at 200°C for 1 h, and (iii) calcined in air at 200°C for 1 h followed by the reduction in hydrogen
at 359°C for 1 h, as used for the catalytic tests. Some predried γ-Al$_2$O$_3$ was also tested for
comparison. TGA programme: ramp from room temperature to 110°C under N$_2$, heating from
110°C to 600°C under air with the heating rate of 5°C/min.

The applied synthetic procedure for the Pd(c)Ir(s) nanoparticles ensures the desired

structure, as the Pd nanoparticles were synthesized first followed by Pd-H formation in hydrogen

atmosphere. The hydride serves as a catalyst for Ir reduction on the Pd nanoparticle surface. This

procedure, known as a hydrogen-sacrificial technique, is shown in Scheme 2.2. The supporting

Information (at the end of chapter) contains detailed explanations on how the stoichiometric

amount of Ir precursor to build a monolayer shell was determined.

---

[1] Nanoparticles used for TEM analyses were synthesized by Mrs. Jing Shen and TEM analyses were completed
by Mrs. Jing Shen and Dr. Cindy-Xing Yin. TEM images of Fig. 2.3 and Fig. 2.11 have been taken from Mrs.
Shen MSc. Thesis: "Bimetallic catalysts for low-pressure ring opening" submitted to University of Alberta
(2011).
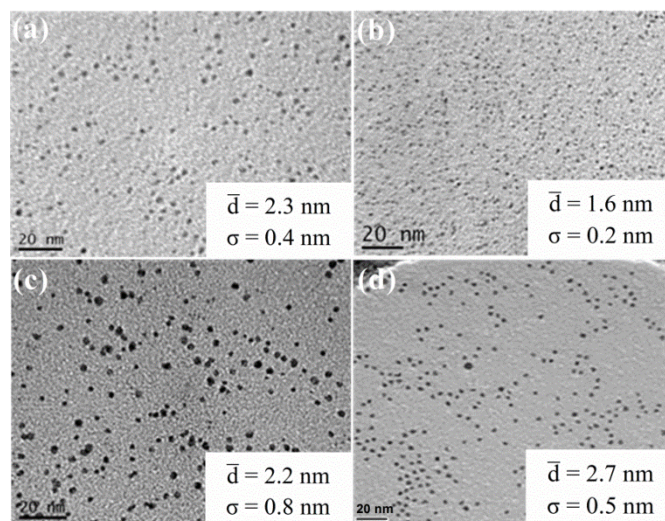
Fig. 2.3. TEM images with average size and one standard deviation for the various Pd and Ir containing nanoparticles: (a) Pd, (b) Ir, (c) Pd2Ir1, and (d) Pd(c)Ir(s). The image for Pd1Ir1 is not shown; the size is 2.3 ± 1.0 nm. The scale bars correspond to 20 nm.
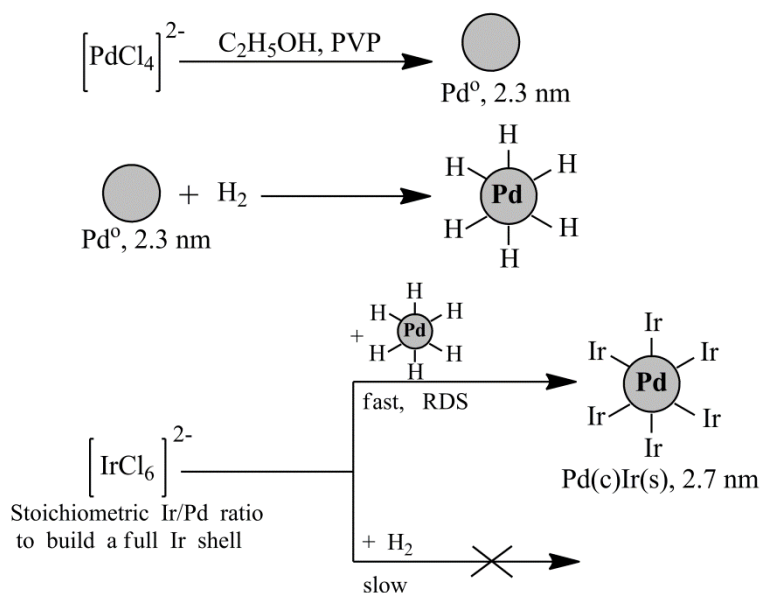
Scheme 2.2. Formation of Pd(c)Ir(s) nanoparticles by hydrogen-sacrificial reduction method.

The analyses below were performed to confirm the nanoparticle bimetallicity and structure, instead of physical mixture of the monometallic counterparts. STEM coupled with EDX of the Pd(c)Ir(s)/γ-Al$_2$O$_3$ (Fig. 2.4) revealed a uniform distribution of the

nanoparticles on γ-Al$_2$O$_3$ due to a proper choice of the support, i.e., the used alumina has an average pore size of 5.8 nm so that the nanoparticles can be easily accommodated within the support pores. The presence of Al, O, Pd, and Ir was confirmed on the surface; however, due to the limited resolution, the bimetallic nanoparticles could not be differentiated either in a layered structure of Pd and Ir atoms (core-shell) or randomly mixed together (alloy)[1].
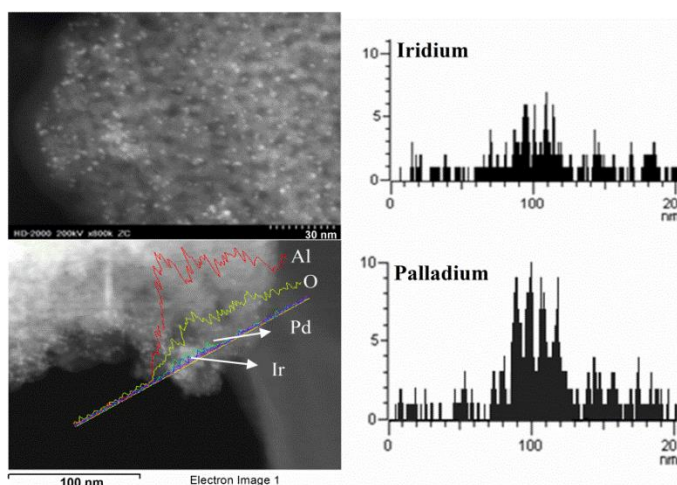
Fig. 2.4. The STEM image with Pd and Ir EDX profiles of the Pd(c)Ir(s) nanoparticle supported on γ-Al$_2$O$_3$.

Fig. 2.5 shows the H$_2$-TPR profiles of the selected catalysts. For the monometallic Pd, the low-temperature negative peak can be ascribed to hydrogen evolution due to Pd-β hydride decomposition [65]. The TPR profile of the monometallic Ir shows a hydrogen consumption peak near 190°C, which is in agreement with the literature data on the reduction of IrO$_x$ species [55]. When a physical mixture of the monometallic Ir and Pd catalysts was inserted to the TPR cell, the TPR profile, expectedly, shows the summation of the less intense signals for the monoPd and monoIr. However, the TPR profiles of the

---

[1] The STEM-EDX analysis was performed at the Centre for Nanostructure Imaging, Department of Chemistry, University of Toronto

Pd1Ir1 and Pd(c)Ir(s) catalysts show different trends compared to their monometallic counterparts, with no distinct hydrogen evolution for the Pd component and a broad peak over the low temperature region (75°C-300°C) for the Pd(c)Ir(s). The change of the reducibility characteristics of a specific metal upon alloying is a typical phenomenon in bimetallic catalysts [55,64,65] and indicative of the formation of new bimetallic clusters, not the physically mixed monometallic particles[1].
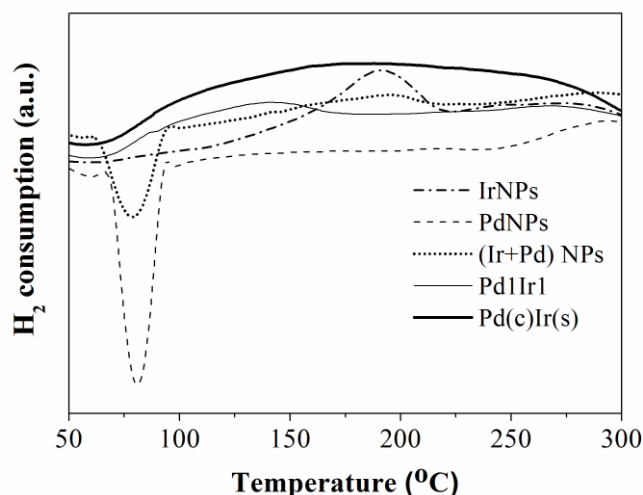
Fig. 2.5. H$_2$-TPR profiles of the selected catalysts in 10 ml/min mixture of 10% H$_2$ in Ar (heating rate: 5°C/min).

XPS analysis was also performed on selected monometallic and bimetallic catalysts. No chlorine residuals from the precursor were found in XPS survey scan. The XPS spectra of the Pd *3d* and Ir *4f* are presented in Table 2.1 and Figs. 2.6 and 2.7. The binding energy (BE) values of 334.6 and 335.7 eV for Pd *3d$_{5/2}$* in mono Pd/γ-Al$_2$O$_3$ can be assigned to the pure and oxide Pd species, respectively [66,67]. The BEs of 60.7 and 62.2 eV for Ir *4f$_{7/2}$* in monoIr/γ-Al$_2$O$_3$ correspond to the reported numbers for pure and oxidized

---

[1] A version of the material of this paragraph (only) has been published in: H. Ziaei-Azad, C.-X. Yin, J. Shen, Y. Hu, D. Karpuzov and N. Semagina, *Journal of Catalysis* 304 (2013) 149 (as a Corrigendum). Reprinted with permission from Elsevier.

Ir [68,69], which forms during the catalyst handling in air even at room temperature [70]. The bimetallic samples exhibited shifts in the BE values as compared to their monometallic counterparts, which can imply the metal alloying. Starting with Pd1Ir1, the BE values of Pd $3d_{5/2}$ shifted to higher values of 335.4 and 336.2 eV for the metallic and oxidized Pd, respectively. Ir $4f_{7/2}$ BE values shifted to lower values (60.6 and 61.4 eV for the metallic and oxidized Ir). These shifts are in line with electron affinities of Pd (54 kJ mol^{-1}) and Ir (151 kJ mol^{-1}), which are indicative of the electron-donating properties of Pd in this bimetallic combination. Similar shift trends exist for the Pd(c)Ir(s) catalyst, but they are less significant, most likely due to the fact that the there are fewer Pd-Ir neighbours in the core-shell combination as compared to the uniformly mixed Pd1Ir1 nanoparticles. The area percentage of the metallic Pd peaks are 47, 58 and 67 % of the total Pd peak areas for monoPd, Pd1Ir1 and Pd(c)Ir(s), respectively, which imply the higher percentage of metallic Pd in Pd(c)Ir(s) as it is protected by the shell Ir layer from oxidation[1].

Table 2.1. XPS binding energy values of Pd and Ir in selected samples after the calcination-reduction pretreatment.

Catalyst (support:γ-Al$_2$O$_3$)	Binding energy (eV)				Zero-oxidation state, %	
	Pd 3d$_{5/2}$		Ir 4f$_{7/2}$		Pd	Ir
Pd	334.6[a]	335.7[b]			47	
Pd1Ir1	335.4	336.2	60.6	61.4	58	55
Pd(c)Ir(s)	334.7	335.9	60.0	61.3	67	59
Ir			60.7	62.2		49

[a] Values correspond to 0-valent and oxidised metal, as seen in Figs. 2.6 and 2.7.
[b] Values correspond to 0-valent and oxidised metal, as seen in Figs. 2.6 and 2.7.

Ion scattering spectroscopy (ISS) was also performed on mono- and bimetallic catalysts (Fig. 2.8) to provide information on the outer surface layer of the bimetallic

formulations. Although quantitative analysis is limited by the uncertainty of the inelastic losses and the neutralization rate depending on ion trajectories [71], the spectra indicate roughly similar amounts of Pd and Ir in Pd1Ir1 sample and significant abundance of Ir (~ 5-fold) in the outer shell of Pd(c)Ir(s) catalyst. This result confirms that Ir was successfully deposited on Pd nanoparticles following the hydrogen-sacrificial technique (Scheme 2.2).
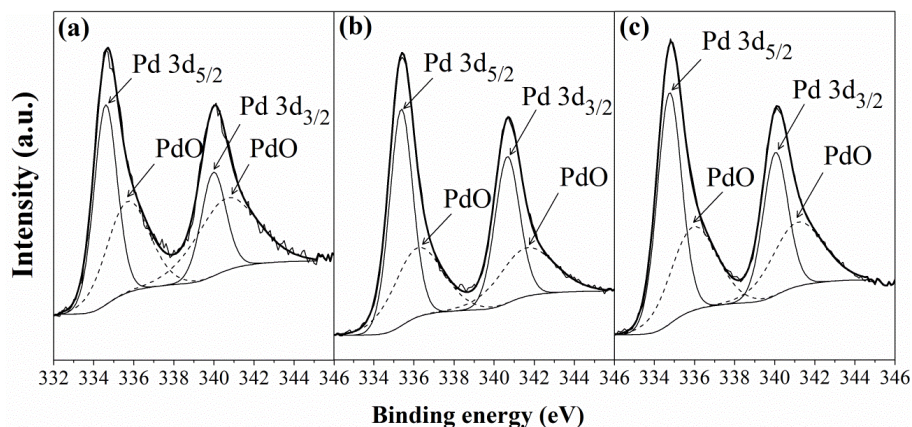
Fig. 2.6. Pd 3d XPS spectra of the selected γ-Al$_2$O$_3$-supported catalysts: (a) Pd, (b) Pd1Ir1 and (c) Pd(c)Ir(s).
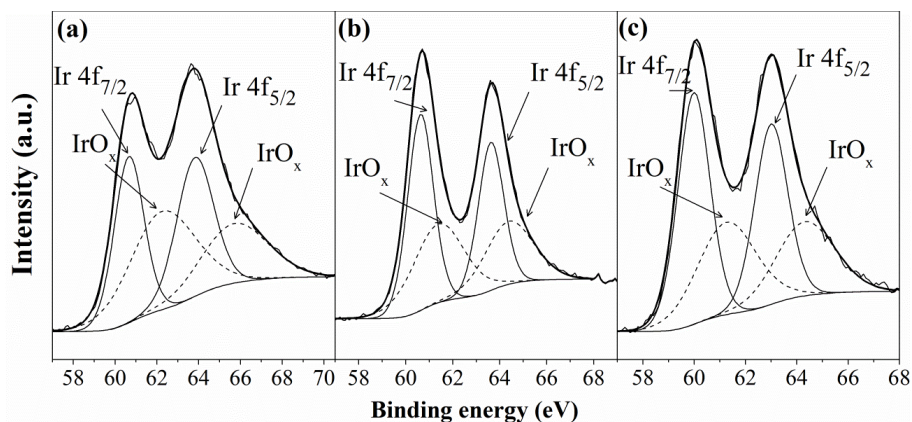
Fig. 2.7. Ir 4f XPS spectra of the selected γ-Al$_2$O$_3$-supported catalysts: (a) Ir, (b) Pd1Ir1 and (c) Pd(c)Ir(s).

Pd L$_3$-edge XANES spectra were also recorded; the nanoparticle monodispersity made them excellent samples for this analysis. All the spectra have been normalised using

the Athena software so that the edge jump intensity can be compared directly. The peak on the rising edge of the XANES profiles in Fig. 2.9 (also refer as "white line") is due to excitations of Pd $2p_{1/2}$ electrons to the unoccupied Pd $4d$ orbitals, and its intensity is proportional to the degree of valence electrons' occupancy of the absorber [72]. The change in the white line intensity and the peak position are reported as a possible indication of the change in the oxidation state of the absorbing metal [73]. As seen in Fig. 2.9, all three presumably bimetallic formulations exhibit peaks at higher energies as compared to monometallic Pd foil and monometallic Pd nanoparticles, as well as larger peak intensities, indicating higher positive charge on Pd in bimetallic catalysts (it takes more energy to remove Pd $2p$ electrons from oxidized Pd). The shift to higher energy values as compared both to Pd foil and Pd nanoparticles is significant (0.4 - 0.5 eV for Pd nanoparticles) and it is larger than the instrumental error (the beamline resolution is 0.3 eV, and 0.2 eV step size was used in the scan). This observation may again confirm the bimetallic structure of the Pd-Ir catalysts, instead of physical mixtures of monometallic Pd and Ir nanoparticles[1].
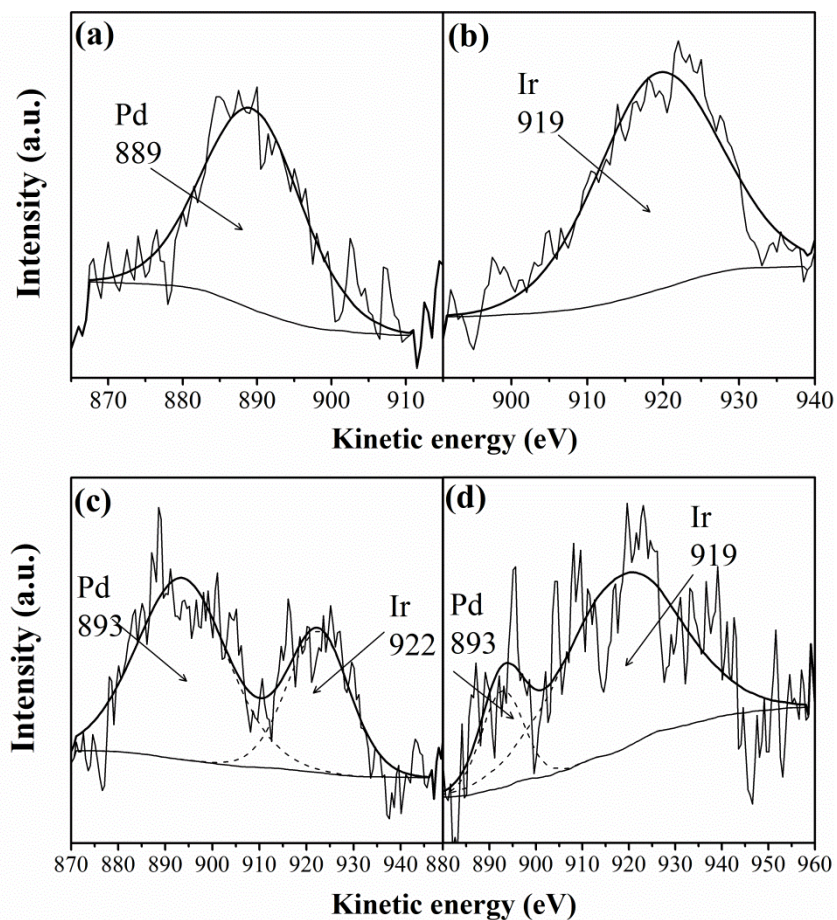
Fig. 2.8. Ion scattering spectra of the selected γ-Al$_2$O$_3$-supported catalysts: (a) Pd, (b) Ir, (c) Pd1Ir1 and (d) Pd(c)Ir(s).
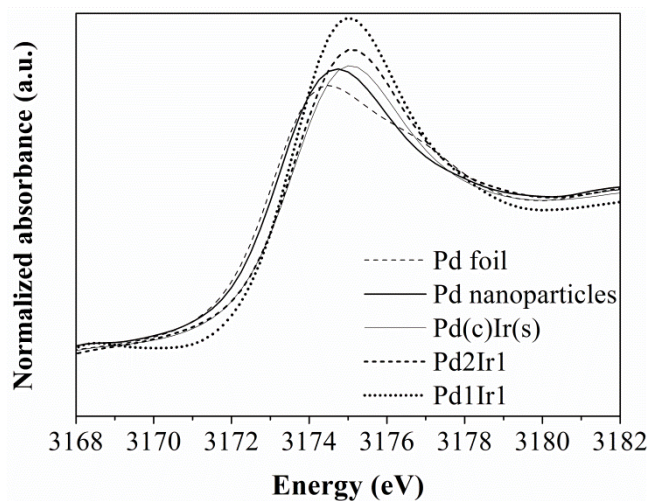
Fig. 2.9. Pd L$_3$-edge XANES spectra of the selected nanoparticles supported on γ-Al$_2$O$_3$. Pd foil was used as the reference.

From Fig. 9 one can compare the intensities by calculating the peak areas, which vary in the order of Pd1Ir1>Pd2Ir1> Pd(c)Ir(s)>Pd nanoparticles. This can be interpreted as the Pd in Pd1Ir1 having relatively more positive charge, while that of the Pd(c)Ir(s) seems to be more metal-like. The electron affinity of Ir (112 kJ/mol) is higher than that of Pd (54 kJ/mol), indicating electron-accepting properties of Ir, which result in more positive Pd in bimetallic structures. This phenomenon is more pronounced in Pd1Ir1 probably due to the higher Ir-to-Pd ratio in this sample as compared to Pd2Ir1. Among the bimetallic structures, the least intense edge jump is observed for Pd(c)Ir(s), even though its Ir-to-Pd ratio is in between those for Pd1Ir1 and Pd2Ir1 samples. It is likely that the Pd-Ir contact in Pd1Ir1 and Pd2Ir1 is more profound than that of the core-shell structure and the formation of alloy structure is more likely for the Pd1Ir1 and Pd2Ir1 samples (herein, under the alloy structure a nanoparticle composed of mixed Pd-Ir atoms in all nanoparticle shells is assumed). One the other hand, the lower white line intensity of the Pd(c)Ir(s) compared to Pd2Ir1 (about 10% less) may be similarly attributed to the lower contact of Pd-Ir in the former. Indeed, for the core-shell structure only the surface Pd atoms of the Pd core are in contact with Ir shell atoms, resulting in higher ratio of Pd-Pd bonds compared with the Pd-Ir ones. As a result, the XANES profile of this structure looks more like that of the Pd monometallic nanoparticles but the peak is still shifted towards higher energy values (the same as for alloy PdIr catalysts) indicating the nanoparticle bimetallicity. These results may suggest that the hydrogen sacrificial strategy has been effective in producing the targeted Pd(c)Ir(s) nanoparticle structure and that the simultaneous reduction resulted in bimetallic structures instead of a physical mixture of monometallic Pd and Ir nanoparticles.

Thus, monometallic Ir and Pd as well as bimetallic PdIr nanoparticles were synthesised with narrow size distribution and controlled structure, which makes them invaluable tool in finding correlations between the bimetallic nanoparticle compositions with its catalytic properties without possible size effects.

2.3.2. Catalytic behaviour in indane ring opening[1]

The indane conversion, single cleavage selectivity and product distribution are presented in Figs. 2.10a, 2.10b and Tables 2.2 and 2.3. As seen, the Pd monometallic nanoparticles are not active for the RO of indane. In contrast, the Ir monometallic catalyst shows the highest conversion (99%) among the synthetic nanoparticles. The presence of Ir in the bimetallic catalysts ensures their higher activity as compared to pure Pd. Notably, as seen from Table 2.2, similar Ir loadings in the reactor (in the range of 0.6 mg – 0.84 mg), lead to a range of conversions from 9% to 91% depending on the bimetallic structure, which makes the possibility of controlling the structure of crucial importance. The highest conversion for a bimetallic catalyst is achieved with Pd(core) and Ir(shell) structure. Our working hypothesis was that the Ir atoms forming one outer layer around a Pd core display similar catalytic properties as the surface atoms on the monometallic Ir nanoparticles. The atmospheric ring opening of naphthenic rings is a metal-driven reaction, which is essentially controlled by the accessibility of the surface metal [44]. The f.c.c. cuboctahedral crystal surface statistics was applied for the Pd and Ir monometallic particles with 2.3 nm and 1.6 nm diameters to find the metal dispersion as 46% and 61%, respectively [74], which allowed calculating the activity per surface Ir atoms of the

---

monometallic particles (Table 2.2). For the Pd(core) Ir(shell) particles, the statistics were applied for the core Pd particles covered with one extra layer of Ir atoms. The calculation details are presented in the Supporting Information; the amount of Ir in the sample is enough (or nearly enough) to build one full Ir shell around the Pd core, which results in 100% Ir dispersion. Based on the found dispersions of monometallic Ir and Pd(c)Ir(s), the activities per surface Ir atoms were found as 3.6×10^{-2} g_{indane} / $g_{surface\ Ir}$ / min irrespectively of the catalyst mono- or bimetallicity, indicating the absence of either antagonism or synergism between the two metals arranged in the core-shell structure with one layer of Ir atoms. External Pd core atoms, located in the close proximity to the covering Ir atoms, which would allow for the electron transfer between the metals, do not affect the Ir atoms electronic properties enough to change their activity in indane ring opening. In this bimetallic structure, the role of a second metal (Pd) is only in being an inert support allowing 100% dispersion of the active Ir metal.
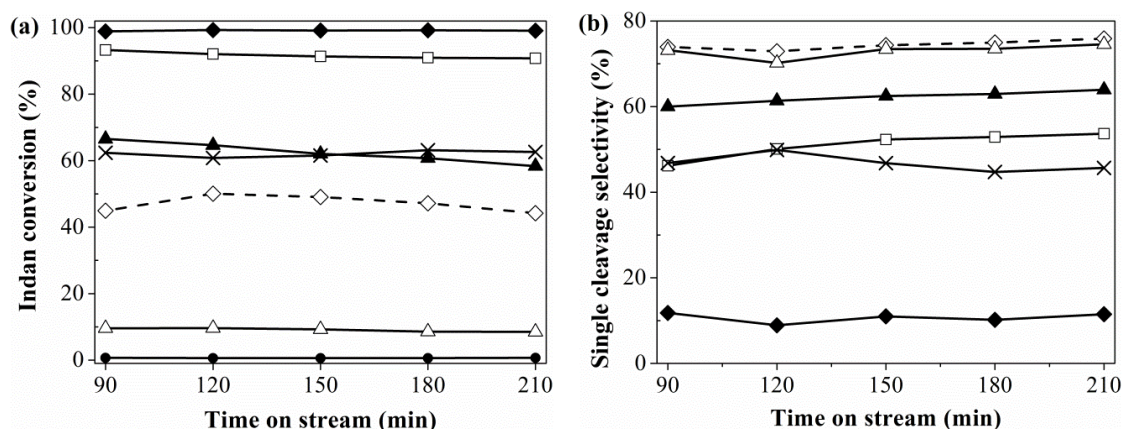
Fig. 2.10. Indane conversion (a) and single cleavage selectivity (b) vs. time-on-stream over different γ-Al$_2$O$_3$-supported nanoparticles at 336°C and 0.1 MPa: Pd nanoparticles (●), Ir nanoparticles (♦), Ir nanoparticles (half amount) (◊), Pd2Ir1 (Δ), Pd1Ir1 (▲), Pd(c)Ir(s) (□), and industrial Pt–Ir catalyst (×).

Table 2.2. Catalytic performance of the synthesized and industrial catalysts in atmospheric indane ring opening at 336°C.

Catalyst (support: γ-Al$_2$O$_3$)	Nano-particle size[b], nm	Pd / Ir loadings, wt.%	Conver-sion[c], %	Single cleavage selectivity / yield, %	Ir loading in the reactor, mg	Ir disper-sion[d], %	Surface Ir in the reactor, mg	Activity, 10^{-2} g_{indane} / $g_{surface\ Ir}$ / min	PB/ET ratio / PB yield
Pd	2.3±0.4	0.160 / 0	1	N/A	N/A	N/A	N/A	-	-
Ir	1.6±0.2	0 / 0.178	99	10 / 10	1.20	61	0.73	3.8	<0.09 / <1
Ir (half amount[a])	1.6±0.2	0 / 0.178	48	75 / 36	0.60	61	0.37	3.6	0.19 / 6
Pd2Ir1	2.2±0.8	0.091 / 0.098	9	73 / 7	0.62	46	0.29	0.9	0.17 / 1
Pd1Ir1	2.3±1.0	0.047 / 0.11	61	63 / 39	0.84	46	0.39	4.4	0.11 / 4
Pd(c)Ir(s)	2.7±0.5	0.269 / 0.385	91	52 / 48	0.71	100	0.71	3.6	0.15 / 6
Industrial Pt-Ir	N/A	N/A	62	47 / 29	N/A	N/A	N/A	N/A	0.15 / 4

[a] 0.6 mg of Ir in the reactor vs. 1.2 mg of the active metal(s) in all other reactions including for the industrial catalyst.
[b] the TEM diameter of the as-prepared nanoparticles.
[c] average values between 120 and 210 min on stream.
[d] the calculation details can be found in the Supporting Information.
[e] PB: n-propylbenzene, ET: 2-ethyltoluene.

Other bimetallic "alloy" structures Pd1Ir1 and Pd2Ir1 showed intermediate activities between monometallic Pd and Ir catalysts. Due to similar sizes (2.3 nm and 2.2 nm, vs. 2.3 nm for monometallic Pd), the nanoparticle dispersion in all the catalysts is 46% (see Supporting Information for the calculation details). As a working hypothesis, a uniform mixing of Pd and Ir atoms in the nanoparticles was assumed, implying that there is no Ir abundance either on the surface or in the core of the nanoparticles. With these assumptions, the activities per surface Ir atoms were found as being 4.4×10^{-2} and 0.9×10^{-2} g_{indane} / $g_{surface\ Ir}$ / min for Pd1Ir1 and Pd2Ir1 catalysts, respectively. The first value may be considered as being in line with the surface Ir activity in the monometallic or core-shell

nanoparticles and confirms the hypothesis of the absence of Pd promoting effect on Ir. However, the second value can reflect any of the following scenarios (or their combinations): i) Ir deficiency in the particle shell, i.e., Pd and Ir non-uniform distribution in the bimetallic structure; ii) Pd inhibiting effect *via* electronic transfer, when Ir atoms have relatively high coordination number with respect to Pd atoms, which amount is the highest among the all catalysts; and iii) surface dilution of Ir atom ensembles with Pd atoms which hinders indane chemisorption. The first hypothesis is line with the literature for Pt-Ir reforming catalysts, which as shown by X-ray diffraction and EXAFS, have a platinum-rich surface and an iridium-enriched core [75]. Palladium, similar to platinum, with lower heat of sublimation than iridium (about 160 kcal/mol for Ir, 135 for Pt and 89 for Pd) has the lowest surface energy and so it is more preferable to concentrate on the bimetallic particle surface. However, in this case, the Pd1Ir1 catalyst would not exhibit its high activity, which under the assumption of uniform Pd and Ir mixing in Pd1Ir1 catalyst corresponds well to the activity of surface Ir atoms in monoIr and Pd(c)Ir(s) catalysts. In addition, the single cleavage selectivity decreases with the increase of surface iridium in the samples (Table 2.2). These results are in good agreement with the well-documented propensity of iridium for hydrogenolysis and cracking [4,37,44]. So, the first hypothesis may be declined for the presented PdIr catalysts; it is not excluded that after aging and/or prolong exposure to the high-temperature reaction conditions, the core enrichment with Ir may occur leading to the loss of activity. Similarly, the Pd inhibiting effect via electron transfer is unlikely due to the similarity of Ir atom properties located on monoIr, Pd1Ir1, and Pd(c)Ir(s) nanoparticles.

The third hypothesis on the Ir surface dilution is viable if we consider possible reaction mechanisms. Three mechanisms have been proposed for the RO over metal-supported catalysts (see Scheme 2.3[1]) [76]. First, the dicarbene mechanism, which results in the cleavage of unsubstituted secondary-secondary carbon atoms, necessitates the metal-carbon bonding of two carbon atoms standing perpendicular on the metal surface. The second mechanism, known as π-adsorbed olefin mode, requires the flat adsorption of three neighbouring carbon atoms, which can achieve cleavage at substituted C-C positions. And a third mechanism competes with the dicarbene mechanism and operates via a metallocyclobutane intermediate containing a metal atom and four carbon atoms, which allows the opening of substituted C-C bonds if an external methyl group is involved in the intermediate [76]. This mechanism, as reported, has higher activation energy than the dicarbene and can operate only when the dicarbene path is blocked [76]. The RO mechanism of alkyl and/or aromatic branched naphthenic rings greatly depends on the nature of the metal as well as its particle size and structure [45]. In general, RO on metals like Ir, Ru, Rh, and Pt-Ir mostly happen only on the unsubstituted carbons, while on others such as Pt, Pd, Pt-Pd, and Pt-Ni substituted ones are usually involved as well [42,45]. A very comprehensive study on the RO of several naphthenic molecules using different noble metals can be found in the literature [44]. Among the different noble metals investigated in the literature, iridium reportedly displays the strongest tendency to break unsubstituted C–C bonds via the dicarbene mechanism [76].

---

[1] Scheme 2.3 is not part of the published materials indicated in the beginning of the chapter 2. It is added here for clarification purpose only.

(I) Dicarbene mode   (II) π- Adsorbed olefin mode   (III) Metallocyclobutane mode
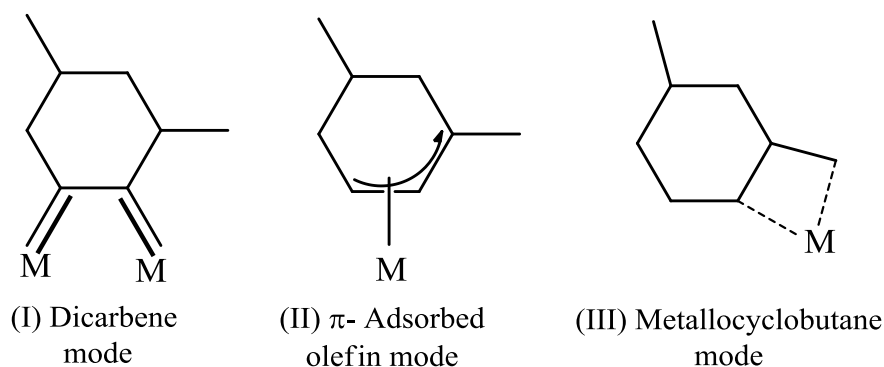
Scheme 2.3. A schematic representation of possible reaction mechanisms for ring opening reaction. Reprinted from [76] with the permission from Elsevier [1].

Table 2.3. Product distribution at 120 min on stream.

Catalyst (support: γ-Al$_2$O$_3$)	Product distribution, wt.%						
	2-ethyl-toluene	n-propyl-benzene	o-xylene	ethyl-benzene	toluene	benzene	lights
Ir	11	<1	45	4	22	2	17
Ir (half amount)[a]	31	6	7	1	3	<1	2
Pd2Ir1	6	1	1	<1	<1	<1	<1
Pd1Ir1	36	4	16	2	3	<1	4
Pd(c)Ir(s)	41	6	20	4	10	1	8
Industrial Pt-Ir	26	4	12	2	8	1	6

[a] 0.6 mg of Ir in the reactor vs. 1.2 mg of the active metal(s) in other runs; Pd is not included in the comparison due to low conversion.

From Table 2.3 presenting the product distribution, 2-ethyltoluene is the major product, while the portion of n-propylbenzene is much lower for all the samples, which is in line with the dicarbene mechanism [44,45,76]. The alternative olefin mode mechanism cannot be used to explain the presented results due to low selectivity to n-propylbenzene. The dicarbene mode requires two contiguous Ir atoms on the surface, and assuming one active site consisting of two neighboring Ir atoms, a Pd1Ir1 catalyst with 1:1 surface ratio of Pd-to-Ir atoms will display similar activities per each surface Ir atom

---

[1] Scheme 2.3 is not part of the published materials indicated in the beginning of the chapter 2. It is added here for clarification purpose only.

(Table 2.2, 4.4×10^{-2} g_{indane} / $g_{surface\ Ir}$ / min) or per ensemble of two surface atoms (8.8×10^{-2} g_{indane} / $g_{Ir\ active\ site}$ / min) as monometallic Ir or Pd(c)Ir(s) nanoparticles ($3 \times 6 \cdot 10^{-2}$ g_{indane} / $g_{surface\ Ir}$ / min or 7.2×10^{-2} g_{indane} / $g_{Ir\ active\ site}$ / min). The small difference may be attributed to the rounding up the Pd-to-Ir ratio to 1-to-1 which is 0.8-to-1 according to the NAA results, so more Ir ensembles exist on the catalyst surface resulting in higher specific activity of 8.8 vs. 7.2 for the monoIr. However, the Pd2Ir1 catalyst with 2-to-1 Pd-to-Ir surface atom ratio possesses the lower proportion of two-Ir-atom ensembles, which correlates with much lower activity of the Pd2Ir1 catalyst. The single cleavage selectivity (S) for all catalysts is also governed by Ir, irrespectively to its surroundings, and follows the conversion (X) trend: 73% S (9% X, Pd2Ir1) ~ 75% S (48% X, monoIr) > 63% S (61% X, Pd1Ir1) > 52% S (91% X, Pd(c)Ir(s)). Palladium's presence does not contribute to the cetane improvement number either: the *n*-propylbenzene-to-2-ethyltoluene ratio follows the same conversion trend being ~0.18 up to 50% conversion and ~0.13 up to 90% conversion (Table 2.2). Similarly, no significant improvement in the yield of single cleavage products obtained when Pt was added to Ir [37,77], which may point out the role of Pt only as the diluting material. This again confirms the Pd role only as a Ir surface diluting (for alloy catalysts) or dispersing (for core-shell) agent, with the catalytic properties governed by Ir active sites.

The existence of synergism in bimetallic formulations was widely reported for MCP ring opening. For instance, the MCP ring opening using Pt-Ru catalysts revealed a synergetic effect for Pt-Ru catalysts prepared by the amine precursors, which was explained as the formation of Pt-Ru dual surface sites [78]. In a recent study, a synergetic behaviour was reported for the RO of MCP over Pt-Ir/γ-Al$_2$O$_3$, where the bimetallic catalyst presented the conversion six-fold higher than Pt/γ-Al$_2$O$_3$ but two-fold lower than

Ir/γ-Al$_2$O$_3$. Such behaviour was attributed to the formation of new active sites between Pt and Ir [43]. However, the synergetic effects were not completely understood in both cases due to the incomplete knowledge over the structure of particles obtained via co-impregnation. Finally, in another recent study, Pt-Rh/Al$_2$O$_3$ catalysts were applied for the RO of MCP. The study showed that only the catalysts synthesised by refilling method (surface redox reaction), that possess large particles of greater than 1.7 nm, presented the improved activity and modified selectivity compared to Pt/Al$_2$O$_3$ [79]. Surface characterization and cyclohexane dehydrogenation probe reactions confirmed the presence of alloy structures for the particles of larger than 1.7 nm, and it was shown that under a hydrogen atmosphere the surface of the catalyst is enriched with Pt [80]. Bimetallicity also alters the selectivity of RO reactions. For instance, the incorporation of Pt into Ir moderates the cracking behaviour of iridium in the SRO of benzocyclopentane (indane) and improves the selectivity toward the single cleavage products [55]. Or, the addition of Ni to Ir/Al$_2$O$_3$ may improve the selectivity to higher octane number products in the RO of 1,3-dimethylcyclohexane (DMCH) [48]. However, all these findings were reported for the catalysts prepared via traditional impregnation techniques, which result in the active metal polydispersity and hinders the "one-particle" size effect studies [6].

The important significance of the current work is that by controlling the size and structure, including the surface structure, of mono- and bimetallic nanoparticles, we were able to distinguish two metal roles and establish the absence of any other Pd functioning apart from being an inert diluting or dispersing agent for active Ir. Our findings do not contradict the observed synergism hypotheses but allow verifying whether the intrinsic synergism exists. Indeed, according to the Table 2.2, similar Ir loadings in the reactor (in

the range of 0.6 mg – 0.8 mg) lead to a range of conversions from 9% to 91% for bimetallic structure, which could be assigned to antagonism and/or synergism between Pd and Ir. The possibility to control the nanoparticle structure, thus, to know its surface composition allowed us to reject the intrinsic synergism hypothesis and assign the observed synergism to the variations in active site architecture.

From the catalyst application point of view, for the same metal loading in the reactor, i.e., 1.2 mg of active metals(s), the synthesized Pd(c)Ir(s) nanoparticles display the highest selective ring opening yield (48%) among the various samples in this study, with a yield of about 19% higher than the commercial Pt-Ir catalyst (Table 2.2). As mentioned, a series of in-house Pt-Ir catalysts has been tested recently for the RO of indane at low pressure [55,77]; however, no significant improvement in the yield of single cleavage products was observed after the addition of Pt to Ir. Our Ir and Pd(c)Ir(s) nanoparticles also showed the absence of agglomeration under the reaction conditions (Fig. 2.11[1]). Although the ratio of *n*-proplylbenzene-to-2-ethyltoluene for the developed catalysts is the same as for the industrial catalyst, due to higher single cleavage selectivity, the Pd-Ir catalysts allow a higher yield of *n*-propylbenzene (Table 2.2), which is beneficial in terms of cetane number improvement.
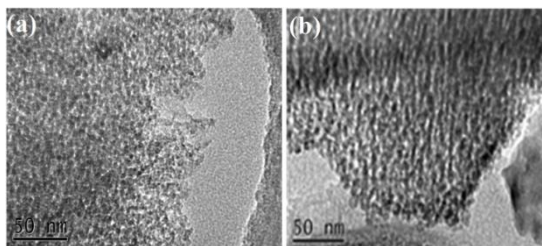
Fig. 2.11. TEM photographs of (a) Ir/γ-Al$_2$O$_3$ after the reaction, 210 min on stream; (b) Pd(c)Ir(s)/γ-Al$_2$O$_3$ after the reaction, 210 min on stream.

---

[1] Although no sign of agglomeration was observed in TEM images of supported catalysts after reaction, a size distribution histogram is not presented here because of the inaccuracy in determining the exact size of the metallic particles (fewer particles obtained in supported samples).

2.4. Conclusions

The engineered synthesis of Pd, Ir and Pd-Ir nanosized catalysts of 1.6 nm – 2.7 nm range enabled us to get insights into the Pd and Ir roles in the sulfur-free atmospheric ring opening of indane. Irrespective of the catalyst structure and composition, as soon as two contiguous surface Ir atoms exist on the nanoparticle surface, they display the same catalytic properties, most likely through the dicarbene ring opening mechanism. Palladium serves only either as a dispersing agent in Pd(core)–Ir(shell) structures providing 100% Ir dispersion or as a surface diluting inert metal in Pd-Ir formulations with mixed nanoparticle surface. The surface composition should be carefully controlled so that the Pd-to-Ir atom ratio on the surface does not exceed 1:1 to allow the existence of the two contiguous Ir atoms. No intrinsic synergism or antagonism between the two metals was found, while the conversion improvement (observed synergism) for some bimetallic formulations was seen in the catalytic runs. The ability to control and know the bimetallic nanoparticle surface structure is an indispensible tool in verifying whether intrinsic synergism exists between the two metals.

The hydrogen-sacrificial technique of liquid-phase colloid synthesis may allow the production of a very active and Pt-free catalyst formulation, i.e., Pd(c)Ir(s), which can be further examined in a sulfur feed under industrial conditions. This work is currently under way. With Ir being twice as expensive as Pd and one of the rarest elements on Earth, its 100% dispersion makes the Pd(c)Ir(s) catalyst preferable to the monometallic Ir. An increase of 19% in the yield of desired products was observed with the Pd(c)Ir(s) compared to a commercial Pt-Ir bimetallic catalyst, which may suggest Pd(c)Ir(s) as a potential candidate to reduce the consumption of platinum in refineries.

Acknowledgments

2.5. Supporting information

2.5.1. Dispersion calculations for monometallic and bimetallic nanoparticles

The dispersion calculations are based on the average nanoparticle diameter determined from TEM and crystal surface statistics described in detail by R. van Hardeveld and F. Hartog (Surface Science 15 (1969) 189-230).

Monometallic particles: The calculation parameters and results for the monometallic Pd and Ir particles are shown in Table 2.4. The total number of atoms is first determined based on the nanoparticle diameter, followed by finding the number of atoms on an equivalent edge m, which was further rounded to a non-zero natural number. This number was used to recalculate the total and surface number of atoms and metal dispersion.

Table 2.4. Surface statistics and dispersion for the monometallic nanoparticles

	Ir nanoparticles	Pd nanoparticles
Crystal structure	f.c.c. cuboctahedron	
Diameter from TEM, nm	1.6	2.3
Unit cell parameter a, nm	0.384	0.390
Volume of the unit cell a^3, nm^3	0.057	0.059
Number of atoms in the unit cell	4	
Number of atoms on an equivalent edge (including corner atoms) m	3	4
Total number of atoms in a nanoparticle, N_T	201	586
Number of surface atoms in a nanoparticle, N_S	122	272
Dispersion, N_S/N_T	0.61	0.46

Core-shell particles: The surface statistics were applied to the core Pd particles (the same as the monometallic Pd vide supra) covered with Ir atoms; the statistics can help reveal whether one complete or incomplete shell was built or several Ir shells. For simplicity, calculations are based on 1 g of the supported catalyst (0.269 wt.% Pd, 0.385 wt.% Ir). Total number of Pd atoms in 1 g catalyst using the Avogadro number is 1.52×1019. Using N_T from Table 2.4 the total number of nanoparticles is 2.59×1016. Ir crystals have a similar lattice parameter as the Pd one (see Table 2.4), so Ir atoms may be assumed to occupy the same volume in the bimetallic crystal as the Pd atoms. Assuming that Ir atoms build one full extra shell around the Pd core particles, for $m = 5$ total number of atoms in one particle can be found as 1289, i.e., the extra shell contains 703 atoms in one particle, or all particles in the sample should contain 1.82×1019 atoms. The real amount of Ir atoms in 1 g of the catalyst is 1.21×1019 atoms. Thus, the amount of Ir amounts in the catalyst is enough (or nearly enough) to build one full (or nearly full) Ir shell around the Pd core. In any of those cases, Ir dispersion is 100%.

Bimetallic PdIr nanoparticles of alloy structure, i.e., Pd2Ir1 and Pd1Ir1 samples: An additional assumption was made that the unit cell parameter a is an arithmetic average of a's for Ir and Pd due to the proximity of the values (0.384 and 0. 389 nm, respectively). As the working hypothesis, a uniform mixing of Pd and Ir atoms in the nanoparticles is assumed implying that there is no surface/core abundance of either of these metals.

Table 2.5. Surface statistics and dispersion for the bimetallic nanoparticles

	Pd2Ir1	Pd1Ir1
Crystal structure	f.c.c. cuboctahedron	
Diameter from TEM, nm	2.2	2.3
Unit cell parameter a, nm	0.387	
Volume of the unit cell a^3, nm^3	0.058	
Number of atoms in the unit cell	4	
Number of atoms on an equivalent edge (including corner atoms) m	4	
Total number of atoms in a nanoparticle, N_T	586	
Number of surface atoms in a nanoparticle, N_S	272	
Dispersion, N_S/N_T	0.46	

The above dispersions can be used with the metal loading values to find the amount of surface Ir for these two samples (see Table 2.2).

2.6. References

[1] G.C. Bond, A.F. Rawle, J. Mol. Catal. A: Chem. 109 (1996) 261-271.

[2] L. Guczi, Z. Schay, Gy. Stefler, L.F. Liotta, G. Deganello, A.M. Venezia, J. Catal. 182 (1999) 456-462.

[3] H.R. Aduriz, P. Bodnariuk, B. Coq, F. Figueras, J. Catal. 129 (1991) 47-57.

[4] J.L. Carter, G.B. McVicker, W. Weissman, W.S. Kmak, J.H. Sinfelt, Appl. Catal. 3 (1982) 321-346.

[5] B. Coq, F. Figueras, J. Mol. Catal. A: Chem. 173 (2001) 117-134.

[6] N. Semagina, L. Kiwi-Minsker, Catal. Rev. 51 (2009) 147-217.

[7] N.Toshima, H. Yan, Y. Shiraishi, in: G. Schmid, N. Toshima, B. Corain (Eds.), Metal Nanoclusters in Catalysis and Material Science: The Issue of Size Control, Elsevier Science, Amesterdam, (2008) 49-75.

[8] P. Lu, T. Teranishi, K. Asakura, M. Miyake, N. Toshima, J. Phys. Chem. B 103 (1999) 9673-9682.

[9] P. Lu, N. Toshima, Bull.Chem. Soc. Jpn. 73 (2000) 751-758.

[10] N. Toshima, Y. Wang, Langmuir 10 (1994) 4574-4580.

[11] C.-R. Bian, S. Suzuki, K. Asakura, L. Ping, N. Toshima, J. Phys. Chem. B 106 (2002) 8587-8598.

[12] N. Toshima, T. Yonezawa, K. Kushihash, J. Chem. Soc., Faraday Trans. 89 (1993) 2537-2543.

[13] N. Toshima, Y. Shiraishi, T. Teranishi, M. Miyake, T. Tominaga, H. Watanabe, W. Brijoux, H. Bonnemann, G. Schmid, Appl. Organomet. Chem. 15 (2001) 178-196.

[14] L.M. Bronstein, D.M. Chernyshov, I.O. Volkov, M.G. Ezernitskaya, P.M. Valetsky, V.G. Matveeva, E.M. Sulman, J. Catal. 196 (2000) 302-314.

[15] B. Zhao, N. Toshima, Chem. Express 5 (1990) 721-724.

[16] S.K. Singh, Q. Xu, Chem. Commun 46 (2010) 6545-6547.

[17] N. Toshima, K. Hirakawa, Appl. Surf. Sci. 121/122 (1997) 534-537.

[18] Y. Lou, M.M. Maye, L. Han, J. Luo, C.-J. Zhong, Chem. Commun. 5 (2001) 473-474.

[19] T.C. Deivaraja, J.Y. Lee, J. Electrochem. Soc. 151 (2004) A1832-A1835.

[20] T. Endo, T. Yoshimura, K. Esumi, J. Colloid Interface Sci. 286 (2005) 602-609.

[21] T. Endo, T. Kuno, T. Yoshimura, K. Esumi, J. Nanosci. Nanotechol. 5 (2005) 1875-1882.

[22] S.K. Ghosh, M. Mandal, S. Kundu, S. Nath, T. Pal, Appl. Catal. A 268 (2004) 61-66.

[23] L. Guczi, A. Beck, A. Horvath, Z. Koppany, G. Stefler, K. Frey, I. Sajo, O. Geszti, D. Bazin, J. Lynch, J. Mol. Catal. A: Chem. 204 (2003) 545-552.

[24] A.Q. Wang, C.M. Chang, C.Y. Mou, J. Phys. Chem. B 109 (2005) 18860-18867.

[25] X. Wang, W.B. Yue, M.S. He, M.H. Liu, J. Zhang, Z.F. Liu, Chem. Mater. 16 (2004) 799-805.

[26] G. Schmid, H. West, J. O. Halm, J. O. Bovin, C. Grenthe, Chem.-Eur. J. 2 (1996) 1099-1103.

[27] Y. Mizukoshi, T. Fujimoto, Y. Nagata, R. Oshima, Y. Maeda, J. Phys. Chem. B 104 (2000) 6028-6032.

[28] N. Toshima, Y. Shiraishi, A. Shiotsuki, D. Ikenaga, Y. Wang, Eur. Phys. J. D 16 (2001) 209-212.

[29] J. He, I. Ichinose, T. Kunitake, A. Nakao, Y. Shiraishi, N. Toshima, J. Am. Chem. Soc. 125 (2003) 11034-11040.

[30] A.U. Nilekar, S. Alayoglu, B. Eichhorn, M. Mavrikakis, J. Am. Chem. Soc. 132 (2010) 7418-7428.

[31] S.J. Cho, R. Ryoo, Catal. Lett. 97 (2004) 71-75.

[32] N. Toshima, Pure Appl. Chem. 72 (2000) 317-325.

[33] N. Toshima, K. Hirakawa, Polym. J. 31 (1999) 1127-1132.

[34] S.J. Cho, S.K. Kang, Catal. Today 93 (2004) 561-566.

[35] L. DSouza, S. Sampath, Langmuir 16 (2000) 8510-8517.

[36] J.H. Sinfelt, Catal. Today 53 (1999) 305-309.

[37] U. Nylen, L. Sassu, S. Melis, S. Jaras, M. Boutonnet, Appl. Catal. A 299 (2006) 1-13.

[38] M. Kangas, D. Kubicka, T. Salmi, D.Y. Murzin, Top. Catal. 53 (2010) 1172-1175.

[39] R.C. Santana, P.T. Do, M. Santikunaporn, W.E. Alvarez, J.D. Taylor, E.L. Sughrue, D.E. Resasco, Fuel 85 (2006) 643-656.

[40] F. Garin, P. Girard, F. Weisang, G. Maire, J. Catal. 70 (1981) 215-220.

[41] W.E. Alvarez, D.E. Resasco, J. Catal. 164 (1996) 467-476.

[42] D. Teschner, K. Matusek, Z. Paal, J. Catal. 192 (2000) 335-343.

[43] A. Djeddi, I. Fechete, F. Garin, Appl. Catal. A 413-414 (2012) 340-349.

[44] G. B. McVicker, M. Daage, M. S. Touvelle, C. W. Hudson, D. P. Klein, W. C. Baird Jr., B. R. Cook, J. G. Chen, S. Hantzer, D. E. W. Vaughan, E. S. Ellis, O. C. Feeley, J. Catal. 210 (2002) 137-148.

[45] H. Du, C. Fairbridge, H. Yang, Z. Ring, Appl. Catal. A 294 (2005) 1-21.

[46] F. Luck, J.L. Schmitt, G. Maire, React. Kinet. Catal. Lett. 21 (1982) 219-224.

[47] C.G. Walter, B. Coq, F. Figueras, M. Boulet, Appl. Catal. A 133 (1995) 95-102.

[48] S. Dokjampa, T. Rirksomboon, D.T.M. Phuong, D.E. Resasco, J. Mol. Catal. A: Chem. 274 (2007) 231-240.

[49] S. Lecarpentier, J.V. Gestel, K. Thomas, J.-P. Gilson, M. Houalla, J. Catal. 254 (2008) 49-63.

[50] R. Moraes, K. Thomas, S. Thomas, S.V. Donk, G. Grasso, J.-P., M. Houalla, J. Catal. 286 (2012) 62-77.

[51] D. Kubicka, N. Kumar, P. Maki-Arvela, M. Tiitta, V. Niemi, H. Karhu, T. Salmi, D.Yu. Murzin, J. Catal. 227 (2004) 313-327.

[52] D. Kubicka, M. Kangas, N. Kumar, M. Tiitta, M. Lindblad, D.Yu. Murzin, Top. Catal. 53 (2010) 1438-1445.

[53] J.-W. Park, K. Thomas, J.V. Gestel, J.-P. Gilson, C. Collet, Appl. Catal. A 388 (2010) 37-44.

[54] D. Kubicka, T. Salmi, M. Tiitta, D.Yu. Murzin, Fuel 88 (2009) 366-373.

[55] U. Nylen, J.F. Delgado,S. Jaras, M. Boutonnet, Appl. Catal. A 262 (2004) 189-200.

[56] J.G. Van Senden, E.H. Van Broekhoven, C.T.J. Wreesman, V. Ponec, J. Catal. 87 (1984) 468-477.

[57] T. Miyake, M. Teranishi, Chem. Mater. 10 (1998) 594-600.

[58] X. Yan, H. Liu, K.Y. Liew, J. Mater. Chem. 11 (2001) 3387-3391.

[59] X. Huang, Y. Wang, X. Liao, B. Shi, Chem. Commun. 35 (2009) 4687-4689.

[60] S. Link, M.A. El-Sayed, J. Phys. Chem. B 103 (1999) 8410-8426.

[61] R.M. Rioux, H. Songa, M. Grass, S. Habas, K. Niesz, J.D. Hoefelmeyer, P. Yang, G.A. Somorjai,Top. Catal. 39 (2006) 167-174.

[62] S.K. Matam, E.H. Otal, M.H. Aguirre, A. Winkler, A. Ulrich, D. Rentsch, A. Weidenkaff, D. Ferri, Catal. Today 184 (2012) 237-244.

[63] N.S. Babu, N. Lingaiah, R. Gopinath, P.S.S. Reddy, P.S.S. Prasad, J. Phys. Chem. C 111 (2007) 6447-6453.

[64] Y.-J. Huang, J. Xue, J.A. Schwarz, J. Catal. 111 (1988) 59-66.

[65] J. Batista, A. Pintar, D. Mandrino, M. Jenko, V. Martin, Appl. Catal. A 206 (2001) 113-124.

[66] K.S. Kim, A.F. Gossmann, N. Winograd, Anal. Chem. 46 (1974) 197-200.

[67] A.B. Gaspar, L.C. Dieguez, Appl. Catal. A 201 (2000) 241-251.

[68] R. Nyholm, A. Berndtsson, N. Martensson, J. Phys. C: Solid State Phys. 13 (1980) L1091-L1096.

[69] F. Bernardi, J.D. Scholten, G.H. Fecher, J. Dupont, J. Morais, Chem. Phys. Lett. 479 (2009) 113-116.

[70] F. Locatelli, B. Didillon, D. Uzio, G. Niccolai, J. P. Candy, J. M. Basset, J. Catal. 193 (2000) 154-160.

[71] J. Shen, X. Yin, D. Karpuzov, N. Semagina, Catal. Sci. Technol. 3 (2013) 208-221.

[72] J.A. Horsley, J. Chem. Phys. 76 (1982) 1451-1458.

[73] B.J. Hwang, C.-H. Chen, L.S. Sarma, J.-M. Chen, G.-R. Wang, M.-T. Tang, D.-G. Liu, J.-F. Lee, J. Phys. Chem. B 110 (2006) 6475-6482.

[74] R.V. Hardeveld, F. Hartog, Surf. Sci. 15 (1969) 189-230.

[75] J.H. Sinfelt, Bimetallic Catalysts: Discoveries, Concepts and Applications, John Wiely & Sons ,Inc., New York, (1983) 94.

[76] P.T. Do, W.E. Alvarez, D.E. Resasco, J. Catal. 238 (2006) 477-488.

[77] U. Nylen, B. Pawelec, M. Boutonnet, J.L.G. Fierro, Appl. Catal. A 299 (2006) 14-29.

[78] G. Diaz, F. Garin, G. Maire, S. Alerasool, R.D. Gonzalez, Appl. Catal. A 124 (1995) 33-46.

[79] P. Samoila, M. Boutzeloit, C. Especel, F. Epron, P. Marecot, Appl. Catal. A 369 (2009) 104-112.

[80] P. Samoila, M. Boutzeloit, C. Especel, F. Epron, P. Marecot, J. Catal. 276 (2010) 237-248.

Chapter 4: Nickel boosts ring opening activity of iridium[1]

4.1. Introduction

Catalytic ring opening (RO) is one of the key processes of increasing the quality of heavy polyaromatic and naphthenic compounds. During the process, a C-C bond on the ring is cleaved only once, leaving the number of carbon atoms in the product unchanged [1]. RO increases the volume of the products, and if substituted C-C bonds are the ones cleaved, it can also improve the cetane number. These are two important incentives for the oil market [2].

Since the 1970s, ring opening (RO) of cyclic compounds has been studied extensively using the Pt-group supported catalysts [1,3-7]. The RO of naphthenic rings relies on a metal-driven chemistry and among the different metals studied, Ir is the most selective and active ring opening catalyst [1,8,9]. The RO of several cyclic molecules such as methylcyclopentane, ethylcyclopentane, methylcyclohexane, dimethylcyclopentane, dimethylcyclohexane, indane, decalin, perhydroindane and trimethylcyclohexane has been studied using Ir supported catalysts [1,2,5-7,10-14]. Mechanism of the metal-catalysed RO of naphthenic rings depends on the nature of the metal, its particle size and support effects [8,15]. Iridium is reported to operate mostly via dicarbene mechanism, implying perpendicular adsorption of two carbon atoms of a naphthenic ring, which results in the cleavage of unsubstituted secondary-secondary carbon atom bonds [15]. The particle size effect in changing the mechanism of RO is reportedly less pronounced for Ir [16,17], as contrary to the platinum [17,18]. A study of the support effects in the RO of 1,3-

dimethylcyclohexane showed that Ir/SiO_2 is selective towards expected unsubstituted C-C bond cleavage, while Ir/Al_2O_3 presented also a significant selectivity for RO at substituted positions; this unusual behaviour was attributed to be the effect of support rather than the particle size [13].

However, Ir is one of the rarest elements on earth, a concern for the sustainable development. Is there a way to spare the metal without losing its outstanding catalytic performance? Could we place a much more inexpensive metal in the metal nanoparticle core, surrounded by only one layer of the expensive active noble metal, which would make all its atoms available for catalysis? Not with traditional preparation techniques for heterogeneous catalysts. Such techniques, like impregnation, exert limited control over particle size, particle structure, and vicinity between the two metals [19].

The controlled synthesis of bimetallic core-shell nanoparticles, developed about a decade ago, presents an attractive solution [20]. Colloid chemistry methods have synthesized bimetallic nanoparticles in a successful, controlled way in recent years, into various structures such as 'random alloy' and 'core/shell' [21]. A significant number of core/shell nanoparticles for catalytic applications have remained in the noble metal region: Au/Pd, Pd/Pt, Ru/Pt, Rh/Pt, Ir/Pt, Au/Pt, Au/Rh, and Pd/Ir [22-30]. Recent metal cores have comprised cheaper elements like Ni, Co, and Cu to prevent the waste of precious metals at bulk positions. However, to the best of our knowledge, synthesized nanoparticles have only been applied in low temperatures (rarely exceeding $120^{o}C$), or synthesized using relatively complicated methods. Some examples include a series of Co/M (M = Pd, Pt and Au) nanoparticles prepared by colloid chemistry (redox-transmetalation) [31], Ni/Pt and Ni/Pd nanoparticles synthesized by wet chemistry (polyol reduction) as the catalysts of PEM

fuel cells (operating typically at 50-100°C) or direct methanol fuel cells (90-120°C) [32,33], polyol-assisted synthesis of Ni/Pd for hydrogenation of nitrobenzene to aniline at 27°C [34], Co/Pt nanoparticles prepared by wet chemistry (redox-transmetalation) for hydrogenation of several compounds at room temperature [35], Ni/Pd nanoparticles synthesized by combined electrochemistry and wet chemistry methods, tested in a cross-coupling reaction at 65°C [36], and Cu/Pt nanoparticles synthesized by electrodeposition of Cu on carbon electrode followed by Pt shell formation, used in a study of PEM fuel cell catalysts [37].

The goal of the work is to replace a portion of Ir - one of the rarest elements on Earth - with the more abundant and less expensive Ni, without incurring any loss in catalytic performance per total Ir loading in a reactor. Indane ring opening is used as a model reaction, representing one of the routes in large-scale industrial fuel upgrading processes. Herein we report the synthesis of bimetallic nanoparticles of Ni and Ir either via simultaneous reduction of metal precursors in the presence of the stabilizing polymer polyvinylpyrrolidone (PVP), yielding supposedly alloy nanoparticles with random atom distribution, or via so-called hydrogen-sacrificial technique, when nickel hydride, formed by hydrogenation of preformed nickel nanoparticles, reduces and positions Ir atoms in the nanoparticle shell, creating supposedly 'Ni core- Ir shell' bimetallic particles (Ni(c)Ir(s), Scheme 4.1).

As will be shown by a variety of characterization techniques, after the high-temperature polymer removal, the particles either retain or change their initial size depending on the Ni-Ir ratio, and the supposedly core-shell sample indeed exhibits the expected nanoparticle shell enrichment with Ir atoms. Indane RO is studied at atmospheric

pressure and 350°C (Scheme 4.2). The RO products, when the ring is cleaved only once, are 2-ethyltoluene and n-propylbenzene.
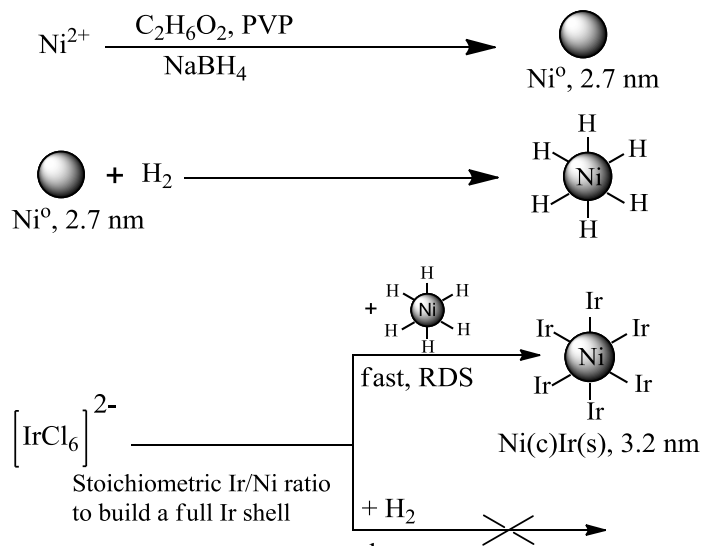
Scheme 4.1. Formation of Ni(c)Ir(s) nanoparticles by hydrogen-sacrificial method.
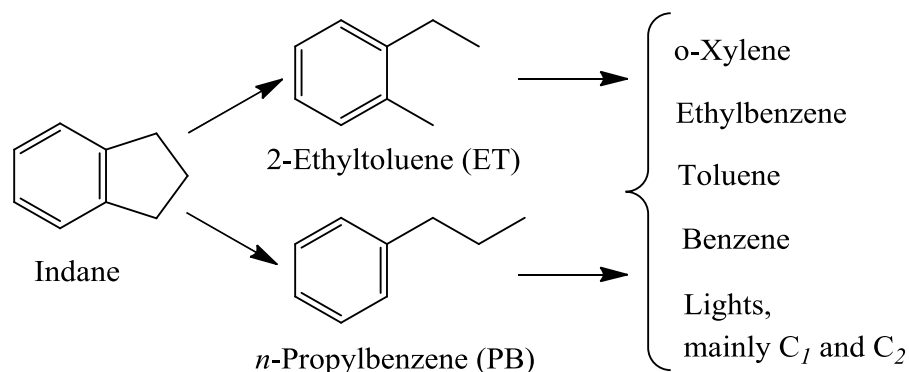
Scheme 4.2. The reaction scheme for ring opening of indane at atmospheric pressure and 350°C.

In the current work, we do not focus on selectivity improvement or cetane number increase, but on a material that will spare rare and expensive Ir, increase its activity per metal loading in the reactor, and bring no loss to the RO product yield. We only target the metal function of the material. As will be shown, the addition of Ni in the core position almost doubles RO activity with the same amount of active Ir in the reactor.

107

4.2. Experimental Section

4.2.1. Materials

Hydrogen hexachloroiridate (IV) hydrate ($H_2Cl_6Ir.xH2O$, Sigma-Aldrich), nickel chloride hexahydrate ($NiCl_2.6H_2O$, Sigma-Aldrich), polyvinylpyrrolidone (PVP, average molecular weight 40,000, Sigma-Aldrich), sodium borohydride ($NaBH_4$, Sigma-Aldrich), gamma alumina (γ-Al_2O_3, average pore size 58 Å, SSA 155 m^2/g, Sigma-Aldrich), ethylene glycol (Fischer-Scientific), and acetone (>99.7%, Fischer Scientific) were used as received. Nitrogen, argon, and hydrogen of ultra-high purity (99.999%) were purchased from Praxair. Benzocyclopentane (indane, 95% vol., Sigma-Aldrich) was distilled once.

4.2.2. Catalyst preparation

Ni and Ir mono- and bimetallic nanoparticles were preformed in a colloidal dispersion before deposition on γ-Al_2O_3. A modified polyol process, which applies a strong reducing agent, $NaBH_4$, was adapted for the synthesis of nanoparticles in this study. The method has precedent for Ni [70]. 0.1 mmol of either Ni or Ir metal precursor was dissolved in 25 ml of ethylene glycol and added to a 500-ml three neck flask. PVP was then added with the PVP/metal ratio of 40:1 and 20:1 (molar basis) to the Ni and Ir containing flasks, respectively. The final volume of the solution was increased to 175 ml by adding extra ethylene glycol. The resulting mixture was stirred vigorously under a constant flow of nitrogen and heated until the temperature reached 130-140°C. About 0.38 g of $NaBH_4$ was added to the flask at this temperature very quickly with adequate care. The reduction reaction happened immediately, the solution turned into dark brown with vapor release. Heating was continued until the mixture came to boil at ~ 197°C and then refluxed

in air for 1 h to complete the synthesis of PVP-protected nanoparticles. No precipitate was observed at the end of synthesis.

Bimetallic nanoparticles were synthesized with either simultaneous reduction of metal precursors (co-reduction) or the successive reduction assisted by hydrogen (hydrogen-sacrificial reduction method) to produce random alloy and core-shell particles, respectively. The PVP/(Ir +Ni) ratio of 20:1 (molar basis) was used for all the bimetallic nanoparticles. Three different Ni-Ir alloys with the molar ratios of Ni:Ir = 3:1, Ni:Ir = 1:1 and Ni:Ir = 1:3 were synthesized by the co-reduction of the metallic precursors. In all cases, 0.1 mmol of (Ni+Ir) was used and the same amount of $NaBH_4$ (0.38 g) was added at 130-140°C. The resulting colloidal solution obtained was always macroscopically homogeneous and transparent without any precipitate. Since the final Ni:Ir molar ratios in the γ-Al_2O_3 supported catalysts were found as 1.9:1, 0.9:1 and 1:3, respectively, hereafter they are referred as Ni2Ir1, Ni1Ir1 and Ni1Ir3. In addition to the alloy particles mentioned above, another bimetallic nanoparticle composition, Ni(core)-Ir(shell) was synthesized (with the molar ratio of 1:1) using the hydrogen-sacrificial reduction method, and referred as Ni(c)Ir(s). For the latter combination, Ni core nanoparticles were synthesized as vide supra. After the refluxing time, colloidal solution was allowed to cool down to room temperature followed by purging with hydrogen for 1.5 h. This procedure creates Ni hydride [40], which further serves to reduce Ir and forms an Ir shell around the preformed Ni nanoparticles. To build an Ir shell, 0.1 mmol of $H_2Cl_6Ir.xH_2O$ was dissolved in about 50 ml of ethylene glycol and added to the mixture of Ni nanoparticles drop by drop. A syringe pump (Fisher-Scientific 01001) was used to transfer Ir solution to the synthesis flask with the flow rate of about 20 ml/h. The synthesis flask was constantly purged with H_2 during

the addition of Ir and at least one hour afterwards. Each resulting colloidal dispersion was macroscopically homogeneous and transparent with no precipitate.

All synthesized nanoparticles were supported on pre-dried γ-Al_2O_3, using acetone to precipitate them [71]. About 800 ml acetone was added to the suspension of nanoparticles (in colloidal solution) and γ-Al_2O_3, and it was stirred vigorously for 2 h. Then, the supernate was removed from the beaker and the resulting powder was washed several times with acetone, dried at ambient overnight to form fresh catalysts, which then were calcined in air at 400^oC for 2 h to ensure PVP removal.

4.2.3. Catalyst Characterization

Formation of nanoparticles in the colloidal solution was studied by UV visible spectroscopy using a Varian Cary 50 Scan UV visible spectrometer with a 1 cm quartz cell.

Transmission electron microscopy (TEM) images of as synthesized and supported nanoparticles were recorded with a JEOL JEM2100 TEM device with a LaB_6 filament operating at 200 kV. The system was equipped with a Gatan GIF Tridiem energy filter with a 2k $\times$ 2k digital camera. Samples for TEM analysis were prepared by placing a drop of the colloidal dispersion of nanoparticles onto a carbon-coated copper grid, followed by the evaporation of the solvent in a vacuum oven at 50^oC. The average diameter and the standard deviation were calculated by counting over 200 particles using the ImageJ software. In the case of supported catalysts, 0.1 g of the sample was suspended in 5 ml of ethanol and dispersed in an ultrasonic bath for about 5 min before placing a drop of the suspension on TEM grid.

The loading of the Ni and Ir in the calcined catalysts were determined by neutron activation analysis (NAA) at the University of Alberta SLOWPOKE facility[1]. Samples were irradiated in the nuclear reactor for 600 s following a decay period of $\geq$ 24 h. Irradiated samples were individually counted for 600 s using a 22 % relative efficiency ORTEC hyperpure Ge detector housed in a 10 cm Pb cave. The Ge detector was connected to a PC-based Aptec multichannel analyser card.

Fresh and calcined supported catalysts were analyzed by an Elementar Vario Micro elemental analyser for CHN percentage.

Hydrogen temperature programmed reduction (H_2-TPR) was performed using an AutoChem 2950 HP device (Micromeritics). About 500 mg of the calcined catalysts was used for the analysis. Samples were initially reduced by 50 ml/min mixture of 10% H_2 in Ar up to 400°C for 1 h, cooled down to ambient and then oxidized by 50 ml/min of 10% O_2 in He to 400°C for 1 h. The TPR profiles were collected with a 10 ml/min mixture of 10% H_2 in Ar from ambient temperature to 400°C with a heating rate of 10°C/min. Peak deconvolution was performed using Origin software.

CO_2 temperature programmed desorption (CO_2-TPD) was performed with the same AutoChem 2950 HP device. About 250 mg of the similar calcined catalysts but with higher metal loading (about 1 wt.%) was used for this study since the Al_2O_3 also adsorbed CO_2. Before CO_2 adsorption, samples were initially outgassed in Ar at 300°C for 2 h, and then reduced by a mixture of 10% H_2 in Ar up to 400°C for 1 h. After the reduction pre-treatment, the active gas was switched to He and the temperature was brought down to 50°C. A mixture of 3% CO_2 in He was passed through the samples at 50°C for 1 h with the flow of 50 ml/min. Physically adsorbed CO_2 was then removed by flushing 50 ml/min of

---

[1] NAA analysis was done by Dr. John Duke at SLOWPOKE facility at the University of Alberta.

He at 50°C for 1 h. The TPD spectra were collected by flowing 20 ml/min He from ambient temperature to 300°C with a heating rate of 10°C/min.

Diffuse reflectance infrared Fourier transform spectroscopy (DRIFTS) of adsorbed carbon monoxide (CO) was performed with a Nicolet Nexus670 spectrophotometer, at a resolution of 4 cm^{-1} in the range of 800-3000 cm^{-1} and averaged over 128 scans. The Ni-Ir nanoparticles were supported on γ-Al$_2$O$_3$ with the higher loading of about 1 wt.%. Following the same calcination treatment, i.e. 2 h at 400°C in air, catalysts were reduced in the AutoChem 2950 with a flow of 50 ml/min of 10% H$_2$ in Ar from ambient to 400°C and kept for 1 h. Subsequently, they were allowed to cool down to room temperature under a flow of Ar and later a mixture of 3% CO in He with a flow of 50 ml/min was passed over the samples for about 45 min. CO adsorbed catalysts were further treated with a flow of Ar at room temperature for about 30 min to desorb the physically adsorbed CO; the DRIFTS spectra of the CO adsorbed catalysts were recorded immediately. Potassium bromide (KBr) from Sigma-Aldrich was dried at about 200°C overnight and used for collecting the background spectra. Samples were also diluted with KBr at the ratio of about 20 wt.% before placing in the DRIFTS cell. The reflectance spectra of the catalysts were transformed to Kubelka-Munk using the OMNIC software. OMNIC and Origin software were used for further data processing, visualisation and deconvolution of the spectra.

X-ray photoelectron spectroscopy (XPS) was performed using a Kratos Axis 165 X-ray photoelectron spectrometer with a mono Al Kα source operating at 15 mA and 14 kV[1]. The XPS analysis was done on pelletized samples that were calcined in air at 400°C for 2 h followed by the reduction in hydrogen at 400°C for 1 h. Background subtraction

---

[1] XPS analysis was done by Alberta Center for Surface Science and Engineering (ACSES) at the University of Alberta.

(Shirley-type), smoothing, and peak fitting were performed using the CasaXPS software package. All the core-level spectra were corrected with C 1s at 284.6 eV.

4.4.2. Catalytic behaviour in indane ring opening

Catalytic studies were performed at atmospheric pressure in a flow stainless steel reactor (length of 0.406 m, i.d. 0.013m). Calcined catalysts were diluted with about 2g #150 mesh SiC. Catalyst amounts corresponding to 0.8 mg Ir were used for each run except for monometallic Ni, where 0.8 mg Ni used. Gas flows were regulated with calibrated mass flow controllers (Sierra Instruments). The system was purged with Ar before and after each test. Catalysts were initially pre-treated in situ with 80 ml/min H_2 from ambient to 359°C for 1 h. Afterwards, the reactor temperature and the H_2 flow rate were changed to 350°C and 120 ml/min, respectively. The catalytic reaction started by bubbling hydrogen through the indane bubbler kept at the constant temperature water bath of 10°C that corresponds to 70.8 Pa indane partial pressure assuming saturation. The actual pressure was found as 68.4 Pa and indane flow rate of 2.8×10^{-5} g/min was confirmed with GC, which was calibrated with a Gilson HPLC pump. The reaction products were analyzed online every 25 minutes with a 430 Varian Gas chromatograph equipped with an FID detector; the details has been explained previously [30]. Each catalyst was tested for 200 min on stream and 6 data points were collected at 75, 100, 125, 150, 175 and 200 min. Results were repeatable within 2-5% experimental error. The absence of external and internal mass transfer limitations was verified experimentally by the Madon-Boudart method. Within the indicated times on stream, catalysts did not show significant deactivation. The reaction products were confirmed via an Agilent Technologies 7890 GC coupled with a 5975C MSD as described previously [30].

The desired single cleavage products of ring opening are 2-ethyltoluene and n-propylbenzene. Main dealkylation products are o-xylene, ethylbenzene, toluene, and benzene. Compounds with GC retention times less than that of benzene were named as 'lights'. The same main products were reported in ring opening of indane over Pt-Ir catalysts [7].

Selectivity values are reported not on mole, but on a mass basis (since up to 9 methane moles may be produced from a mole of indane). Response factors of different products with respect to indane were found by performing GC FID calibration with reference gas cylinders.

4.3. Results and Discussion

4.3.1. Characterization of as-synthesized nanoparticles

The synthesized Ni, Ir and Ni-Ir nanoparticles were analyzed by UV-vis spectroscopy and transmission electron microscopy (TEM). Figure 4.1 shows the UV-vis spectra during the synthesis of Ni1Ir1 colloidal dispersion as an example. No peak is discernible in the UV-vis range for PVP or ethylene glycol (EG) at room temperature. When metallic precursors are added to the solution, peaks occur at about 443 and 496 nm, which can be ascribed to the ligand-to-metal charge-transfer absorption of metallic ions [38]. As soon as the $NaBH_4$ is added, the mixture turns dark brown, a sign of nanoparticle formation. The UV-vis spectrum collected after reflux confirms that precursor peaks disappear and absorption increases in the visible region. Metallic nanoparticles absorb photons in UV-visible region due to the coherent oscillation of their conduction band electrons [39].
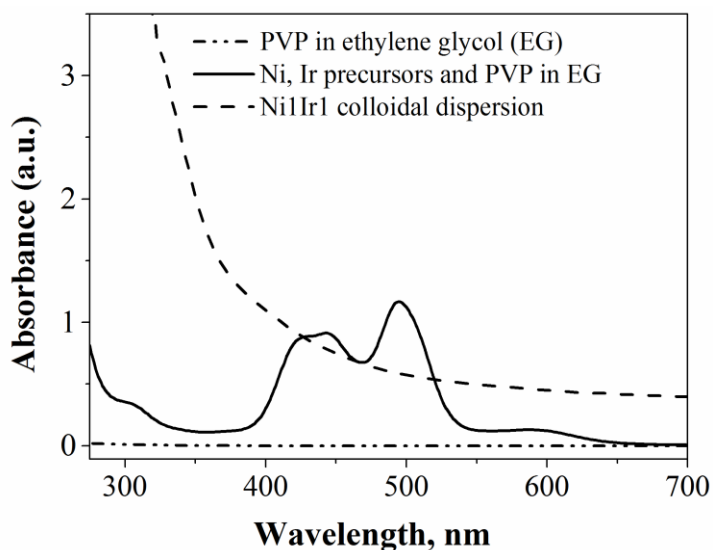
Figure 4.1. UV-vis spectra during the preparation of Ni1Ir1 colloidal dispersion.

Figure 4.2 presents size distribution histograms and an exemplary TEM image of the as synthesized nanoparticles[1]. Particles are nearly spherical with a narrow size distribution. The Ni(c)Ir(s) sample shows the largest size amongst all the synthesized nanoparticles (3.2 ± 0.6 nm), which implies the hydrogen-sacrificial technique successfully deposited Ir atoms on preformed core Ni particles (2.7 ± 0.7 nm). The technique, as shown in Scheme 4.1, provides the colloidal Ni core particles with hydrogen, which forms Ni-H [40]. The hydride species then catalyse the reduction of iridium ions on the surface of Ni core particles, forming core/shell particles. We have recently used this technique to synthesize Pd(c)Ir(s) particles [30].

---

[1] The σ in TEM images or the ± sign appearing with TEM sizes refer to one standard deviation in average sizes that are reported.
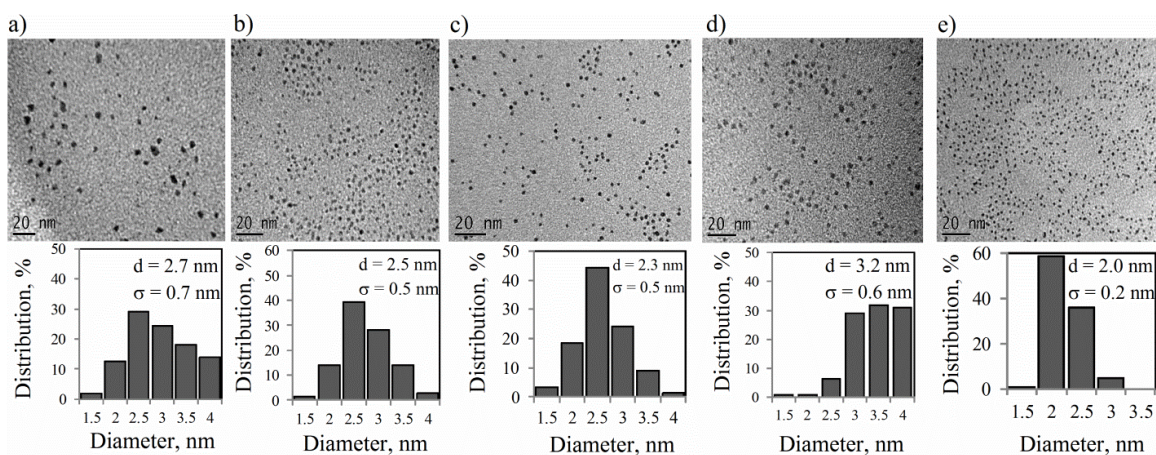
Figure 4.2. Size distribution histograms and the corresponding TEM images: (a) Ni, (b) Ni2Ir1, (c) Ni1Ir1, (d) Ni(c)Ir(s) and (e) Ir.

Figure 4.3 shows H_2-TPR profiles of selected samples along with deconvoluted peaks for each graph. There were three peaks in the TPR profile of monometallic Ir at 120, 200 and 272°C after deconvolution. The peak at 120°C may represent the reduction of highly dispersed surface Ir species, which agrees with other results [6]. The major peak at 200°C indicates IrO_2 reduction, which is formed during the calcination period before the TPR [41,42], while the peak centered at 272°C resembles documented results for Ir/γ-Al_2O_3 calcined at 420°C, attributed to the reduction of O-rich complexes [41]. The TPR spectrum of Ni/γ-Al_2O_3 shows a major peak at 219°C (reduction of NiO phase) [43], followed by two smaller peaks at 258 and 316°C. The latter peaks may show Ni species interacting with the support or the reduction of bulk Ni, since Ni sinters upon calcination as shown below, or both [13].

The deconvolution of bimetallic catalysts' TPR profiles was initiated by assuming the same reduction temperatures as in monometallic samples; a fit could indicate the absence of bimetallic interactions.

116
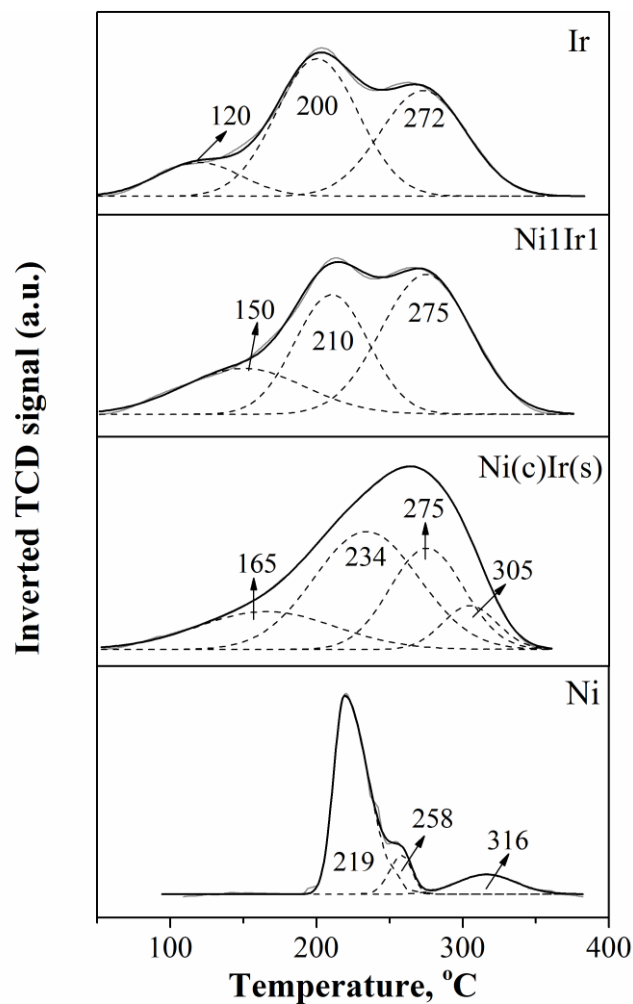
Figure 4.3. H$_2$-TPR profiles of the selected γ-Al$_2$O$_3$ supported catalysts. Positive inverted TCD signal indicates hydrogen consumption in H$_2$/Ar mixture.

The TPR of Ni1Ir1 shows three peaks at 150, 210 and 275°C. The first two peaks came at higher temperatures than those of mono Ir, while the second peak at 210°C can be also ascribed to the contribution from the shifted 219°C Ni peak. This result agrees with the TPR studies of Ir-Ni/γ-Al$_2$O$_3$ catalysts, where intimate contact between the oxide species of Ni and Ir delays reduction of Ir and facilitates that of Ni [13]. Such behaviour is a typical indication of alloy formation, which confirms our hypothesis of intrinsic bimetallic nanoparticle formation instead of the physical mixture of mono Ir and mono Ni

nanoparticles [44]. However, the high temperature reduction peak centered at 275°C remains intact, which implies the presence of some segregated mono Ir oxygen-rich complexes as well.

The deconvoluted TPR spectrum of Ni(c)Ir(s) reveals peaks at 165, 234, 275 and 305°C. The first two are at higher temperatures than those of the monoforms and indicate bimetallic formation. The peak at 275°C may indicate either some monometallic Ir particles or the close contact between the Ir atoms in the nanoparticle shell, resembling a monometallic Ir nanoparticle's surface. In addition to the formation of bimetallic species discussed analogously for Ni1Ir1, the peak at 305°C may indicate reduction of core Ni atoms in little or no contact with Ir atoms. Thus, TPR profiles reveal bimetallic interactions in the Ni-Ir samples, mostly indicating their intrinsic bimetallic nature, with the possible co-existence of some monometallic Ir structures. Simultaneous reduction for the alloy structure and hydrogen-sacrificial technique for the core-shell does indeed result in different structures, despite the same molar ratio of Ni and Ir.

Since Ni and Ir have different chemisorption behaviours toward CO_2 [45], carbon dioxide was used as a probe molecule on the catalyst surface. Figure 4.4 shows the CO_2-TPD profiles of selected supported catalysts after subtracting the reference TPD data for γ-Al_2O_3 to eliminate the support effect. A relatively sharp peak is observed for monometallic Ni catalyst at 80°C, which agrees with the literature, relating to the weakly adsorbed CO_2 [46,47]. The Ir catalyst also shows a peak at 90°C but with a more pronounced tail than the Ni catalyst, which continues up to about 300°C. Such tails indicate continuous desorption or dissociation of CO_2 during TPD analysis [46]. The core-shell structure's desorption profile can neither prove nor reject bimetallic interactions in the Ni(c)Ir(s) sample, since it

may be governed by tightly packed Ir atoms in the nanoparticle shell. However, the Ni1Ir1 sample's peak significantly differs from the monoforms', which does indicate bimetallic interactions.
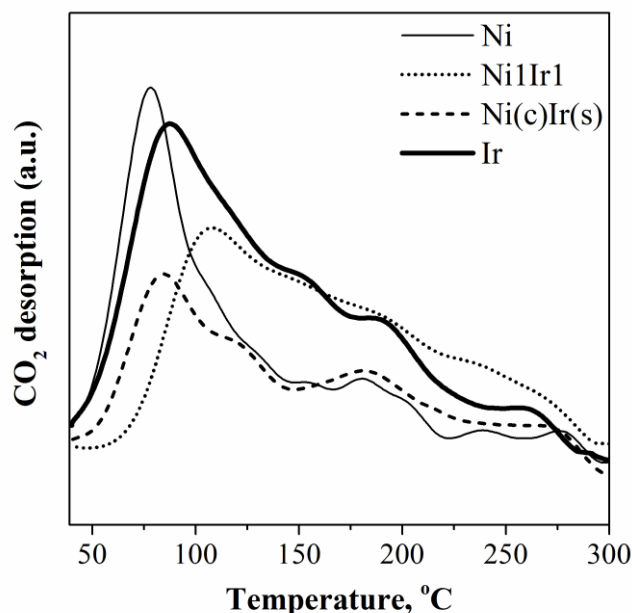
Figure 4.4. CO_2-TPD profiles of selected γ-Al_2O_3 supported catalysts, after subtraction of the TPD data for the support.

Figure 4.5 shows DRIFT spectra of the adsorbed CO for the same catalysts at frequencies from 1800-2150 cm^{-1} along with deconvoluted peaks. Deconvolution for bimetallic samples was performed the same way as for TPR. For monometallic Ir, peaks at 2069, 2008 cm^{-1} and 1865 cm^{-1} were detected, which agrees with results reported for Ir catalysts [48]. The band at 1865 cm^{-1} relates to the bridged type of adsorbed CO [49], while the one at 2008 cm^{-1} relates to linearly bonded CO [50,51]. The band at 2069 cm^{-1} may reflect CO molecules adsorbed linearly on large iridium crystallites [51], or Ir-dicarbonyl species, when one Ir atom can accommodate two CO molecules [50]. Monometallic Ni catalyst shows five peaks from 1824-2108 cm^{-1}. The 1824 cm^{-1} and 1872 cm^{-1} bands may reflect the bridged type of adsorbed CO [49]; the peaks at 1994 cm^{-1} and

2030 cm^{-1} the CO molecules adsorbed linearly on Ni particles [52]. The two peaks for each

adsorption mode may be explained by CO adsorption on metal atoms with different

coordination numbers on a nanoparticle surface (terrace, edge and corner atoms) [49]. The

weak band at 2108 cm^{-1} may reflect CO adsorption on some Ni$^{\delta+}$ species resistant to

reduction [53].
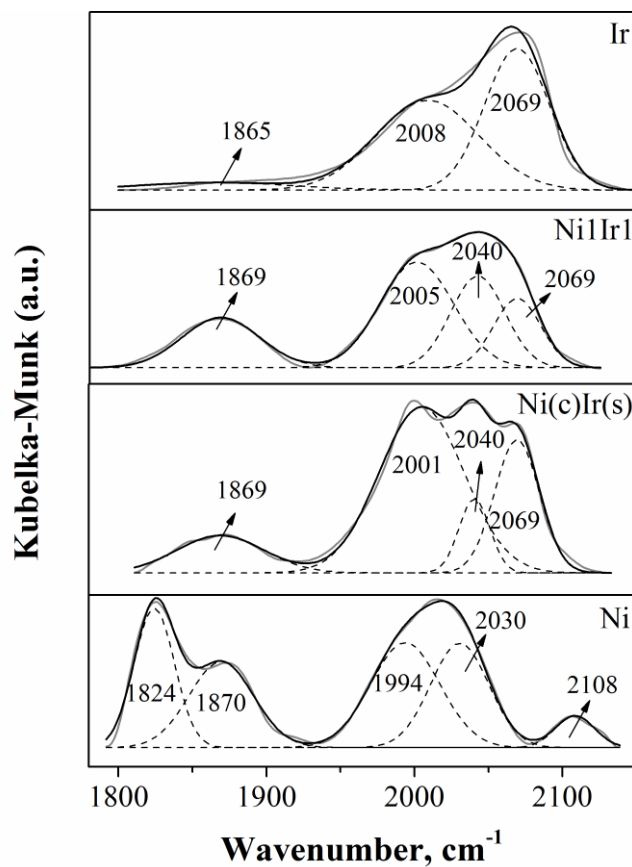
Figure 4.5. DRIFT spectra of the adsorbed CO.

In the DRIFT spectra of the two bimetallic samples, the band at 1869 cm^{-1} in both

Ni1Ir1 and Ni(c)Ir(s) is positioned between those of mono Ir and mono Ni (1865 and 1870

cm^{-1}, respectively), which can be related to the bridged adsorbed CO molecules. However,

neither sample shows any sign of the 1824 cm^{-1} peak of mono Ni, but both present peaks at

positions very close to that of the mono Ir, which indicates Ir on the samples' surfaces. The

bands of 2005 cm^{-1} in Ni1Ir1 and 2001 cm^{-1} in Ni(c)Ir(s) are close to the corresponding peak of the mono Ir (2008 cm^{-1}). The small differences observed can be related to the bimetallic interactions. All three, i.e. Ir, Ni1Ir1 and Ni(c)Ir(s), show a peak at 2069 cm^{-1}. Both bimetallic samples also show a peak at 2040 cm^{-1}, with higher intensity in Ni1Ir1 than in Ni(c)Ir(s). The 10 cm^{-1} difference with monometallic Ni indicates changes in electronic properties of Ni atoms in the bimetallic samples [48,54,55], or new sites created upon alloying [54]. Thus, like the TPR results, the DRIFT spectra confirm bimetallic interactions in Ni-Ir samples, with possible co-existence of monometallic Ir clusters.

Table 4.1 presents the XPS binding energy (BE) values of the Ni 2p$_{3/2}$ and Ir 4f$_{7/2}$ after deconvolution into metallic and oxide components. The BE values of 852.4 and 855.2 eV in Ni/γ-Al$_2$O$_3$ and 60.7 and 62.0 eV in Ir/γ-Al$_2$O$_3$ match reported numbers for metallic and oxide Ni and Ir, respectively [56,57,58]. Bimetallic samples show minor but consistent shifts of BE values from their monometallic counterparts, about 0.2-0.3 eV up from Ni and 0.3 eV down from Ir implying charge transfer from Ni to Ir upon alloying, which can strengthen the growing evidence of bimetallicity and new clusters. A similar transfer of charge from Ni to Pt upon alloying has been reported in the literature [59].

Table 4.1. XPS binding energy values for Ni and Ir (after peak deconvolution into metallic and oxide components).

Catalyst (support: γ-Al$_2$O$_3$)	Binding energy (eV)	
	Ni 2p$_{3/2}$	Ir 4f$_{7/2}$
Ni	852.4 855.2	
Ni2Ir1	852.6 855.6	60.4 61.5
Ni1Ir1	852.7 855.4	60.7 61.8
Ni(c)Ir(s)	852.6 855.4	60.6 61.9
Ir		60.7 62.0

Angle-resolved XPS (normal, 45° and 60° tilt) was also performed on Ni(c)Ir(s). The normal beam provides the information on the top 8-10 nm of the sample, while the tilted ones reduce the depth by cos45^o or cos60^o factor (5.6 - 4 nm). Since some Ni(c)Ir(s) particles are close to the 4-nm range (3.2 ± 0.6 nm), we only expected some degree of Ir/Ni intensity ratio increase upon tilting. Indeed, the ratio increased from 0.9 to 1.4, indicating Ir excess on the catalyst surface.

Alloying two metals may increase their resistance to sintering [41], as we evaluated as further evidence of bimetallicity. All catalysts were calcined at 400°C, after depositing them on γ-Al$_2$O$_3$, to remove PVP. Monometallic Ni and Ir exhibited different resistance. Figure 4.6 show TEM images of fresh and calcined catalysts and Table 4.2 summarize size changes. Monometallic Ni sinters severely after calcination (into agglomerates of about 50 nm), while mono Ir retains its size. Oxidative agglomeration of Ir is known to occur at calcination temperatures above 400°C [41,60]. The samples with the Ir-to-Ni molar ratio of equal or greater than 1, including the core-shell structure, did not sinter. This implies that no monometallic Ni is present in the samples, and supports bimetallicity.

There is no evidence that the synthesized nanoparticles preserved their structure after the high-temperature oxidation and reduction. On the contrary, particles with low Ir content sintered on calcination, and calcination probably enriched the surface of all Ni-containing nanoparticles with Ni. Ni's heat of sublimation (101 kcal/mol) [61] is lower than that of Ir (160 kcal/mol) [62], so Ni's migration to the surface would decrease the nanoparticles' surface energy. Both Ni and Ir have the f.c.c. crystal structure and are completely miscible in each other below 1455°C [63]. In our calcination-reduction temperature range we did not except the bimetallic nanoparticles' transformation to one

most thermodynamically stable structure, which was shown to occur at ~700-800 K for Au-Pt nanoparticles [64]. A study of the Pd-Pt nanoparticles' thermodynamic stability revealed that the transformation process becomes significant at ~1600 K [65]. The melting point of NiO is even higher than that of Ni (1960°C vs. 1455°C, respectively); thus, the O$_2$ atmosphere is not expected to promote the oxidized particles' sintering vs. the reduced Ni.

4.2. Size change and the stabilizer removal from the catalysts after calcination for 2 h at 400°C in Table air.

Catalyst (support: γ-Al$_2$O$_3$)	TEM sizes, nm (colloidal NPs)	TEM size of NPs after calcination (Fig. 6)	Carbon content, wt.% (fresh catalyst)	Carbon rejection after calcination[a], %
Ni	2.7±0.7	Sintered (up to 50 nm)	8.40	97.4
Ni2Ir1	2.5±0.5	Agglomerates (up to 10 nm)	-	-
Ni1Ir1	2.3±0.5	No change	7.01	99.6
Ni1Ir3	2.2±0.4	No change	-	-
Ni(c)Ir(s)	3.2±0.6	No change	3.99	99.7
Ir	2.0±0.2	No change	6.90	99.7

[a] carbon content of pure calcined Al$_2$O$_3$ (0.08 wt.%) was subtracted from the numbers reported

The following catalytic reactions were performed at 350°C after 400°C calcination and 359°C reduction. The Characterization analyses described above were conducted after calcination and reduction at 400°C (higher than the reaction temperature); thus, the results cover the worst-case scenario of bimetallic particle rearrangement due to hot spot formation during the reaction. The surface characteristics described can be assumed to be close to the in-situ surface arrangement of Ni and Ir.
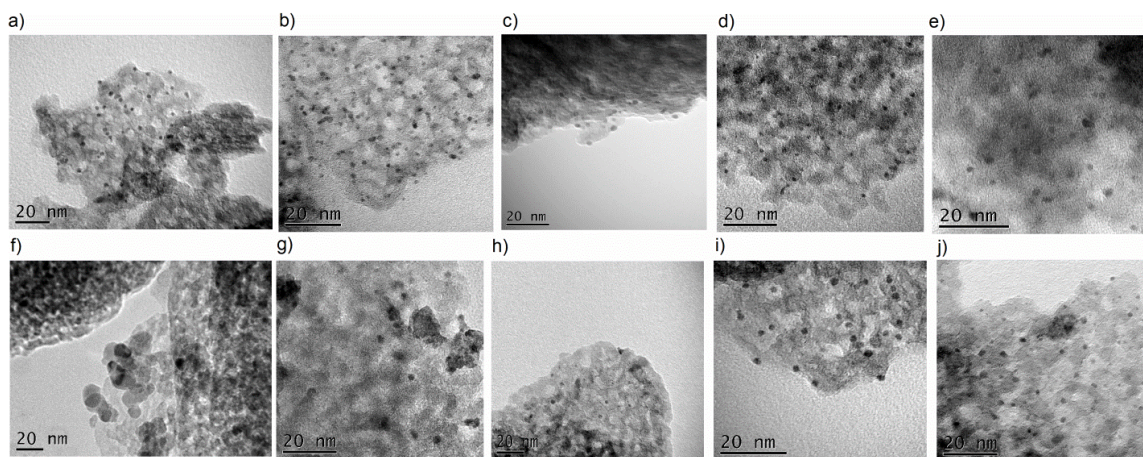
Figure 4.6. TEM images of the fresh (top column) and calcined (2 h, 400°C; bottom column) supported catalysts: (a, f) Ni, (b, g) Ni2Ir1, (c, h) Ni1Ir1, (d, i) Ni(c)Ir(s) and (e, j) Ir.

4.3.2. Stabilizer removal before catalysis

The supported catalysts were calcined at 400°C in air for 2 h before the catalytic reaction to remove PVP. PVP can be adsorbed on the metal surface as a result of hydrophobic interactions [66], thus blocking part of the active surface sites. We did not aim to find the best calcination conditions, but chose a temperature higher than the free PVP decomposition temperature, i.e. about 350°C [67], to ensure PVP's removal from particles capable of carbide formation. Table 4.2 presents the carbon content of the selected fresh and calcined catalysts analyzed by CHN analysis. The calcination treatment led to more than 99.6% removal of carbon in Ir-containing catalysts (97.4% for Ni), and XPS results showed no detectable Cl or N traces in the samples. This confirms that calcination-reduction successfully rejected PVP and chlorine species.

4.3.3. Catalytic activity in indane ring opening

Table 4.3 shows the catalytic activity results of the synthesized catalysts. Since monometallic Ni shows no activity for the RO, the results are reported per mole of Ir, and the amount of Ir was standardised (0.8 mg). The negligible Ni RO activity is in line with data presented in literature: in an extensive study dealing with the RO of several five and six-membered-ring naphthenes [1], the activity of Ir/Al_2O_3 for the RO of methylcyclopentane at $275^{\circ}C$ was found to be 50 times higher than that of the Ni/Al_2O_3.

The addition of Ni to Ir with a molar ratio of equal or less than 1 increases the catalytic activity. Above the specified ratio, the activity drops significantly as for Ni2Ir1. However, the highest Ir-to-Ni ratio of 3 and the absence of Ni do not lead to the highest activity. That was observed for the 1/1 Ni(c)Ir(s) sample, which has almost twice the activity of monometallic Ir, and 50% more than the Ni1Ir1 sample with the same metal ratio but synthesized by simultaneous metal reduction. Thus, the hydrogen-sacrificial technique is paramount for achieving the highest activity. Since the amount of Ir used is the same, and monometallic Ir does not sinter, the observed activities further confirm bimetallicity, although the presence of some monometallic Ir nanoparticles cannot be excluded.

An interesting coincidence was found when calculating the turnover frequency TOF for the monometallic Ir catalyst. Based on the diameter of an Ir nanoparticle (2.0 nm) and assuming an ideal f.c.c. cuboctahedron crystal with a unit cell parameter of 0.384 nm, we found Ir dispersion based on van Hardeveld and Hartog's surface statics as 61% [68], yielding TOF of 0.7 $mol_{indane}/mol_{surface\ Ir}/min$. This value is almost the same as the activity value of 0.8 $mol_{indane}/mol_{\ Ir}/min$ for the Ni(c)Ir(s) catalyst. The similarity indicates that in

the latter catalyst all iridium atoms are accessible to the reactant, meaning they are in the nanoparticle shell, with Ni supporting them. However, synergism cannot be excluded, since some monometallic Ir nanoparticles with lower dispersion may be also present.

Table 4.3. Catalytic activity of the synthesized catalysts in atmospheric ring opening of indane at $336^{\circ}C$ (at 125 min on stream[a]).

Catalyst (support: γ-Al_2O_3)	Ni / Ir loadings, wt.%	Activity, 10^{-1} $mol_{indane}/ mol_{Ir}/ min$	Productivity, 10^{-1} $mol_{(ET+PB)}/mol_{Ir}/min$[b]
Ni	0.165/0	<0.1	<0.1
Ni2Ir1	0.067/0.118	1.3	1.2
Ni1Ir1	0.044/0.163	5.6	4.5
Ni1Ir3	0.022/0.218	5.1	3.9
Ni(c)Ir(s)	0.052/0.165	8.3	6.4
Ir	0/0.220	4.3	3.4

[a] 0.8 mg of Ir used for each activity measurement
[b] ET: 2-ethyltoluene, PB: *n*-propylbenzene

The core-shell sample also allows the highest production rate of single cleavage products (i.e. 2-ethyltoluene and n-propylbenzene). The lower selectivity of this catalyst for 2-ethyltoluene and n-propylbenzene compared to the rest of the samples (see Table 4.4) should not be used for comparison with other catalysts, since it is observed at much higher conversions. Nickel addition does not improve the ratio of n-propylbenzene to 2-ethyltoluene. This is in line with the dicarbene RO mechanism, which results in the cleavage of unsubstituted secondary-secondary carbon atom bonds, i.e., yielding 2-ethyltoluene for this specific reaction, and agrees with the literature, which suggests a dicarbene mechanism domination for both Ni and Ir in RO reactions [15]. The observed

low lights formation agrees with the literature data on Ir-catalyzed ring opening reactions [1,7]. Because of this work, we can replace rare and expensive Ir with Ni and increase the RO activity per total Ir loading in the reactor.

Table 4.4. Selectivities of the synthesized catalysts in atmospheric ring opening of indane at 336°C (at 125 min on stream[a]).

Catalyst (support: γ-Al$_2$O$_3$)	Selectivity, wt.%							
	2-ethyl-toluene	n-propyl-benzene	o-xylene	ethyl-benzene	toluene	benzene	lights
Ni	<1 % conversion							
Ni2Ir1	69	20	3	0	4	2	2
Ni1Ir1	64	17	10	1	4	1	3
Ni1Ir3	66	11	13	2	5	0	3
Ni(c)Ir(s)	51	9	20	3	9	1	7
Ir	64	16	10	1	4	1	4

[a] Note that the selectivities are at different conversions (activities, Table 3)

The results obtained can be compared with reported data on the atmospheric RO of indane at 325°C using a series of in-house Pt-Ir catalysts [7,44,48]. For the most active bimetallic formulation of Pt5Ir95 (based on wt.%)/γ-Al$_2$O$_3$, the product selectivities at 55% indane conversion at 275 min on stream were reported as 67.1, 8.8, 12.9, 3.1, 4.1, 0.4 and 3.6 (wt.%) for 2-ethyltoluene, n-propylbenzene, o-xylene, ethylbenzene, toluene, benzene and lights, respectively [7]. These selectivities match the selectivities of our Ni1Ir3 catalyst (or Ni9Ir91 in wt.%), as demonstrated in Table 4. This finding indicates that Pt can be successfully replaced by Ni without loss in selectivity. In terms of activity, using the

127

reported values for Pt5Ir95 catalyst (4.8 dm^3(n)/h H_2 flow, H_2/indane molar ratio of 63, 0.3 g amount of catalyst, 2 wt.% sum of metal loadings [44] and 83% dispersion [48]) the TOF can be calculated as 1.2 mol_{indane}/$mol_{surface\ atoms}$/min. The TOF value for our Ni(c)Ir(s) catalyst at the same 325^oC can be estimated from 0.8 mol_{indane}/$mol_{surface\ atoms}$ /min at 336^oC and the reaction activation energy of 78 kJ/mol (found previously for the monometallic Ir catalyst [69]) as 0.6 mol_{indane}/$mol_{surface\ atoms}$ /min. Considering the fact that the data stem from two different groups, the value may be considered comparable to the value for the Pt5Ir95 catalyst; however, the catalyst reported herein does not contain Pt and has a lower amount of Ir.

The TEM picture of exemplary Ni1Ir1 catalyst before and after the catalytic reaction (200 min) is presented in Figure 4.7 and reveals no observable particle sintering after the reaction.
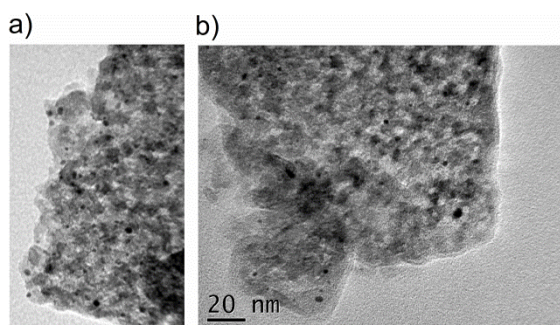
Figure 4.7. TEM images of Ni1Ir1 catalyst: (a) before the catalytic reaction (calcined and reduced in-situ) and (b) after the 200 min on stream.

4.4. Conclusion

The correct method to synthesize bimetallic nanoparticles is essential in developing a material with enhanced catalytic performance. A 1:1 molar ratio of Ni-Ir leads to doubled catalytic activity only if Ir is placed preferably in the nanoparticle shell. This was possible due to applying a hydrogen-sacrificial technique applied to preformed Ni core

nanoparticles, as opposed to the simultaneous reduction of Ni and Ir precursors. TEM, XPS, CO DRIFTS, TPR and CO_2-TPD and CHN analysis were performed on a variety of Ni-Ir nanoparticles synthesized in the presence of PVP and deposited on alumina followed by high-temperature polymer removal. The particles are mostly bimetallic, and the presence of Ir enhanced their stability towards sintering. The Ni(core)-Ir(shell) catalyst showed twice higher activity in indane ring opening at 350^oC than that of monometallic Ir, and allowed higher yield of single cleavage products. Ni presence did not change the dicarbene path for RO characteristic of Ir. The study has developed a material that will spare rare and expensive iridium and enhance its performance. Supposedly, the introduction of acidic function into the support may further improve ring opening yield via the 6-member ring isomerisation to a 5-member ring.

4.5. References

[1] G. B. McVicker, M. Daage, M. S. Touvelle, C. W. Hudson, D. P. Klein, W. C. Baird Jr., B. R. Cook, J. G. Chen, S. Hantzer, D. E. W. Vaughan, E. S. Ellis, O. C. Feeley, J. Catal. 210 (2002) 137-148.

[2] R.C. Santana, P.T. Do, M. Santikunaporn, W.E. Alvarez, J.D. Taylor, E.L. Sughrue, D.E. Resasco, Fuel 85 (2006) 643-656.

[3] W.E. Alvarez, D.E. Resasco, J. Catal. 164 (1996) 467-476.

[4] D. Teschner, K. Matusek, Z. Paal, J. Catal. 192 (2000) 335-343.

[5] D. Kubicka, M. Kangas, N. Kumar, M. Tiitta, M. Lindblad, D.Yu. Murzin, Top. Catal. 53 (2010) 1438-1445.

[6] A. Djeddi, I. Fechete, F. Garin, Appl. Catal. A 413-414 (2012) 340-349.

[7] U. Nylen, L. Sassu, S. Melis, S. Jaras, M. Boutonnet, Appl. Catal. A 299 (2006) 1-13.

[8] H.Du, C. Fairbridge, H. Yang, Z. Ring, Appl. Catal. A 294 (2005) 1-21.

[9] H. Shi, O. Y. Gutierrez, G. L. Haller, D. Mei, R. Rousseau, J. A. Lercher, J. Catal. 297 (2013) 70–78.

[10] A. Djeddi, I. Fechete, F. Garin, Catal. Commun. 17 (2012) 173–178.

[11] R. Moraes, K. Thomas, S. Thomas, S.V. Donk, G. Grasso, J.-P. Gilson, M. Houalla, J. Catal. 286 (2012) 62-77.

[12] J.-W. Park, K. Thomas, J.V. Gestel, J.-P. Gilson, C. Collet, J.-P. Dath, M. Houalla, Appl. Catal. A 388 (2010) 37-44.

[13] S. Dokjampa, T. Rirksomboon, D.T.M. Phuong, D. E. Resasco, J. Mol. Catal. A: Chem. 274 (2007) 231-240.

[14] N. Semagina, X. Yin, J. Shen, K. Loganathan, US Patent, 2013, No. US-2013-0248414-A1.

[15] P.T. Do, W.E. Alvarez, D.E. Resasco, J. Catal. 238 (2006) 477-488.

[16] C.G. Walter, B. Coq, F. Figueras, M. Boulet, Appl. Catal. A 133 (1995) 95-102.

[17] J.G. van Senden, E.H. van Broekhoven, C.T.J. Wreesman, V. Ponec, J. Catal. 87 (1984) 468-477.

[18] F. Luck, J.L. Schmitt, G. Maire, React. Kinet. Catal. Lett. 21 (1982) 219-224.

[19] B. Coq, F. Figueras, J. Mol. Catal. A: Chem. 173 (2001) 117-134.

[20] Y. Wang, N. Toshima, J. Phys. Chem. B 101 (1997) 5301-5306.

[21] N. Toshima, H. Yan, Y. Shiraishi in: *Metal Nanoclusters in Catalysis and Material Science: The Issue of Size Control* (Eds.: G. Schmid, N. Toshima, B. Corain), Elsevier Science, Amesterdam (2008) 49-75.

[22] G. Schmid, H. West, J. O. Halm, J. O. Bovin, C. Grenthe, Chem.-Eur. J. 2 (1996) 1099-1103.

[23] Y. Mizukoshi, T. Fujimoto, Y. Nagata, R. Oshima, Y. Maeda, J. Phys. Chem. B 104 (2000) 6028-6032.

[24] N. Toshima, Y. Shiraishi, A. Shiotsuki, D. Ikenaga, Y. Wang, Eur. Phys. J. D 16 (2001) 209-212.

[25] A.U. Nilekar, S. Alayoglu, B. Eichhorn, M. Mavrikakis, J. Am. Chem. Soc. 132 (2010) 7418-7428.

[26] N. Toshima, Pure Appl. Chem. 72 (2000) 317-325.

[27] N. Toshima, K. Hirakawa, Polym. J. 31 (1999) 1127-1132.

[28] S.J. Cho, S.K. Kang, Catal. Today 93 (2004) 561-566.

[29] L. DSouza, S. Sampath, Langmuir 16 (2000) 8510-8517.

[30] H. Ziaei-azad, C.-X. Yin, J. Shen, Y. Hu, D. Karpuzov, N. Semagina, J. Catal. 300 (2013) 113-124.

[31] W.-R. Lee, M. G. Kim, J.-R. Choi, J.-I. Park, S. J. Ko, S. J. Oh, J. Cheon, J. Am. Chem. Soc 127 (2005) 16090-16097.

[32] S. Bhlapibul, K. Pruksathorn, P. Piumsomboon, Renewable Energy 41 (2012) 262-266.

[33] Y. Zhao, X. Yang, J. Tian, F. Wang, L. Zhan, Int. J. Hydrogen Energy 35 (2010) 3249-3257.

[34] K. Nagaveni, A. Gayen, G. N. Subbanna, M. S. Hegde, J. Mater. Chem. 12 (2002) 3147-3151.

[35] C.-H. Jun, Y. J. Park, Y.-R. Yeon, J.-R. Choi, W.-R. Lee, S.-J. Ko, J. Cheon, Chem. Commun. 15 (2006) 1619-1621.

[36] L. D. Pachon, M. B. Thathagar, F. Hartl, G. Rothenberg, Phys. Chem. Chem. Phys. 8 (2006) 151-157.

[37] Z.D. Wei, Y.C. Feng, L. Li, M.J. Liao, Y. Fu, C.X. Sun, Z.G. Shao, P.K. Shen, J. Power Sources 180 (2008) 84-91.

[38] S.K. Singh, Q. Xu, Chem. Commun. 46 (2010) 6545-6547.

[39] S. Link, M.A. El-Sayed, J. Phys. Chem. B 103 (1999) 8410-8426.

[40] J. Lapujoulade, K. S. Neil, Surf. Sci. 35 (1973) 288-301.

[41] Y.-J. Huang, S. C. Fung, W. E. Gates, G. B. Mcvicker, J. Catal. 118 (1989) 192-202.

[42] S. Subramanian, J.A. Schwarz, Appl. Catal. 74 (1991) 65-81.

[43] J. Zielinski, J. Mol. Catal. 83 (1993) 197-206.

[44] U. Nylen, J.F. Delgado,S. Jaras, M. Boutonnet, Appl. Catal. A 26 (2004) 189-200.

[45] J. Hagen, *Industrial Catalysis: A practical approach*, Wiley-VCH Weinheim, (2006).

[46] H.-S. Roh, K.-W. Jun, W.-S. Dong, J.-S. Chang, S.-E. Park, Y.-I. Joe, J. Mol. Catal. A: Chem. 181 (2002) 137-142.

[47] M. Cai, J. Wen, W. Chu, X. Cheng, Z. Li., J. Nat. Gas Chem. 20 (2011) 318-324.

[48] U. Nylen, B. Pawelec, M. Boutonnet, J.L.G. Fierro, Appl. Catal. A 299 (2006) 14-29.

[49] N. Sheppard, C. D. L. Cruz, Catal. Today 70 (2001) 3-13.

[50] G. B. McVicker, R. T. K. Baker, R. L. Garten, E. L. Kugler, J. Catal. 65 (1980) 207-220.

[51] F. Solymosi, J. Rasko, J. Catal. 62 (1980) 253-263.

[52] G. Poncelet, M.A. Centeno, R. Molina, Appl. Catal. A 288 (2005) 232-242.

[53] M. Mihaylov, T. Tsoncheva, K. Hadjiivanov, J. Mater. Sci. 46 (2011) 7144-7151.

[54] P. Samoila, M. Boutzeloit, C. Especel, F. Epron, P. Marecot, J. Catal. 276 (2010) 237-248.

[55] O. Roduner, E. Terekhina, J. Phys. Chem. C 116 (2012) 6973-6979.

[56] J. F. Moulder, W. F. Stickle, P. E. Sobol, K. D. Bomben, *Handbook of X-ray Photoelectron Spectroscopy, Ulvac-Phi, Chigasaki and Physical Electronics*, Minnesota, (1995).

[57] R. Nyholm, A. Berndtsson, N. Martensson, J. Phys. C: Solid State Phys. 13 (1980) L1091-L1096.

[58] M. Wu, D. M. Hercules, J. Phys. Chem. 83 (1979) 2003-2008.

[59] B. Moraweck, A.J. Renouprez, E.K. Htil, R. Baudoing-Savois, J. Phys. Chem. 97 (1993) 4288-4292.

[60] R. L. Garten, J. H. Sinfelt, J. Catal. 62 (1980) 127-139.

[61] V. I. Severin, A. V. Tseplayaeva, N. E. Khandamirova, Y. A. Priselkov, N. A. Chernova, l. V. Golubtsov, V. B. Lukyanov, Mendeleev Commun. 2 (1992) 97-100.

[62] R. F. Hampson, Jr., R. F. Walker, J. Res. Natl. Bur. Stand., Sect. A. 65A (1961) 289-295.

[63] S.C. Yang, N. Chen, P. Nash, Ir-Ni Phase Diagram, ASM Alloy Phase Diagrams Center, P. Villars, editor-in-chief; H. Okamoto and K. Cenzual, section editors; http://www1.asminternational.org/AsmEnterprise/APD, ASM International, Materials Park, OH, 2006.

[64] H. B. Liu, U. Pal, J. A. Ascencio, J. Phys. Chem. C 112 (2008) 19173–19177.

[65] R. Huang, Y.-H. Wen, Z.-Z. Zhu, S.-G. Sun, J. Phys. Chem. C 116 (2012) 8664−8671.

[66] T. Miyake, M. Teranishi, Chem. Mater. 10 (1998) 594-600.

[67] R.M. Rioux, H. Songa, M. Grass, S. Habas, K. Niesz, J.D. Hoefelmeyer, P. Yang, G.A. Somorjai, Top. Catal. 39 (2006) 167-174.

[68] R.V. Hardeveld, F. Hartog, Surf. Sci. 15 (1969) 189-230.

[69] A. Chhabra, M.Sc. Thesis, University of Alberta, 2012.

[70] G.G. Couto, J.J. Klein, W.H. Schreiner, D.H. Mosca, A.J.A. de Oliveira, A.J.G. Zarbin, J. Colloid Interface Sci. 311 (2007) 461-468.

[71] X. Yan, H. Liu, K.Y. Liew, J. Mater. Chem. 11 (2001) 3387-3391.

Chapter 3: Bimetallic catalysts; requirements for stabilizing PVP removal depend on the surface composition[1]

3.1. Introduction

Increasing attention has been paid to the synthesis of size- and structure-controlled nanoparticles [1]. With sizes typically below 5 nm, these materials are becoming more attractive in heterogeneous catalysis. Such an interest relies on the fact that one can optimize the catalytic activity and selectivity by precise control over the nanoparticle morphology. Unfortunately, the traditional methods of synthesis like impregnation, although still widely used for commercial catalysts, suffer from broad particle size distribution and specifically in bimetallic catalysts, surface inhomogeneity and the intimate contact between two metals are questionable [2].

Colloid chemistry offers relatively easy methods for the controlled synthesis of nanoparticles, which rely on the chemical reduction of a metal salt in the presence of a stabilizing agent to produce zerovalent metal colloids [3]. Alcohols are mostly used for reduction and a stabilizer is necessary to prevent excessive size increase and agglomeration of as-synthesized nanoparticles [3].

Poly(N-vinyl-2-pyrrolidone), or PVP, is a water-soluble amine-based polymer, which is commonly used in the synthesis of metallic nanoparticles [3]. Examples include monometallic particles such as Au [4], Pd [5], Ru [6], Pt [7], Ir [8], as well as various bimetallic combinations including AuAg [9], NiPd [10], PdPt [11], RuIr [12], and PtCu [13]. PVP presence during synthesis and catalysis affects particle size and surface

accessibility of active sites, the two important factors in catalytic studies. A threshold ratio of PVP/metal is necessary for keeping the nanoparticles in solution and above that, a slight size decrease has been typically observed [5, 6, 14]. The effect of the PVP amount in changing particle size is less pronounced as compared to the temperature, type of alcohol, and alcohol concentration. For instance, in the synthesis of Ru nanoparticles, particles with the average diameters of 1.8 to 7.4 nm are reported by changing the reduction temperature in the presence of PVP/RuCl$_3$ molar ratio of 10:1; while changing the PVP/RuCl$_3$ molar ratio from 1 to 50 (at a constant reduction temperature) was shown to change the particle sizes only from 5.7 to 3.8 nm [6].

PVP also can limit surface accessibility of the resulting nanoparticles by interacting with surface sites. Such interactions depend on the type of a metal and the particle sizes. For instance, in PVP-stabilized Pt nanoparticles of < 7 nm, charge transfer occurs from the C=O, C-N and CH$_2$ functional groups of PVP into surface Pt atoms [15]; whereas for Pt particles of > 25 nm, the reverse trend is observed [16]. In the case of Pd nanoparticles, small particles interact only with the oxygen atoms of C=O, while interactions in larger particles include C=O and C-N groups in the PVP pyrrolidone ring [17]. These interactions, although protecting nanoparticles from agglomeration, block part of the surface active sites, thus affecting the properties of the resulting catalysts [18]. Evidence of such effects has been studied for PVP-stabilized Pt nanoparticles by comparing the particle sizes measured by chemisorption (affected by PVP residues) and XRD (not affected by PVP residues) techniques [7]. Consequently, removal of the stabilizer residues is necessary for having an active surface available for catalysis.

Part of the excess PVP used in the synthesis is removed during solvent washing after the deposition of particles on a catalyst support; however, major residues remain and require further treatment. A number of techniques including chemical treatment [19, 20], thermal treatment [21, 22], UV-ozone [23] and plasma treatment [24, 25] have been studied. Of these, thermal treatment is the most commonly used method [21, 22]. Oxidative decomposition of free PVP starts at about 330°C, while the presence of Pt was shown to catalyze the process by oxygen diffusion through the randomly tangled alkyl chains of PVP and dissociation on clean Pt surface sites, which initiates the decomposition process at about 200°C [21]. The decomposition starts at about 100-120°C higher when the treatment is performed under N_2 instead of O_2 [21, 26]. Thus, depending on the nature of the metal and the atmosphere in which the treatment is performed, thermal removal of PVP demands moderate to high temperatures. Such conditions may result in possible metal nanoparticle structural changes as well: metal oxides often have lower melting points than the corresponding reduced metals, thus, nanoparticle sintering and structural changes in oxygen atmosphere may occur at lower temperatures. As a result, thermal removal of PVP can be a challenging trade-off between the elimination of the stabilizer and the structural changes happening to the final catalysts.

Recently, we reported a study showing that it is not always necessary to remove PVP completely before catalysis using two exemplary monometallic Ir and Ru nanoparticles in the ring opening (RO) of indane at 350°C. The RO activities of the PVP-derived Ru catalysts precalcined at 200 and 250°C and hydrogen-treated at 375°C before catalysis, were similar, while the former catalyst had an order-of-magnitude higher amount of PVP residuals as was shown by CHN analysis [27]. Thus, it was possible to achieve

high catalytic reaction rates without complete stabilizer removal; the mild pretreatment ensured thermal stability of the monometallic Ru nanoparticles.

To the best of our knowledge, the reported studies of thermal PVP removal dealt only with monometallic nanoparticles. In the current work, we study the effects brought by thermal PVP removal on bimetallic nanoparticles. As a model bimetallic combination, Pd-Ir catalysts were selected due to the known roles of both metals in the indane RO reaction [28]: Pd does not show any activity and only serves as a dispersing agent for Ir atoms with high RO activity and selectivity if ensembles of at least two contiguous Ir atoms are present on the nanoparticle surface and realize a dicarbene RO mechanism yielding 2-ethyltoluene. The particular question that motivated us for the current work is: if Pd is an inert material in a ring opening, even with the combination with Ir, and the performance of monometallic Ir is not affected by the PVP residuals, could the latter independence be extrapolated to the bimetallic Pd-Ir catalysts stabilized by PVP? In general, how does stabilizer removal affect catalytic properties of bimetallic nanoparticles, and does it depend on the nanoparticle composition and structure?

3.2. Experimental

3.2.1. Materials

The metal nanoparticle precursors were $H_2IrCl_6 \cdot xH_2O$ and H_2PdCl_4. PVP from Sigma-Aldrich with an average molecular weight of 40,000 was used. γ-Al_2O_3 with average pore size 58 Å, SSA 155 m^2/g was received from Sigma-Aldrich). Ethanol and acetone purity were 95 vol.% and >99.7%, respectively. Gases of ultra-high purity

(99.999%) were purchased from Praxair. Milli-Q water was used. Indane, 95% vol., Sigma-Aldrich, was distilled once.

3.2.2. Catalyst preparation

Mono- and bimetallic Pd and Ir nanoparticles were prepared via the alcohol reduction method as explained in our previous work [28]. 0.1 mmol of either Pd or Ir metal precursor was added to a 500-ml three-neck flask and dissolved in 120 ml of Milli-Q water. Random alloy Pd-Ir catalysts were synthesized by coreduction. Three different alloys with the desired molar ratios of Pd:Ir = 3:1, Pd:Ir = 1:1 and Pd:Ir = 1:3 were synthesized using the PVP/metals ratio of 5:1 (molar basis). PVP was added at the PVP/metal(s) ratio of 5:1 (molar basis), followed by 50 ml of ethanol, which serves as solvent and reducing agent. The resulting mixtures were stirred and heated until they boiled, then refluxed in air under vigorous stirring for about 3 h, yielding a dark stable colloidal dispersions of nanoparticles. The actual molar ratios of Pd:Ir in the bimetallic alloys, according to neutron activation analysis (NAA) of the supported catalysts, are 3.6:1, 1.25:1, and 0.5:1, respectively. Thus, hereafter they are referred as Pd4Ir1, Pd1Ir1 and Pd1Ir2. In addition to the Pd1Ir2 bimetallic alloy synthesized with PVP/metal ratio of 5:1, two more samples of the same composition were prepared with the PVP/metal ratios of 10:1 and 40:1 (molar basis) and used for comparative studies.

Pd(core)-Ir(shell) nanoparticles were prepared via hydrogen sacrificial reduction as described previously [28] using PVP/metals ratio of 5:1 (molar basis). Colloidal dispersion of Pd nanoparticles was purged with H_2, followed by Ir precursor addition. The Ir atoms replace the hydride species on Pd surface, creating an iridium shell. The desired Pd:Ir

molar ratio was 1:2, but the NAA of the final supported catalysts showed a ratio of 0.7:1, so the sample from now on will be referred to as Pd(c)Ir(s) [1/1].

The synthesized nanoparticles were deposited on γ-Al_2O_3 using an acetone precipitation [6]. The catalysts were dried at ambient overnight and then were calcined either 1 h at 200°C or 2 h at 400°C under air.

3.2.3. Catalyst characterization

NAA, transmission electron microscopy (TEM), CNH analyses, and diffuse reflectance infrared Fourier transform spectroscopy (DRIFTS) of the adsorbed carbon monoxide (CO) were performed as described previously [29][1].

CO pulse chemisorption of the supported catalysts was studied with an AutoChem 2950 HP device (Micromeritics). The calcined catalysts were reduced by a mixture of 10% H_2 in Ar up to 400°C for 1 h, followed by cooling the sample under He to 40°C. A 3% CO in He mixture was used for analysis. Calculation of the CO uptake amounts and the average diameter of the particles was performed by the instrument software using the CO/Pd and CO/Ir ratios of 0.6 [30] and 1.19 [31], respectively.

CO temperature-programmed desorption (CO-TPD) was performed with the same AutoChem 2950 HP device. About 500 mg of the catalysts calcined for 2 h at 400°C were initially reduced by a mixture of 10% H_2 in Ar up to 400°C for 1 h, followed by cooling the sample under He to 40°C. A mixture of 3% CO in He was passed through the sample at 40°C for about 45 min with a flow of 50 ml/min. Physically adsorbed CO was removed by flushing 50 ml/min of He at 40°C for 1 h. The TPD spectra were collected by flowing 10 ml/min He at temperature ramp from 40°C to 400°C.

---

[1] The NAA analysis was performed by Dr. John Duke at University of Alberta, SLOWPOKE facility.

Temperature programmed desorption of the indane (indane-TPD), the model compound of activity studies, was carried out on selected calcined catalysts. About 100 mg of a sample was reduced by 80 ml/min of hydrogen from ambient temperature up to 400$^{\mathrm{o}}$C for 1 h and cooled to ambient in argon. Indane was introduced to the samples by bubbling argon through an indane-containing bubbler kept at a constant temperature of 10$^{\mathrm{o}}$C for about 45 min. The indane adsorbed sample was flushed with Ar for 30 min to desorb the physically adsorbed molecules, followed by collecting the TPD spectra with AutoChem 2950 under 10 ml/min of He flow from room temperature to 400$^{\mathrm{o}}$C.

3.2.4. Catalytic behaviour in ring opening of indane

Catalytic studies were performed at atmospheric pressure in a packed-bed reactor in the absence of external and internal diffusion limitations as described previously [28]. Catalyst amounts corresponding to 0.8 mg Ir were used for each run except for monometallic Pd, where 0.8 mg Pd were used. Catalysts were pre-treated in situ in H2 at 359$^{\mathrm{o}}$C for 1 h. The reactions were carried out at the reactor with an internal temperature of 336$^{\mathrm{o}}$C. The indane and hydrogen flow rates were 2.8×10^{-5} g/min and 120 ml/min, respectively. The reaction products were analyzed via on-line GC [28][1]. Each catalyst was tested for 200 min on stream and 6 data points were collected at 75, 100, 125, 150, 175 and 200 min. Results were repeatable within a 2-5% experimental error. Selectivities are reported on a mass basis. Response factors were found using reference gas mixtures.

3.3. Results and discussion

3.3.1. PVP effect on the size of as-synthesized nanoparticles

---

[1] The carbon balance error never exceeded 10% and was typically within 3%.

Fig. 3.1 presents the exemplary TEM images and the corresponding size distribution histograms of Pd and Pd(c)Ir(s) [1/1] nanoparticles prepared with the PVP/metal(s) molar ratio of 5:1; sizes for the rest of the samples are listed in Table 3.1[1]. The synthesized nanoparticles were all nearly spherical and exhibited a relatively narrow size distribution. The low molar ratio of PVP/metal(s) used for the synthesis, i.e., 5:1, neither affected the monodispersity of the resulting nanoparticles nor resulted in forming precipitates; although these have been reported at PVP/metal ratios of 0.1 or 1 [6, 14]. Ir particles show a smaller size than their Pd counterparts, while the largest average particle size of 3.1 nm is observed for Pd(c)Ir(s) [1/1], where the Pd core metals are covered by a layer of Ir atoms. The Ir atoms deposit preferentially on the Pd core shell, since iridium is reduced by Pd hydride from the pre-formed Pd nanoparticles. More details about this structure have been disclosed recently [28].
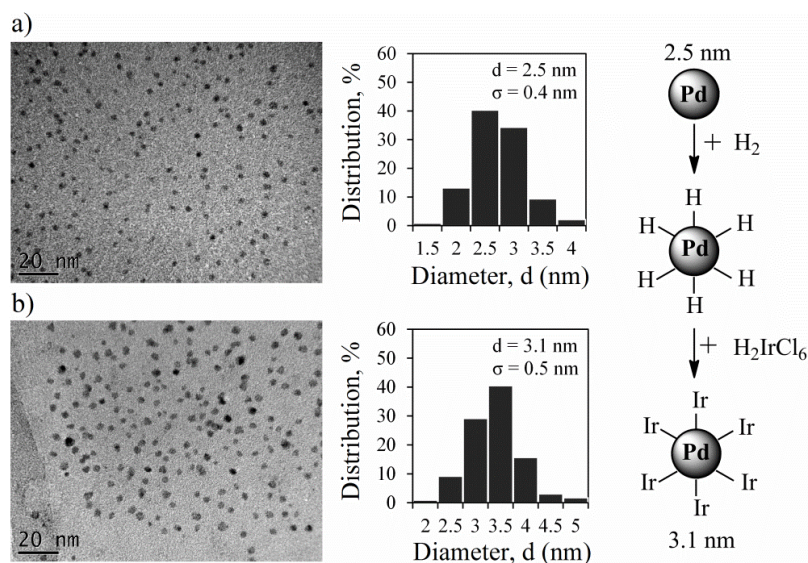
Fig. 3.1. TEM images and size distribution histograms of as-synthesized nanoparticles and their formation schematic: (a) Pd and (b) Pd(c)Ir(s) [1/1] (PVP/metal(s) molarratio = 5:1).

---

[1] The σ in TEM images or the ± sign appearing with TEM sizes refer to one standard deviation in average sizes that are reported.

The effect of PVP on altering the size of nanoparticles was investigated on a selected sample Pd1Ir2 using three PVP/metal ratios of 5:1, 10:1 and 40:1. The average sizes as found by TEM are 1.8 ± 0.6 nm, 1.8 ± 0.7 nm and 2.3 ± 0.8 nm, respectively. Almost negligible (by ~ 0.5 nm) size change is observed with changing the PVP/metal(s) ratio 8-fold. The extra amount of PVP prevents excessive growth of nanoparticles, but at the same time, the ratio increase is known to slow down the reduction process [6]. Temperature, reduction rate, and the concentration of alcohol are reported to influence the size of nanoparticles more significantly as compared to the amount of PVP [5, 6, 14].

Table 3.1. Nanoparticle size and CO uptakes for the nanoparticles (NP) prepared with the PVP/metal(s)   molar ratio of 5:1.

Catalyst (support: γ-Al_2O_3)	TEM sizes, nm (colloidal NPs)	CO uptake, $mol_{CO} / mol_{(Pd+Ir)}$, after calcination[a] at		Average particle size[b], nm
		200°C	400°C	
Samples with excess Ir				
Ir	1.5 ± 0.2	0.08	0.58	2.3
Pd1Ir2	1.8 ± 0.6	0.04	0.62	1.6
Pd(c)Ir(s) [1/1]	3.1 ± 0.5	0.05	0.63	1.5
Samples with excess Pd				
Pd	2.5 ± 0.4	0.01	0.09	7.7
Pd1Ir1	2.5 ± 0.6	0.03	0.51	1.7
Pd4Ir1	2.6 ± 0.6	0.02	0.31	2.4

[a] the catalysts were reduced in hydrogen at 400°C after the calcinations

[b] as found from CO uptakes for the supported catalysts after 400°C calcination / reduction

3.3.2. Treated supported catalysts: nanoparticle size and metal surface composition

Synthesized nanoparticles supported on γ-Al$_2$O$_3$ were calcined at two different temperatures of 200 and 400°C to study the possible effects of thermal treatments on physicochemical properties of the synthesized catalysts. Starting with low temperature treatment of 1 h at 200°C under air, we have recently shown than the supported catalysts retain their structure (i.e., alloy or core-shell) [28]. Briefly, XPS and Pd L$_3$-edge XANES analyses performed on a Pd(c)Ir(s) [1/1] sample calcined for 1 h at 200°C indicated the higher Pd-Pd and Ir-Ir interactions together with the presence of more metallic state Pd in this sample compared to a catalyst with the alloy-type structure, i.e., Pd1Ir1. Also, ion scattering spectroscopy (ISS) revealed that the top layer of the Pd(c)Ir(s) particles is mainly Ir, while an even presence of surface Pd and Ir was observed in the case of Pd1Ir1 [28]. Fig. 3.2 presents the exemplary TEM images of γ-Al$_2$O$_3$ supported Ir and Pd(c)Ir(s) catalysts (PVP/metal(s) ratio = 5:1) after 1 h of calcination at 200°C under air. No sign of sintering or size increase is discernible in either of the catalysts.
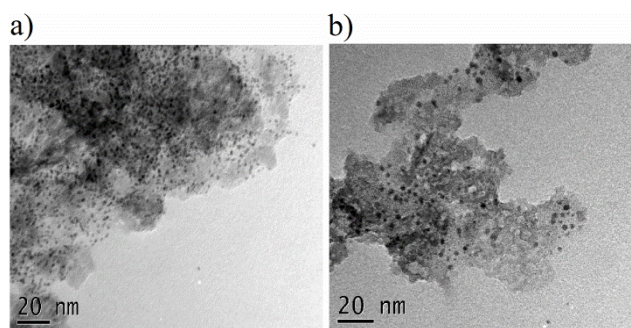
Fig. 3.2. TEM images of selected γ-Al$_2$O$_3$ supported catalysts after calcination at 200°C for 1 h: (a) Ir and (b) Pd(c)Ir(s) [1/1] (PVP/metal(s) molar ratio of 5:1).

TEM images of the catalysts prepared with the PVP/metal(s) ratio of 5:1 after 400°C calcination revealed sintering of the Pd catalysts, resulting in particles as large as 10 nm. The bimetallic sample with a relatively high Pd content, Pd4Ir1, also showed

agglomeration with the particles about 6 nm. A size increase of about 1 nm is discernible for monometallic Ir, but its initial particle diameter (1.8 nm, Table 3.1) was significantly lower than for the Pd-rich samples (2.5 nm, Table 3.1). Other bimetallic catalysts with higher Ir content (Pd1Ir1, Pd1Ir2 and Pd(c)Ir(s) [1/1]) remained intact. Exemplary TEM images of monometallic Pd and Ir, as well as Pd(c)Ir(s) [1/1] catalysts after 400°C calcination are provided in Fig. 3.3. Higher resistance to agglomeration of Ir-rich particles is in line with its higher melting point compared to Pd.
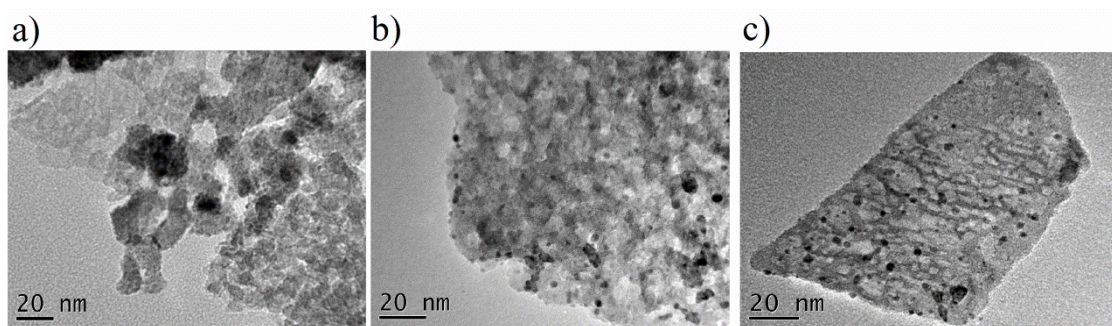
Fig. 3.3. TEM images of selected γ-Al$_2$O$_3$ supported catalysts after calcination at400∘C for 2 h: (a) Pd, (b) Ir and (c) Pd(c)Ir(s) [1/1].

Apart from size changes, an important issue to be considered about the bimetallic catalysts after the high temperature calcination is the surface structural changes, i.e., surface reconstruction. Pd's lower heat of sublimation (89.2 kcal/mol [32]) compared to that of Ir (160 kcal/mol [33]) may cause the migration of some Pd atoms to the surface positions in bimetallic samples after high temperature calcination, making changes in the initial surface arrangements of Pd and Ir atoms. The structural changes discussed here do not imply phase segregation, since both Pd and Ir have the f.c.c. crystal structure and are miscible in each other below 1490°C within the ratios applied here [34]. From the thermodynamic viewpoint, all bimetallic structures of the same composition may come to

the one most favourable atomic arrangement, which destroys the original concept of bimetallic nanoparticle structure control [35, 36]. To investigate possible structural changes in bimetallic catalysts, DRIFT spectroscopy of the adsorbed CO (CO DRIFTS) was performed for the alloy and core-shell samples of the same 1:1 Pd:Ir molar composition Pd1Ir1. The catalysts were calcined in air and reduced in hydrogen at 400°C to approach the catalytic reaction conditions. The results collected in the frequency range of 1800-2200 cm^{-1} are presented in Fig. 3.4 along with the deconvoluted peaks. Three peaks centered at 2069, 2008, and 1865 cm^{-1} were detected for monometallic Ir. The band at 1865 cm^{-1} is related to the bridge-type adsorbed CO [37], while the one at 2008 cm^{-1} is ascribed to the CO bonded linearly [38, 39]. The peak at 2069 cm^{-1} may represent the CO molecules adsorbed linearly on large Ir particles [38] or Ir-dicarbonyl species, where each iridium atom can accommodate two CO molecules [39]. Monometallic Pd shows two peaks, one centered at 1858 cm^{-1}, indicating the bridge-type adsorbed CO [37] and the other one at 1998 cm^{-1}, which is related to the linear adsorption of CO molecules [37]. The DRIFT spectrum of the Pd1Ir1 after calcination at 400°C shows three bands centered at 1864, 2005, 2064 cm^{-1}, characteristic features of Pd and Ir present on the surface. This implies that although Pd migration to the surface cannot be excluded, Ir atoms are still present on the surface after the applied high-temperature treatment for these alloy samples.

The CO-DRIFT spectrum of Pd(c)Ir(s) sample with the same 1:1 molar ratio reveals mostly surface characteristic features of Ir with increased intensity of the peak at 1866 cm^{-1} (bridged CO adsorption). This increase compared to the monometallic Ir could be due to the larger size of the core-shell nanoparticles; so that more bridged CO complexes could be accommodated. The contribution of bridge-type CO adsorption to

exposed Pd atoms cannot be excluded either, but the prevalence of Ir atoms on the surface of Pd(c)Ir(s) comparing the Pd1Ir1 alloy (with the same molar ratio of Pd:Ir) is evident from the large characteristic peak of Ir at 2077 cm^{-1} and the less pronounced bridge-type peak at 1866 cm^{-1} in Pd(c)Ir(s). This implies that although high-temperature treatment could potentially cause Pd migration to the surface, it did not lead to the same spatial atoms' arrangement in the bimetallic nanoparticles.
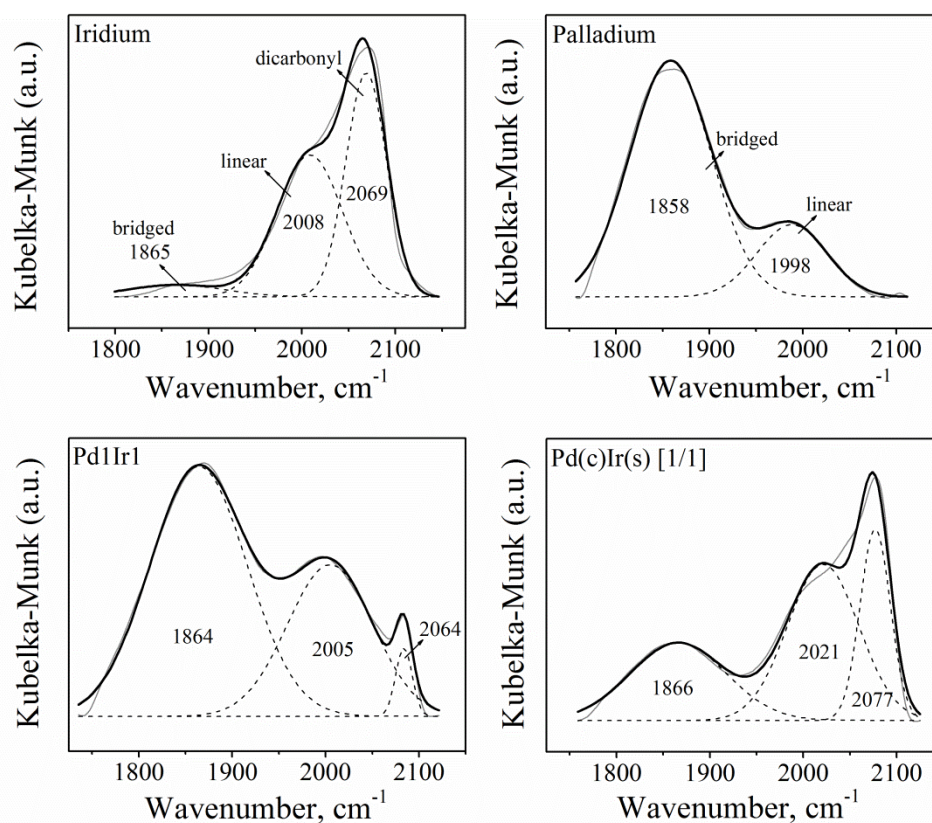
Fig. 3.4. CO-DRIFT spectra for selected samples after calcination and reduction at 400◦C (PVP/metal(s) molar ratio of 5:1 used initially for synthesis).

3.3.3. Treated supported catalysts: PVP residues

The presence of PVP residues on supported catalysts can block active sites and affect the catalytic properties of a sample. CO chemisorption and elemental carbon analysis

were performed on supported catalysts to track the PVP residuals after the thermal treatments. The CO uptake values are presented in Table 3.1. These values after 200^oC calcination and 400^oC reduction in hydrogen indicate that the surface sites are still covered with PVP residuals that block access for adsorption of CO molecules. A similar trend has been reported for Pt nanoparticles supported on mesoporous SBA-15 silica [7]. After calcination at 400^oC and 400^oC reduction in hydrogen, CO uptakes increase dramatically, and the calculated particle sizes (Table 3.1) are in the same range as observed by TEM, indicating that PVP residuals have been removed completely from the surface. Some calculated sizes are smaller than fresh particles from TEM analysis. This could be explained by reported CO/Ir ratios of close to or even higher than two [40], implying multiple bonding of the adsorbed CO on the corner and edge atoms of small particles.

Since the oxidative and oxidative/reduction treatments can have different cleaning effects, which also depend on the metal nature and its loading [18], they were studied separately via CHN analyses of the monometallic Pd and Ir catalysts with the same metal loadings (Table 3.2). Irrespective of the metal nature (Pd or Ir), calcination at 200^oC removed only 30% of C. When the treatment was followed by hydrogen at 375^oC, 77% C removal was achieved for Ir and only 44% for Pd, which and shows metal-nature dependency of the hydrogen treatment. The 400^oC calcination in air only was enough to remove the PVP from both catalysts. For the 200^oC calcination / 375^oC reduction, the carbon analyses data are in line with higher CO uptake by Ir than by Pd due to higher C content on Pd catalysts. However, the 77% carbon removal from Ir catalyst was still not enough to provide efficient CO adsorption: the CO uptake after 400^oC / 375^oC reduction is

7-fold higher (Table 3.1). Thus, complete PVP removal is essential for CO adsorption as we also showed recently for the Ru catalysts [27].

Table 3.2. Carbon analysis performed on supported monometallic Pd and Ir catalysts with 0.23 wt.% metal loading after various treatments[a].

Catalyst (support: γ-Al$_2$O$_3$)	Carbon content, mg C / g$_{cat}$		Carbon removal, %[b]	
	mono Ir	mono Pd	mono Ir	mono Pd
Fresh catalyst	6.4	10.1	-	-
1 h 200°C air	4.4	7.4	31	27
1 h 200°C air + 1 h 375°C H$_2$	1.5	5.7	77	44
1 h 200°C air + 1 h 375°C H$_2$ + 125 min RO reaction	1.2	6.2	81	39
2 h 400°C air	<0.1	<0.1	> 98	> 98
2 h 400°C air + 1 h 375°C H$_2$	<0.1	<0.1	> 98	> 98

[a] Pure Al$_2$O$_3$ without any treatment showed <0.1 mg C / g
[b] Carbon removal values calculated with respect to the fresh catalyst

The carbon analysis was also performed on supported Pd1Ir2 catalysts synthesized with PVP/metal(s) ratios of 5:1 and 40:1; the results are provided in Table 3.3. The amount of carbon (originating from PVP residuals) in Pd1Ir2 (PVP/metal(s) ratio = 5:1) reduces from 7.3 to 5.6 mg C / g$_{cat}$ after 200°C calcination corresponding to 23% carbon removal, while after 400°C calcination the carbon residual trims down to 0.4 mg C / g$_{cat}$, indicating 95% removal of PVP as compared to the fresh catalyst. Applying the same analysis to Pd1Ir2 (PVP/metal(s) ratio = 40:1), the initial carbon content is decreased from 37.9 to 36.0 mg C / g$_{cat}$ after 200°C (carbon removal of 5%), and the carbon residual on this sample goes down to 0.4 mg C / g$_{cat}$ after treatment at 400°C. Thus, carbon analysis reveals that: i) the surface of the supported catalysts is still partially blocked by PVP residues after treating of 1 h at 200°C, that can interfere with CO uptakes and catalytic studies vide infra,

and ii) the high temperature treatment of 400^oC successfully removes the PVP residuals from supported catalysts regardless of the PVP/metal(s) ratio initially used for synthesis.

Table 3.3. The effect of PVP amount and 200^oC and 400^oC calcination pretreatments[a] on properties and catalytic activity of Pd1Ir2/γ-Al$_2$O$_3$ catalysts in ring opening of indane at 336^oC.

PVP/ (Pd+Ir) molar ratio	Pd / Ir loadings, wt.%	TEM sizes[b], nm	Carbon amount, mg C / g_{cat}			CO uptake, mol/mol$_{(Pd+Ir)}$		Activity, 10^{-1} mol$_{indane}$ / mol$_{Ir}$ /min[c]	
			fresh	200^oC	400^oC	200^oC	400^oC	200^oC	400^oC
5	0.05/0.18	1.8 ± 0.6	7.3	5.6	0.4	0.04	0.62	2.0	5.0
10	0.04/0.17	1.8 ± 0.7	-	-	-	0.02	0.67	0.7	4.8
40	0.04/0.14	2.3 ± 0.8	37.9	36.0	0.4	0.01	0.70	0.1	5.2

[a] the catalysts were reduced in hydrogen at $375 - 400^oC$ after the calcinations
[b] from fresh colloidal dispersions before deposition
[c] 0.8 mg Ir used for each activity measurement; data represent 125 min on stream

3.3.4. Catalytic activity in gas-phase indane ring opening

Catalytic activities of the supported catalysts after different calcination at 200^oC and 400^oC and reduction in hydrogen at 375^oC were studied in the atmospheric ring opening of indane at 336^oC; the results are presented in Tables 3.3 and 3.4. Activity and productivity (production rate of single cleavage products 2-ethyltoluene and n-propylbenzene) are reported per mole of Ir, since monometallic Pd shows no activity at the reaction conditions. Also, the amount of Ir was standardized (0.8 mg) except for the case of Pd(c)Ir(s) [1/1], where 0.4 mg Ir was used to avoid the conversion of higher than 95%. It is important to note during the catalytic reaction, no additional carbon removal neither for active Ir or inactive Pd is achieved (Table 3.2).

Table 3.4. Catalytic properties the synthesized catalysts (PVP/metal molar ratio of 5) after 200°C and 400°C calcinations (followed by 375°C reduction) in ring opening of indane at 336°C[a].

Catalyst (support: γ-Al$_2$O$_3$)	Pd / Ir loadings from NAA, wt.%	Activity, 10^{-1} mol$_{indane}$ / mol$_{Ir}$ / min		Productivity, 10^{-1} mol$_{(ET+PB)}$ / mol$_{Ir}$ / min[b]	
		200°C	400°C	200°C	400°C
Samples with excess Ir					
Ir	0/0.22	1.5	1.9	1.3	1.7
Pd1Ir2	0.05/0.18	2.0	5.0	1.8	4.3
Pd(c)Ir(s) [1/1]	0.07/0.19	5.0	6.4	3.9	5.1
Samples with excess Pd					
Pd	0.24/0	0.1	0.1	<0.1	<0.1
Pd1Ir1	0.09/0.13	0.4	4.7	0.4	4.1
Pd4Ir1	0.16/0.08	0.1	1.4	<0.1	1.3

[a] 0.8 mg Ir used for each activity measurement, except for Pd(c)Ir(s) [1/1] where 0.4 mg used; data represent 125 min on stream
[b] ET: 2-ethyltoluene, PB: *n*-propylbenzene

The PVP effect on catalytic behavior of the samples synthesized with different PVP/metal(s) ratio is provided in Table 3.3; the catalysts are compared at similar loadings of 0.20 ± 0.03 wt.%. After calcination at 200°C/reduction at 375°C the activity drops 20-fold with the 8-fold PVP amount increase during synthesis, that stays after the treatment as found by elemental C analysis (Table 3.3). However, after calcination at 400°C/reduction at 375°C, all three samples yield similar activity of (5.0 ± 0.2) × 10^{-1} mol$_{indane}$ / mol$_{Ir}$ / min, confirming that the PVP effects disappear after high temperature treatment irrespective of the initial PVP amount.

In Table 3.4, the catalytic activities are grouped for the Ir- and Pd-rich catalysts. The reason is that for the Pd-rich samples, the effect of surface cleaning on the activity increase is more pronounced than for Ir-rich samples. For bimetallic Pd-rich samples,

increased activity happens to the same extent as the increase of CO uptake upon calcination (Table 3.1). The activity increase is also consistent with the carbon removal analysis showing that the PVP residuals block the reaction active sites.

However, for Ir-rich samples, although an order of magnitude increase in the CO uptake was observed comparing the 200°C and 400°C-calcined catalysts both reduced at 375°C (Table 3.1), an insignificant increase in the ring opening activity was found for the samples with a predominantly Ir shell (monometallic Ir and Pd(core)-Ir(shell) catalysts), and only a 3-fold increase for the alloy Pd1Ir2 sample. The Pd(c)Ir(s) samples calcined also at 300°C, 350°C and 450°C (all reduced at 375°C), show a similar trend (Fig. 3.5): CO uptakes increase up to 400°C with an insignificant increase of the ring opening activity, followed by the uptake and activity decrease at 450°C due to the size increase as a result of sintering and the oxidative agglomeration of Ir shell atoms occurring above 420°C [41]. As seen from carbon analysis (Table 3.2), the Ir surface still contains significant amounts of PVP after the 200°C calcination / 375°C reduction, which explain the lower CO chemisorption for the former catalyst, but these residuals do not reduce the ring opening activity.

These findings indicate that Ir and Pd display different poisoning tolerance to PVP residuals for the ring opening reaction, although for CO chemisorption, their adsorption sites are blocked. It is paramount to clean the nanoparticle surface from the PVP residuals for Pd-rich, but not for the Ir-rich surfaces. This hypothesis may explain calcination effects on an Ir-rich Pd1Ir2 sample and Pd-rich Pd1Ir1 samples: after 400°C calcination, both catalysts show similar activity calculated per amount of Ir, but after 200°C calcination,

only the Ir-rich sample shows the same order of activity, while the Pd-rich catalyst's activity is negligible.
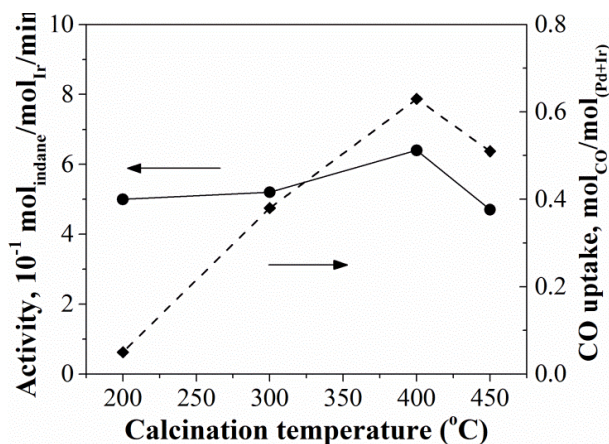
Fig. 3.5. Ring opening catalytic activity and CO uptake of supported Pd(c)Ir(s) [1/1](PVP/metal(s) molar ratio = 5:1) after various thermal treatments.

3.3.5. Indane and CO adsorption

As Ir-rich catalysts were found highly active in the ring opening reaction, a series of indane- and CO-TPD with various heating rates were performed on monometallic Ir catalyst after 400°C calcination and reduction to quantify different adsorption behavior of the two molecules; the corresponding profiles are provided in Fig. 3.6. Activation energy of desorption, Ed, was calculated using the Amenomiya and Cvetanovic equation [42]:

$$Log\left(\frac{T_P{}^2}{\beta}\right) = \frac{E_d}{2.303RT_p} + \log(\frac{E_d A_0}{RC}) \qquad (1)$$

where T_P is the peak temperature (K), β is the heating rate (K/min), E_d is the activation energy of desorption (kJ/mol), R is the gas constant, A_0 is the quantity adsorbed and C is a constant. Plotting $Log\ (T_P{}^2/\beta)$ versus $1/T_P$ results in a line with the slope of E_d. Applying the above equation into the experimental data of Figs. 3.6a and 3.6b results in the

E_d value of 32 kJ/mol for indane; while the E_d values for CO are found as 42 and 58 kJ/mol, respectively. These numbers indicate the stronger adsorption of CO molecules compared to indane. The presence of multiple peaks in desorption profiles of CO implies the presence of multiple adsorption modes, which is in agreement with the CO DRIFT spectra (Fig. 3.4) showing different types of CO bonding with surface metallic sites. However, other reasons such as lateral interactions between adsorbate molecules and/or the penetration of the adsorbing molecules to the subsurface region of a catalyst can also cause a second peak appearing in the TPD profile [43].

As was shown for the Pd1Ir1 catalyst with so-called Pd excess (CO-DRIFTS, Fig. 3.4), this sample's nanoparticle surface is influenced significantly by Pd presence, making this catalyst similar in behavior to the Pd sample in terms of the PVP removal effect. For samples with surfaces rich in Pd (Table 3.4), PVP must be removed for efficient catalysis, since none of the Pd-rich samples are active enough after only 200$^{\rm o}$C-calcination/375$^{\rm o}$C-reduction (note that the activities are calculated based on Ir total moles for fair comparison).

Based on TPD results, one may suggest that for stronger adsorption of carbon monoxide, a clean nanoparticle surface may be required and the presence of impurities such as polymer residues can affect its adsorption more significantly, whereas the required weaker adsorption of indane is not affected as significantly by the presence of PVP residuals. We recently reported a similar conclusion for monometallic Ru and Ir catalysts [27], but how does this trend apply to the bimetallic Pd-Ir catalysts with various compositions?
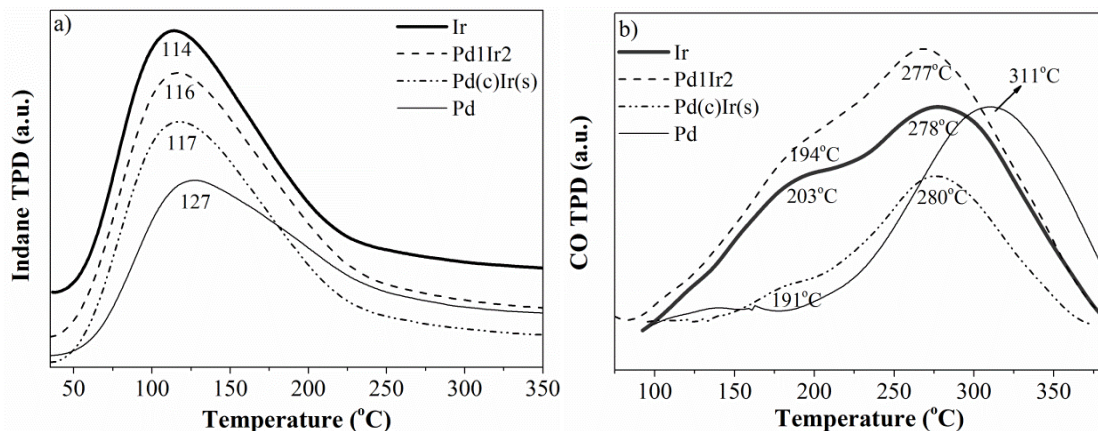
Fig. 3.6. TPD profiles at various heating rates for supported Ir catalysts after calcination and reduction at 400∘C: (a) indane-TPD and (b) CO-TPD.

Other samples from Table 3.4 rich in Ir follow the trend of monometallic iridium: calcination at higher temperatures is not required to boost the activity. Fig. 3.7a and b displays indane- and CO-TPD for the Ir-rich samples after $400^{o}C$ calcination and reduction. Again, the higher desorption temperatures observed in the case of adsorbed CO indicates stronger adsorption of carbon monoxide on the surface of the supported catalysts compared to indane [43]. All bimetallic catalysts show peak positions similar to Ir with some shifts due to bimetallic interactions, and the peaks are far from those for monometallic Pd catalyst. This indicates that the studied samples follow the surface chemistry trend of monometallic Ir and do not require complete removal of PVP for high RO activity.

The $200^{o}C$ calcination/ $400^{o}C$ reduction did not affect the indane chemisorption strength and mode on Pd as compared to the $400^{o}C$ treatments (compare Fig. 3.7b and c), which is anyway not optimal for the indane ring opening due to Pd inactivity. For the Ir catalyst, however, lower desorption temperatures are observed after the $200^{o}C$ treatment. This is in line with the proposed dicarbene ring opening mechanism on Ir when indane is

adsorbed on two contiguous surface atoms perpendicularly [28]. The carbon residuals after the 200°C treatment weaken the interaction, which, however, is still strong enough to cleave the C-C bond, showing similar activities as after the 400°C treatment.
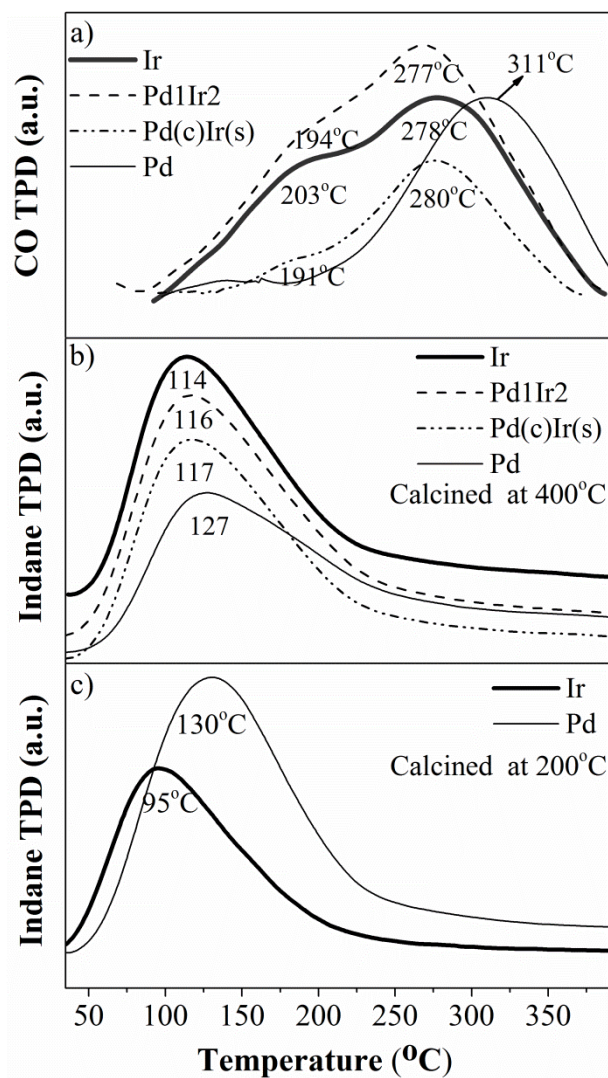
Fig. 3.7. TPD profiles of the selected supported catalysts (PVP/metal(s) molar ratio of 5:1 used initially for synthesis): (a) TPD of adsorbed CO under 10 cc/min He with the heating rate of 12°C/min (the catalysts were calcined / reduced at 400°C); (b) TPD of adsorbed indane under 10 cc/min He with the heating rate of 10°C/min (the catalysts were calcined / reduced at 400°C) and (c) TPD of adsorbed indane under 10 cc/min He with the heating rate of 10°C/min (the catalysts were calcined at 200°C and reduced at 400°C).

The observation that the 200°C and 400°C treatments affect the indane chemisorption differently depending on the metal nature (Pd and Ir, Fig. 3.7b and c) supports our proposed hypothesis that these two metals display different poisoning tolerance to PVP residuals for the ring opening reaction.

Only the bulk metal ratio should not be used to judge the anticipated PVP effect. For example, the 1:1 Pd:Ir bulk molar ratio is kept for Pd(c)Ir(s) and Pd1Ir1 samples. As seen from the CO DRIFTS results (Fig. 3.4), the surface of the former is rich in Ir, while the surface of PdIr1 catalyst includes Pd atoms. This affects the PVP influence: Pd1Ir1 catalyst requires complete cleaning to establish high RO activity (Table 3.4), while the core-shell sample does not.

3.4. Conclusions

Bimetallic Pd-Ir nanoparticles stabilized by PVP and deposited on alumina were studied in indane ring opening reaction after 200°C and 400°C calcination followed by a reduction pretreatment at 375°C. The former treatment did not result in PVP removal, while the 400°C cleaned the surface as shown by CO adsorption and elemental carbon analyses. CO was shown to adsorb more strongly on the catalysts than indane, also its chemisorption was affected more significantly by PVP residuals compared to catalytic activity in ring opening of indane.

Catalysts with surfaces rich in Ir do not require complete polymer removal for high RO activity and their activities after 200°C and 400°C calcination did not vary significantly. Only 400°C calcination could activate the surface of Pd-rich catalysts, which do require complete PVP removal before catalysis. Therefore, complete stabilizer removal

for bimetallic particles is not always necessary and is dependent on the nature of the metals and their surface (not bulk) composition.

Acknowledgement

3.5. References

[1] N. Semagina, L. Kiwi-Minsker, Catal. Rev. 51 (2009) 147-217.

[2] B. Coq, F. Figueras, J. Mol. Catal. A: Chem. 173 (2001) 117-134.

[3] H. Bonnemann, K. S. Nagabhushana, in: G. Schmid, N. Toshima, B. Corain (Eds.), Metal Nanoclusters in Catalysis and Material Science: The Issue of Size Control, Elsevier Science, Amesterdam, (2008) 21-48.

[4] F. Bonet, V. Delmas, S. Grugeon, R. Herrera Urbina, P-Y. Silvert, K. Tekaia-Elhsissen, Nanostruct. Mater. 11 (1999) 1277-1284.

[5] T. Teranishi, M. Miyake, Chem. Mater. 10 (1998) 594-600.

[6] X. Yan, H. Liu, K.Y. Liew, J. Mater. Chem. 11 (2001) 3387-3391.

[7] R. M. Rioux, H. Song, J. D. Hoefelmeyer, P. Yang, G. A. Somorjai, J. Phys. Chem. B 109 (2005) 2192-2202.

[8] X. Zuo, H. Liu, C. Yue, J. Mol. Catal. A: Chem. 147 (1999) 63-72.

[9] H. Zhang, N. Toshima, Appl. Catal., A 447-448 (2012) 81-88.

[10] P. Lu, T. Teranishi, K. Asakura, M. Miyake, N. Toshima, J. Phys. Chem. B 103 (1999) 9673-9682.

[11] Y. Wang, N. Toshima, J. Phys. Chem. B 101 (1997) 5301-5306.

[12] J. Shen, X. Yin, D. Karpuzov, N. Semagina, Catal. Sci. Technol. 3 (2013) 208-221.

[13] F. Papa, C. Negrila, G. Dobrescu, A. Miyazaki, I. Balint, J. Nat. Gas Chem. 20 (2011) 537-542.

[14] T. Teranishi, M. Hosoe, T. Tanaka, M. Miyake, J. Phys. Chem. B 103 (1999) 3818-3827.

[15] Y. Borodko, S. M. Humphrey, T. D. Tilley, H. Frei, G. A. Somorjai, J. Phys. Chem. C 111 (2007) 6288-6295.

[16] L. Qiu, F. Liu, L. Zhao, W. Yang, J. Yao, Langmuir 22 (2006) 4480-4482.

[17] J. Xian, Q. Hua, Z. Jiang, Y. Ma, W. Huang, Langmuir 28 (2012) 6736-6741.

[18] P. Sonstrom, M. Baumer, Phys. Chem. Chem. Phys. 13 (2011) 19270-19284.

[19] J. Monzo, M.T.M. Koper, P. Rodriguez, ChemPhysChem 13 (2012) 709-715.

[20] S.O. Blavo, E. Qayyum, L.M. Baldyga, V.A. Castillo, M.D. Sanchez, K. Warrington, M.A. Barakat, J.N. Kuhn, Top. Catal. 56 (2013) 1835-1842.

[21] R.M. Rioux, H. Song, M. Grass, S. Habas, K. Niesz, J.D. Hoefelmeyer, P. Yang, G.A. Somorjai, Top. Catal. 39 (2006) 167-174.

[22] Z.L. Wang, J.M. Petroski, T.C. Green, M.A. El-Sayed, J. Phys. Chem. B 102 (1998) 6145- 6151.

[23] C. Aliaga, J.Y. Park, Y. Yamada, H.S. Lee, C.K. Tsung, P. Yang, G.A. Somorjai, J. Phys. Chem. C 113 (2009) 6150-6155.

[24] H. Wang, H. Tang, J. He, Q. Wang, Mater. Res. Bull. 44 (2009) 1676-1680.

[25] B. Gehl, A. Fromsdorf, V. Aleksandrovic, T. Schmidt, A. Pretorius, J. Flege, S. Bernstorff, A. Rosenauer, J. Falta, H. Weller, M. Baumer, Adv. Funct. Mater. 18 (2008) 2398-2410.

[26] C. Peniche, D. Zaldivar, M. Pazos, S. Paz, A. Bulay, J. San Roman, J. Appl. Polym. Sci. 50 (1993) 485-493.

[27] J. Shen, H Ziaei-Azad, N. Semagina, J. Mol. Catal. A: Chem. 391 (2014) 36-40.

[28] H. Ziaei-azad, C.-X. Yin, J. Shen, Y. Hu, D. Karpuzov, N. Semagina, J. Catal. 300 (2013) 113-124.

[29] H. Ziaei-Azad, N. Semagina, ChemCatChem 6 (2014) 885-894.

[30] N. Semagina, E. Joannet, S. Parra, E. Sulman, A. Renken, L. Kiwi-Minsker, Appl. Catal., A 280 (2005) 141-147.

[31] S.J. Tauster, S.C. Fung, R. L. Garten, J. Am. Chem. Soc. 100 (1978) 170-175.

[32] R. F. Hampson, Jr., R. F. Walker, J. Res. Natl. Bur. Stand. 66A (1962) 177-178.

[33] R. F. Hampson, Jr., R. F. Walker, J. Res. Natl. Bur. Stand. 65A (1961) 289-295.

[34] Y.I. Vesnin, A.V. Nikolaev, Y.V. Shubin, S.V. Korenev, Ir-Pd Phase Diagram, ASM Alloy Phase Diagrams Center, P. Villars, editor-in-chief; H. Okamoto and K. Cenzual, section editors; http://www1.asminternational.org/AsmEnterprise/APD, ASM International, Materials Park, OH, (2006).

[35] H. B. Liu, U. Pal, J. A. Ascencio, J. Phys. Chem. C 112 (2008) 19173-19177.

[36] R. Huang, Y.-H. Wen, Z.-Z. Zhu, S.-G. Sun, J. Phys. Chem. C 116 (2012) 8664-8671.

[37] N. Sheppard, C. D. L. Cruz, Catal. Today 70 (2001) 3-13.

[38] F. Solymosi, J. Rasko, J. Catal. 62 (1980) 253-263.

[39] G. B. McVicker, R. T. K. Baker, R. L. Garten, E. L. Kugler, J. Catal. 65 (1980) 207-220.

[40] B.J. Kip, J. Van Grondelle, J.H.A. Martens, R.Prins, Appl. Catal. 26 (1986) 353-373.

[41] Y.-J. Huang, S. C. Fung, W. E. Gates, G. B. McVicker, J. Catal. 118 (1989) 192-202.

[42] R.J. Cvetanovic, Y. Amenomiya, Advan. Catal. 17 (1967) 103-149.

[43] K. J. Leary, J. N. Michaels, AlChE J. 34 (1988) 263-271.

Chapter 5: 4,6-DMDBT direct desulfurization enhancement by Ir addition to Pd catalysts

5.1. Introduction

After strict regulations on sulfur reduction of diesel fuel to 50 ppm were introduced a decade ago [1], newer environmental standards in many countries aim at even lower amounts in the range of 10-15 ppm [2-4]. This means that ultra-deep hydrodesulfurization (HDS) technologies are greatly required for new regulations to be met. Sulfur reduction to such levels mainly deals with the elimination of refractory sulfurous compounds such as dialkyl-dibenzothiophenes with alkyl groups adjacent to the sulfur atom, which makes the HDS process quite challenging [5], demanding a highly active catalytic system. 4,6-dimethyldibenzothiophene (4,6-DMDBT) is a typical molecule in this category and is usually selected as a model compound for deep HDS studies [1].

Numerous studies have been published on the HDS mechanism of dibenzothiophene (DBT) and its alkyl-substituted derivatives such as 4,6-DMDBT [6-11] unanimously proposing two different pathways for HDS of such molecules: i) direct desulfurization (DDS), the path of less hydrogen consumption achieved by the hydrogenolysis of C–S bond of the reactant leading to the formation of sulfur-free aromatic products and ii) hydrogenation (HYD), the path, which strongly relies on availability of hydrogen to initially hydrogenate an aromatic ring of the sulfurous molecule before the C–S bond breakage, yielding to a mixture of sulfur-free aromatic and/or saturated rings (depending on level of hydrogenation). Scheme 5.1 shows the DDS and HYD pathways in HDS of 4,6-DMDBT.
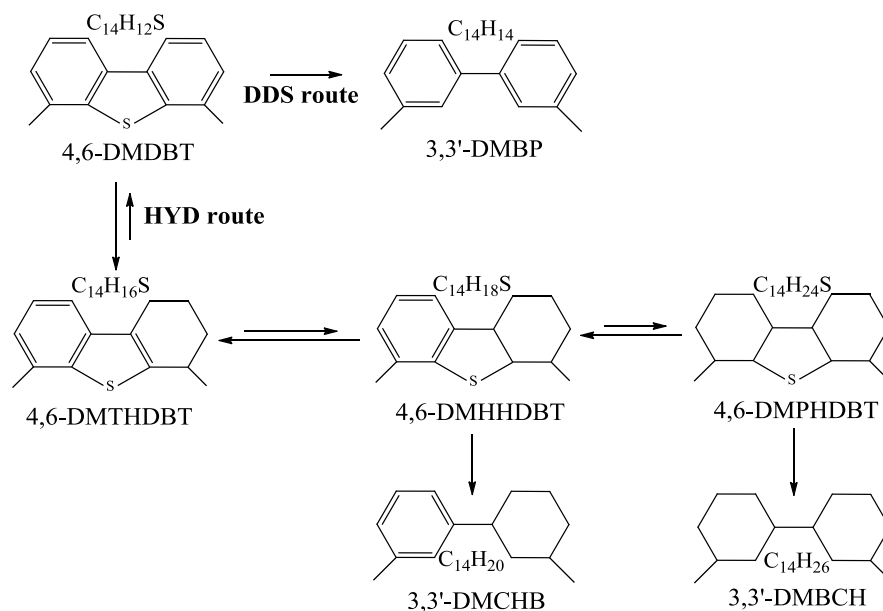
Scheme 5.1. The DDS and HYD reaction pathways in the HDS of 4,6-DMDBT at 300°C and 5 MPa. Reprinted from [24] with permission from Elsevier.

In general, DDS requires a perpendicular adsorption of the reactant on the catalyst surface (i.e. σ mode), while HYD proceeds with parallel bonding of the reactant with the surface (i.e. π mode) [1,6,12]. The HDS of 4,6-DMDBT mainly takes place through the HYD path as the presence of methyl groups near the sulfur atom results in steric hindrance and prevent the perpendicular bonding [5,12,13]. This way, hydrogenation of one aromatic ring is reported to weaken the hindrance in the case of alkyl substituted DBTs, which is explained by the steric change happening in the plane of the hydrogenated ring compared to the remaining aromatic ring(s) that reduces the hindrance imposed by the alkyl substitution [12]. Thus, it is suggested that a good hydrogenation catalyst is required for deep HDS of 4,6-DMDBT [14]. However, the goal in the field is to realize the DDS path that requires less hydrogen consumption and allows maintaining high octane number of the desulfurized feed [15].

Transition metal supported catalysts primarily based on Co/Mo and Ni/Mo, have been conventionally used for HDS studies [11,13,16-24], however, they are not active enough for refractory compounds desulfurization to acceptable levels. It is suggested that either catalyst volume must be increased several fold or higher pressures are required, which is technologically challenging [25,26], that is why the most viable solution is to add a second-stage hydrotreater with more active noble metal catalysts for ultra-deep desulfurization of initially pretreated fuels with 250-300 ppm S [3], largely composed of the most refractory molecules such as 4,6-DMDBT.

The sulfur resistance of noble metals and their HDS activity can be increased by alloying and/or using acidic supports such as zeolites [14]. The existing works on the use of noble metals for 4,6-DMDBT HDS are almost exclusively limited to Pd- and Pt-based catalysts [1-3, 14,24,27-30]. Herein, to the best of our knowledge, we report for the first time the effect of Ir addition to Pd for the 4,6-DMDBT HDS. The presence of Pd warrants a high hydrogenation activity [2] and Ir may act to improve the DDS selectivity due to its proven hydrogenolysis activity [31-34] and allow reducing the required operating hydrogen pressure. As will be shown, the Ir addition to Pd leads to up to a 3-fold increase in S-free products selectivity and enhances the DDS path selectivity contribution almost 5 times.

Since the industrial feeds also contain a variety of desirable octane- and cetane-number enhancing hydrocarbons and undesired polycyclic aromatic hydrocarbons (PAH) [35-37], we also evaluated the 4,6-DMDBT HDS in the presence of indane (benzocyclopentane), which can serve as a model compound for competitive hydrogenolysis (ring opening) of a naphthenic ring and hydrogenation of the aromatic ring.

Depending on the reaction conditions, the hydrocarbon could be either hydrogenated or remain intact at the maintained high levels of S removal from the refractory sulfur compound.

5.2. Experimental

5.2.1. Materials

$H_2IrCl_6 \cdot xH_2O$ and H_2PdCl_4 were used as metal precursors. PVP (Avg. Mw: 40,000) as stabilizing agent and γ-Al_2O_3 (average pore size 58 Å, SSA 155 m^2/g provided by the manufacturer) as the support material obtained from Sigma-Aldrich. Ethanol and acetone were obtained from Fisher Scientific. Milli-Q water used as solvent and for washing the synthesis flasks. All the gases were ultra-high purity (i.e. 99.999%) and purchased form Praxair. For catalytic reactions n-decane (99.4%) from Fisher Scientific, n-dodecane ($\geq$ 99%), indane (95%) and 4,6-dimethyldibenzothiophene (97%) all from Sigma-Aldrich were used.

5.2.2. Catalyst preparation

Mono- and bimetallic Pd and Ir nanoparticles were synthesized by the colloid chemistry techniques, deposited on γ-Al_2O_3 using acetone (as precipitant) and calcined 2 h at 400°C under air; the details has been explained previously [34]. Briefly, about 0.1 mmol of either precursor added to a 500-ml three neck flask followed by the addition of Milli-Q water and ethanol with the approximate volume ratio of 3:2. Nanoparticles were synthesized with the PVP/metal molar ratio of 5:1, which helps to prevent the agglomerations of as synthesized particles. The solution was kept under vigorous stirring at the reflux temperature of water-ethanol for about 3 h. Color of the mixture changed to dark

brown at the end of synthesis without any precipitate, which is a simple indication of forming colloidal nanoparticles. Bimetallic nanoparticles with random alloy structure were synthesized by the simultaneous reduction of both precursors, as explained elsewhere [34]. Three types of nanoparticles synthesized this way, two with a similar molar ratio only for mass transfer limitation study. The exact Pd:Ir molar ratio of the synthesized alloys determined by neutron activation analysis (NAA) performed on supported calcined catalysts and were found to be 8.8:1, 1.5:1 and 1.4:1. Since for catalytic studies samples are discussed based on the weight ratio, hereafter they are referred as Pd83Ir17 (AL), Pd45Ir55 (AL) and Pd43Ir57 (AL), respectively, where the AL symbol in parentheses resembles the initial structure of nanoparticles (i.e. alloy).

In addition to alloy type nanoparticles, two samples were also prepared with the so-called core-shell structure. Hydrogen sacrificial technique was used for that, which has been explained before [34]. The PVP/metal(s) molar ratio of 5:1 kept here as well. Pd nanoparticles were treated after synthesis with H_2 for 1.5 h to form hydride species on their surface, which was further replaced by Ir atoms forming a shell around Pd core particles. NAA indicated 3.5:1 and 0.8:1 for the molar ratio of these nanoparticles supported on γ-Al_2O_3, and hereafter they are recalled by their weight ratio as Pd66Ir34 (C/S) and Pd30Ir70 (C/S), where the C/S symbol stands for the initial structure (i.e. core-shell).

5.2.3. Catalyst characterization

Neutron activation analysis as well as the pulse chemisorption of CO was performed as described previously [38]. The CO chemisorption analyses were done on samples calcined at 400°C and reduced in-situ by hydrogen up to 400°C; a treatment to ensure the complete removal of PVP residues from catalytic surface [38].

Diffuse reflectance infrared Fourier transform spectroscopy (DRIFTS) of adsorbed pyridine was studied with a Nicolet Nexus670 spectrophotometer in the range of 800-3000 cm^{-1}, averaged over 128 scans. Analysis meant to investigate the acidity of the support material (i.e. γ-Al$_2$O$_3$); however monometallic Ir and Pd supported samples were also studied. Calcined samples (2 h in air at 400°C) were reduced in a fixed bed reactor under hydrogen at 375°C and kept for 1 h, followed by cooling down at the same atmosphere to ambient. Later, they were treated with nitrogen for few minutes and then the nitrogen flow passed through a bubbler and saturated with pyridine before flowing to the samples for about 1 h, details of this system has been explained before [38]. Pure nitrogen was flowed to the system afterwards for 30 minutes at 100°C to desorb the physically adsorbed pyridine and finally the DRIFTS spectra were recorded immediately. An overnight dried potassium bromide (KBr) from Sigma-Aldrich used for collecting the background and dilution of the samples. One analysis was also performed on calcined γ-Al$_2$O$_3$ without pyridine treatment as blank. OMNIC software used to transform the reflectance spectra to Kubelka-Munk units.

The specific surface area and the pore size distribution of the support material (γ-Al$_2$O$_3$) were collected by nitrogen adsorption-desorption isotherms using a Quantachrome Autosorb 1MP analyzer at 77.3 K. Sample was degassed at 200°C for 2 h before analysis. Brunauer-Emmett-Teller (BET) method used for the calculation of the specific surface area followed by the Barrett-Joyner-Halenda (BJH) technique for determination of pore size distribution.

5.2.4. Catalytic activity measurements

The catalytic tests were performed in a continuous fixed bed reactor of 22" length and ½" i.d. Noble metal supported catalysts were activated by in-situ reduction at 300°C for 1 h before the reaction. An initial activity evaluation in hydrodesulfurization (HDS) of 4,6-dimethyldibenzothiophene (4,6-DMDBT) was performed at 300°C and 5 MPa using 0.09 g of the supported catalysts diluted with about 4 g of #100 mesh SiC. A mixture of about 0.5 wt.% 4,6-DMDBT (about 800 ppmw S), 3.5 wt.% dodecane (internal standard) balanced with n-decane (as solvent) was fed to the top of the reactor by a Series II high pressure pump, where it mixed with hydrogen and flowed to the system (H$_2$ / liquid ratio of 16 mol / mol and WHSV = 30 h^{-1}). After the initial evaluation, an about 0.18 g of selected catalysts was used for further studies with increasing the flow of hydrogen and oil in a same ratio to increase the WHSV. Later harsher condition (i.e. H$_2$ / liquid = 4 and 8 mol / mol) was studied for the most promising catalysts during 72 h runs to check for reversible deactivation. One run was also performed at 3 MPa to check for pressure sensitivity. All the HDS reactions mentioned above were studied after an overnight (15 h) stabilization period at reaction conditions to diminish the possible initial deactivation effects. A 150 ml stainless steel condenser used to collect liquid samples and for every data point, we let the condenser to be washed by at least 20 ml of the liquid product at the new condition before a sample is taken. . Liquid samples were collected every 2 h after a 15 h stabilization period. A difference of only 2-3% was observed after the second sample (i.e. 17 h on stream) indicating that a steady-state condition has been established after the stabilization period. This method adapted from the reported works on HDS of 4,6-DMDBT [24], also confirmed here with several trial and errors to ensure the system has reached to steady state

and the sample represent the new condition. A second condenser was used in parallel to the first one and connected to the system with the same pressure. Such a design allowed switching flow to another path at the time of sampling, thus preventing pressure fluctuations and instabilities, while the sample is collected. Liquid samples were analyzed off-line using a Varian 430 gas chromatogram (GC) equipped with a CP-Sil 8 CB Varian capillary column (50 m length and 0.25 mm inner diameter) and flame ionization detector (FID). The oven was heated with a ramping rate of 10°C/min up to 300°C, which allowed a clear separation of reactant as well as the reaction products. Various peaks observed, which agreed with the results reported in the literature [24] (also confirmed by GC-MS): 3,3′-dimethylbicyclohexyl (3,3′-DMBCH) and 3,3′-dimethylcyclohexylbenzene (3,3′-DMCHB), as the desulfurized products of hydrogenation (HYD) path, 3,3′-dimethylbiphenyl (3,3′-DMBP), the final product of the direct desulfurization path (DDS), and 4,6-dimethyltetrahydrodibenzothiophene (4,6-DMTHDBT), 4,6-dimethylhexahydrodibenzothiophene (4,6-DMHHDBT), and 4,6 dimethylperhydrodibenzothiophene (4,6-DMPHDBT), as the sulfurous intermediates in the HYD path, which are observed in Scheme 5.1.

Quantification of the GC areas was completed by analyzing calibration mixtures containing n-decane, dodecane (as an internal standard), 4,6-DMDBT and 3,3′-DM-BP. Five calibration mixtures with different concentrations of 4,6-DMDBT and 3,3′-DM-BP were used so that the calibrating lines cover the whole range of conversions. Sulfur containing intermediates were quantified similar to 4,6-DMDBT, and the sulfur-free products were treated the same as 3,3′-DMBP due to structural similarity.

The absence of mass transfer limitation studied with two samples of the same Pd / Ir ratio (Pd45Ir55 (AL) and Pd43Ir57 (AL)) but with almost doubled metal loading using the Madon-Boudart method [39] tested on). A blank run with pure γ-Al$_2$O$_3$ showed a negligible activity of the support (about 2% conversion), implying the necessity of metallic centers for catalytic activity.

The following terms are used in the analysis of the results:

-) DMDBT conversion: the amount of 4,6-DMDBT converted during the HDS reaction divided by the initial amount of 4,6-DMDBT in the feed.

-) HDS conversion: the total amount of sulfur removed by the HDS reaction divided by the initial amount of sulfur in the feed (as 4,6-DMDBT).

-) Selectivity to sulfur-free products: the amount of sulfur-free products (i.e. DMBCH, DMCHB and DMBP) divided by the amount of 4,6-DMDBT converted.

-) Selectivity to sulfurous intermediates: the amount of sulfur-containing intermediates (i.e. DMTHDBT, DMHHDBT and DMPHDBT) divided by the amount of 4,6-DMDBT converted.

-) Selectivity to DDS path: the amount of DMBP divided by the amount of 4,6-DMDBT converted.

-) Selectivity to HYD path: the amount of (DMBCH, DMCHB, DMTHDBT, DMHHDBT and DMPHDBT) divided by the amount of 4,6-DMDBT converted.

-) Selectivity to S-free products in HYD path: the amount of DMBCH and DMCHB divided by the amount of 4,6-DMDBT converted.

All the terms mentioned above are calculated on molar basis.

The high pressure hydrogenation of indane was studied with the same fixed bed system as described above using 0.32 g of the selected supported catalysts diluted with SiC. A mixture containing 2 wt.% indane, 2 wt.% dodecane (as internal standard) balanced with n-decane was pumped to the system. The reactions were studied at 5 MPa at three temperatures of 280, 300 and 320°C, after a stabilization period of 15 h at reaction conditions. Two temperatures were studied every day with a 5 h time interval making sure that the steady stated has been achieved; condenser was washed as described previously before taking a new sample. One reaction was also studied at different pressures. A relatively harsh operating condition always used for these reactions corresponding to the H_2 / liquid ratio of 4 mol / mol and WHSV = 45 h^{-1}. Liquid samples were analyzed with the same GC explained above; however, in order to separate the main reaction product, i.e. hexahydroindane, from n-decane, a 40 min isothermal program at 75°C was used. Ring opening products, i.e. n-propylcyclohexane, ethylcyclohexane and methylcyclohexane was confirmed but in negligible amount at the conditions studied (less than 1 mol % in total). These products have been also reported elsewhere for the high pressure ring opening of indane [40].

Finally, the high pressure hydrogenation of indane was studied in the presence of 300 ppm sulfur as 4,6-DMDBT at 5 MPa and 300, 320 and 350°C. 0.32 g of two most promising samples used for each reaction. Catalytic experiments started after an overnight (15 h) stabilization period, and two operating conditions of i) H_2 / liquid = 16 mol / mol, WHSV = 8.5 h^{-1} (referred as light conditions) and ii) H_2 / liquid = 4 mol / mol, WHSV = 45 h^{-1} (referred as harsh conditions) were studied in 72 h. Sample collection and GC analysis

completed using the same way explained above. The carbon balance deviation in all the above mentioned reactions were in the range of 5 % and never exceeded 10%.

5.3. Results and discussion

5.3.1. Characterization results

The nitrogen adsorption-desorption isotherms and the pore size distribution profile of the support material (γ-Al$_2$O$_3$) after calcination at 400°C is observed in Figure 5.1. The isotherms observed are type IV, indicating the presence of mesopores and the pore size distribution show relatively uniform particles in the range of 3-12 nm. The average pore size and the BET surface area calculated from results of Fig. 5.1 are 4.3 nm and 162 m^2/g, respectively, which are in good agreement with the average specification provided by the manufacturing company (i.e. 5.8 nm and 155 m^2/g).
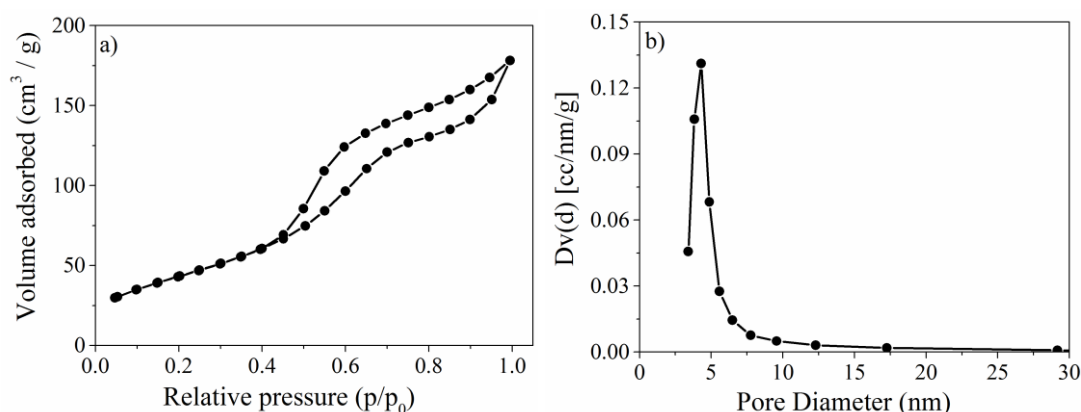
Fig. 5.1. Nitrogen adsorption-desorption isotherm (a) and pore size distribution profile (b) of γ-Al$_2$O$_3$ calcined in air at 400°C.

The surface acidity of γ-Al$_2$O$_3$ as well as monometallic Pd and Ir supported catalysts were studied by the DRIFT spectra of adsorbed pyridine in the range of 1400-1700 cm^{-1} and presented in Figure 5.2. Five peaks are observed for γ-Al$_2$O$_3$ at about 1446,

1490, 1578, 1596 and 1615 cm^{-1}, respectively, which agree with the literature data regarding the presence of strong (band at 1446 cm^{-1}), medium strong (1615 cm^{-1}) and weak Lewis acid sites (1578 and 1596 cm^{-1}) presented on the surface [41,42]. Acidity is reported to originate from the presence of surface hydroxyl groups as well as the unsaturated Al^{3+} coordination configurations [41]. However, no adsorption band is discernible at about 1540 cm^{-1} implying the absence of Brønsted acid sites [42]. The spectra for the supported monometallic Pd and Ir are quite similar to that of pure γ-Al$_2$O$_3$ with same peak positions suggesting that the presence of metals does not alter the surface acidity in a significant manner. A blank run performed on calcined γ-Al$_2$O$_3$ without any adsorbed pyridine is also observed in Figure 5.2 as a blank run.
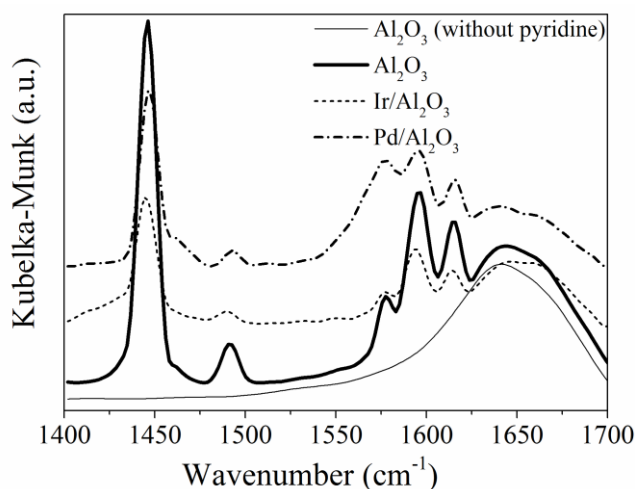
Fig. 5.2. DRIFT spectra of adsorbed pyridine on γ-Al$_2$O$_3$ and selected γ-Al$_2$O$_3$ supported catalysts.

Table 5.1 presents the results of CO chemisorption performed on calcined samples after in-situ reduction at 300°C (same pretreament before catalytic studies). Values reported for the average particle size have been calculated using the CO/Pd and CO/Ir ratios of 0.6 [43] and 1.19 [44], respectively. From the results of Table 1, it is clear that CO uptake decreases by increasing the molar ratio of Pd / Ir, which is attributed to the size

146

increase of Pd particles [38]. The presence of an Ir shell with its higher melting point than Pd is responsible for the higher thermal resistance in core-shell catalysts. The sizes of 3.4 and 3.5 nm observed in the case of core-shell samples, Pd66Ir34 (C/S) and Pd30Ir70 (C/S) respectively, are similar to the previously reported sizes for such core-shell particles after calcination at 400°C, without sign of sintering as confirmed by TEM [38].

Table 5.1. Characteristics of the studied catalysts.

Catalyst, (weight ratio)	Pd / Ir loadings, wt.%	CO uptake[a], mol_{CO} / $mol_{(Pd+Ir)}$	Pd / Ir molar ratio	Average particle size*, nm
Pd	0.305 / 0.0	0.04	1 /0	17.2
Pd83Ir17 – AL	0.233 / 0.047	0.07	10	9.5
Pd66Ir34 – C/S	0.259 / 0.131	0.22	3.3	3.4
Pd45Ir55 – AL	0.185 / 0.225	0.16	1.4	5.2
Pd43Ir57 – AL	0.080 / 0.107	0.18	1.4	4.6
Pd30Ir70 – C/S	0.109 / 0.261	0.26	0.8	3.5
Ir	0.0 / 0.231	0.67	0.0	1.9

[a] determined by CO chemisorption after calcination and reduction at 400°C.

5.3.2. Catalytic activity results

5.3.2.1. HDS of 4,6-DMDBT

Fig. 5.3 presents catalyst activity in terms of DMDBT conversion and selectivity to sulfur-free products (i.e. DMBCH, DMCHB and DMBP). The bimetallic samples unanimously show higher activities than their monometallic counterparts of Pd and Ir. Iridium enrichment of the nanoparticle shell in core-shell samples brings down the activity as compared to the alloy samples at similar Pd/Ir weight ratio. Ir addition is also responsible for the increased selectivity towards direct desulfurization to DMBP up to 23%

147

vs. 4% for monometallic Pd. This behaviour can originate from the well-known tendency of Ir for hydrogenolysis [32]. The activity and selectivity enhancement trends are valid over a range of WHSV's, as shown in Fig. 5.4.
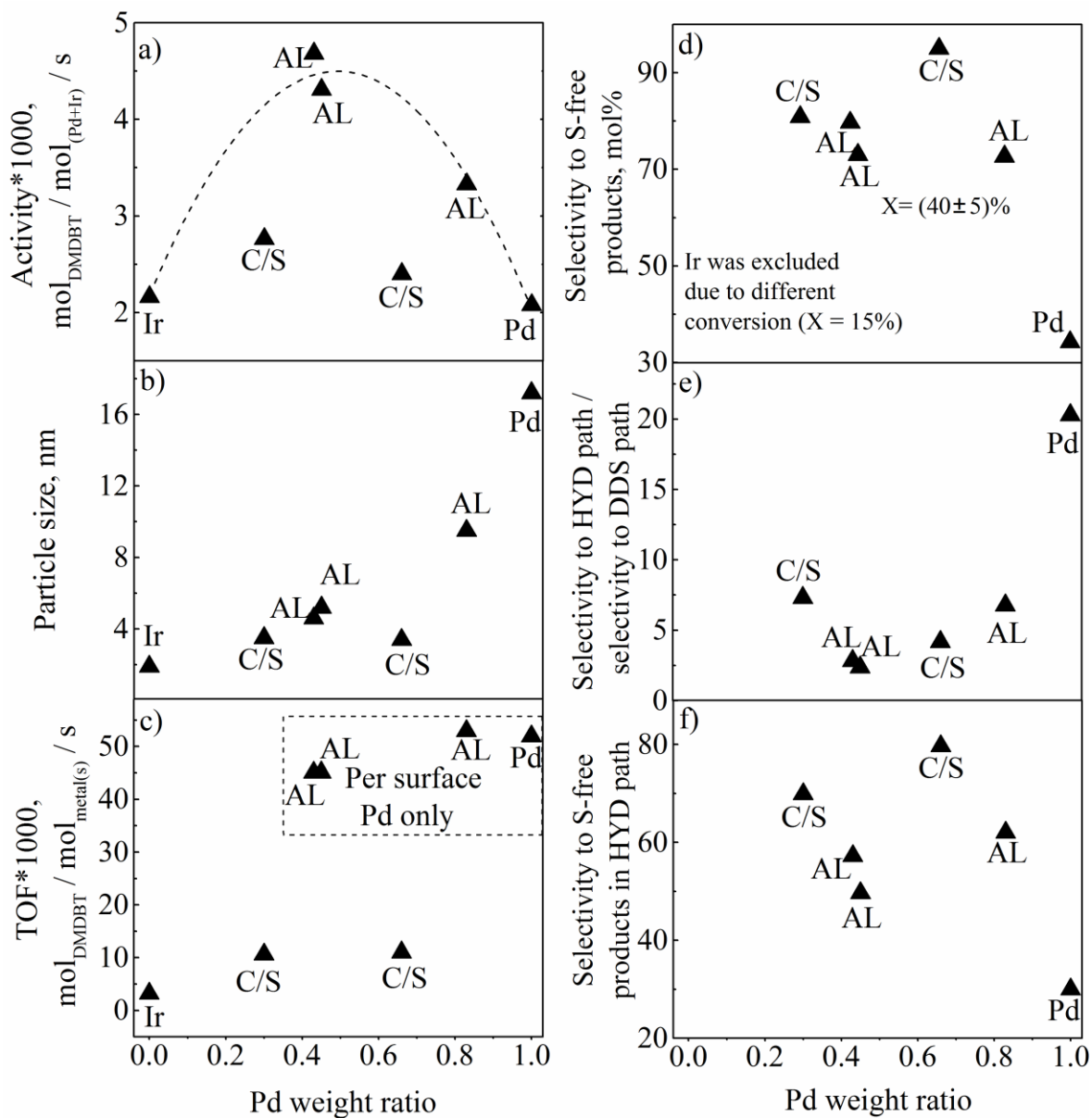

Fig. 5.3. Activity (a), particle size (b), TOF (c), selectivity to sulfur-free products (d), selectivity to HYD path divided by selectivity to DDS path (e) and selectivity to S-free products in HYD path (f) in the HDS of 4,6-DMDBT at 300°C and 5 MPa (WHSV: 30 h^{-1}, amount of catalyst: 0.09 g). Conversions are 40 ± 5 %, except for Ir (15%).

This type of activity and selectivity enhancement has been reported previously in noble metal alloys studied in HDS reactions [2,24,45,46], which is sometimes attributed to synergism happening between two metals [24]. Two types of synergisms are suggested in literature, textural and chemical synergism [24]. A textural effect is related to the changes in the number of active sites upon mixing, which may be explained by dispersion changes. The chemical synergism is described as the creation of new sites in a bimetallic sample, not available in monometallic counterparts. In the current work, a dispersion change by mixing is obvious from the CO chemisorption results of Table 5.1 that verifies the thermal resistance increase of Pd when alloyed with Ir. The CO uptake values were used to calculate the catalytic activity per number of active sites (assumed as 1:1 CO : site ratio), which are presented in Fig. 5.3c. Monometallic Pd shows activity per surface atoms i.e. (TOF ($\times$1000)) at ~50 s^{-1} vs. 3 s^{-1} for monometallic Ir. Due to the large difference, the TOFs for Pd-Ir alloys samples were calculated only based on Pd surface atoms assuming the same Pd/Ir surface ratio as in the bulk. The all four values for Pd, Pd8317, Pd45Ir55 and Pd43Ir57 were amazingly consistent as 48±4 s^{-1}, indicating that Pd dominates the catalyst function and no new Pd-Ir sites are created. It is clarified here that the TOFs are calculated for the catalysts at the same reaction conditions (excluding monometallic Ir with the conversion of 15%): at conversion levels of (40± 6) %, same flow rate and the same Pd surface atoms loading in the reactor (in the range of 1.10 - 1.47 $\times$ 10^{-2} mg). The observed differences in activities (Fig. 5.3a) are only due to textural effects (size change). The size decrease also may explain the DDS selectivity improvement of Pd-Ir alloys vs. Pd: a smaller particle size is expected to increase the DDS selectivity, since more edge atoms exist on smaller particles and may contribute to the improved perpendicular adsorption of

DMDBT required for the DDS. However, when the particle size is decreased for the monometallic Ir and core-shell with Ir enrichment of the nanoparticle shell, turnover frequencies drop towards the lowest value for the monometallic Ir. This is in line with the literature data on high Pd activity in DMDBT HDS. Enhancements in DDS path or HYD path selectivities (Fig. 5.3e) follow the trends of nanoparticle shell enrichment with Ir or Pd, respectively. Selectivity to S-free products in HYD path also enhances with shell enrichment with Ir indicating that even in hydrogenation path Ir is responsible for the C-S bond hydrogenolysis. Thus, the observed Pd activity increase with Ir addition is mostly due to the increased thermal resistance of the alloyed particles and their smaller size. This effect is counterbalanced by the intrinsic activity decrease by adding less active Ir. It is likely that no new bimetallic active sites were created and no intrinsic synergism exists in the developed catalysts.

Catalyst stability studies were performed on the most active catalysts (i.e. Pd66Ir34 C/S and Pd83Ir17 AL) in 72 h runs with the initial sulfur level of 300 ppm. The conversions and the total sulfur in final products are presented in Figure 5.5 and Figure 5.5 inset, respectively. To speed up the catalyst deactivation, larger WHSV and lower H_2/liquid ratios were applied in the second day, and on the third day the values were returned to the ones on the first day of study. As seen from Fig. 5.5a and b, there is no appreciable difference in the catalyst activity on days 1 and 3.

The pressure effect was studied for the Pd66Ir34(C/S) with the feed having 300 ppm sulfur (as 4,6-DMDBT). The reactions were performed at $300^{o}C$ and at two different pressures of 3 and 5 MPa, while the WHSV was altered the same way as previous runs (i.e. 15, 22.5 and 30 h^{-1}). Results collected at different WHSV's (Fig. 5.6) follow the same

trend. Only a 13% decrease of in the conversion of 4,6-DMDBT accompanied by a 2%
reduction of selectivity to sulfur-free products is observed at 3 MPa compared to 5 MPa.
The hydrogen pressure is expected to affect only the hydrogenation pathway: indeed, the
pressure reduction positively affects the DDS path selectivity. Since the HYD pathway rate
decreases at the reduced pressure, the contribution from the DDS path, requiring
significantly less hydrogen, increases which leads to the improved selectivity.
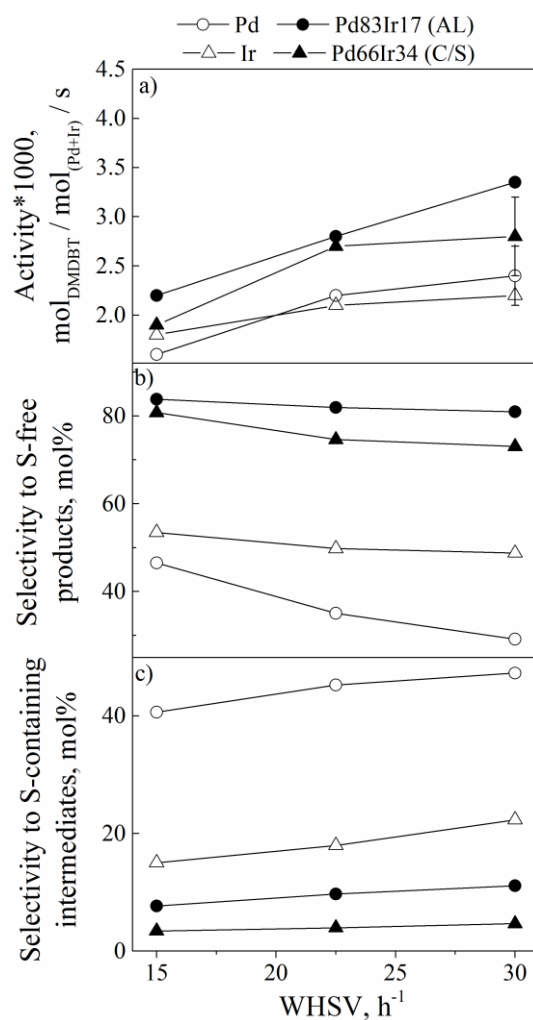
Fig. 5.4. Catalytic activity (a), selectivity to sulfur-free products (b) and selectivity to sulfurous
intermediates (c) in the HDS of 4,6-DMDBT over selected supported catalysts at different WHSV
values at 300°C and 5 MPa (H$_2$ / liquid: 16 mol / mol).
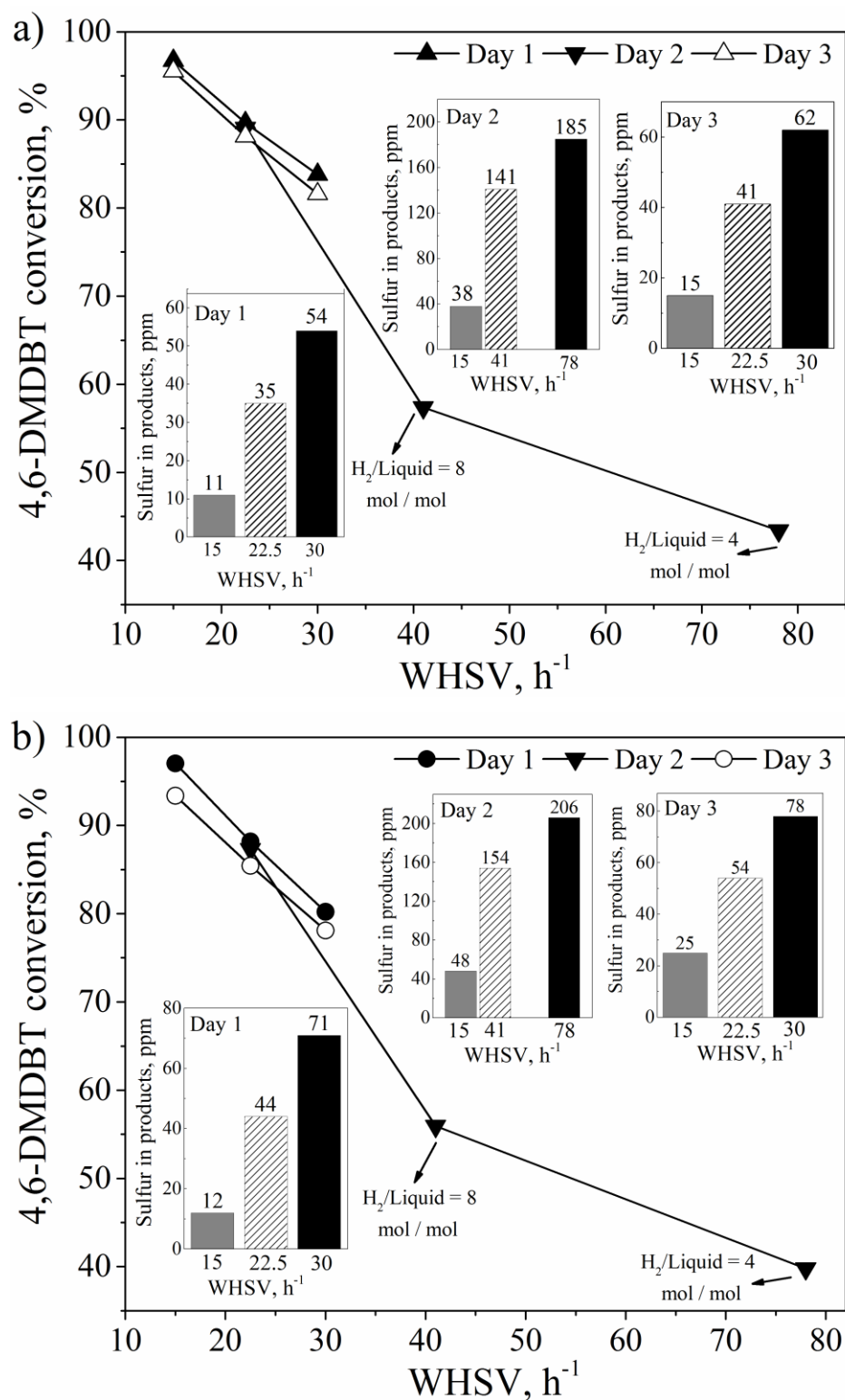
Fig. 5.5. Conversion of 4,6-DMDBT and total sulfur in the final products at various operating conditions over a) Pd66Ir34 (C/S) and b) Pd83Ir17 (AL) supported catalysts (H$_2$ / liquid: 16 mol / mol, unless indicated on the graphs).
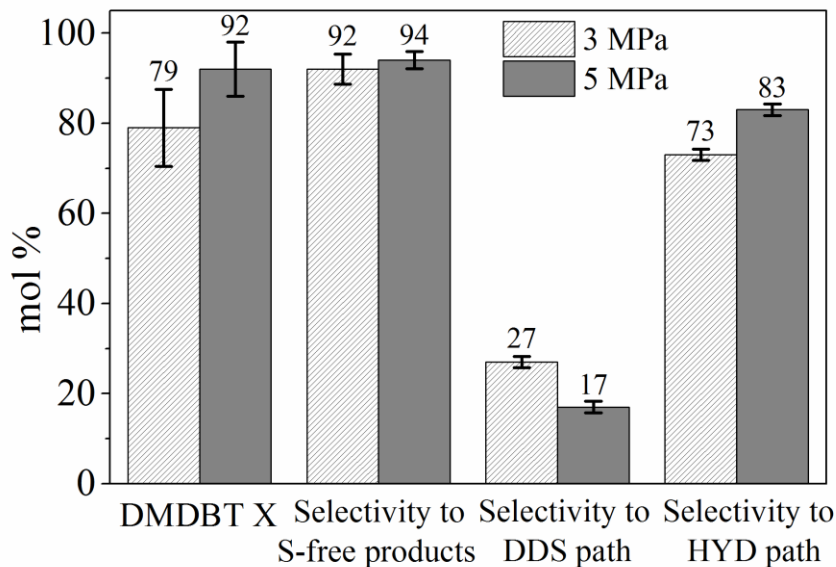
Fig. 5.6. The range of conversions, selectivities to sulfur-free products, DDS and HYD selectivity values in the HDS of 4,6-DMDBT over Pd66Ir34 (C/S) catalyst at 300°C and different pressures for WHSV's of 15, 22.5 and 30 h^{-1}, H$_2$ / liquid: 16 mol / mol.

5.3.2.2. High-pressure hydrogenation of indane

We have recently reported the atmospheric ring opening of indane over Pd-Ir supported bimetallic catalysts at 350°C, where Ir shows an outstanding activity for opening the five membered naphthenic ring of indane at atmospheric hydrogen pressure [34]. However, the reaction follows a different pathway at high pressures. Fig. 5.7 presents the conversion of indane over selected γ-Al$_2$O$_3$ supported catalysts at 5 MPa and 280-320°C. The only reaction product quantified for all catalysts was hexahydroindane, the product of complete hydrogenation. Selectivity to ring opening products (n-propylcyclohexane, ethylcyclohexane and methylcyclohexane) were always less than 1% during the whole temperature range studied. No significant cracking (within 5% carbon balance error) was observed even at 350°C. The same reaction products and mechanism have been previously reported at 4 MPa for Pt-Ir bimetallic catalysts [40]. A blank experiment with pure γ-Al$_2$O$_3$

confirmed no activity for the support material. Ir catalyst is more active than Pd for hydrogenation of indane, even though Pd is known to be a better hydrogenation catalyst and the relatively low activity of Ir for hydrogenation has been reported elsewhere [47]. A study performed on bimetallic Pd-Ir supported catalysts for hydrogenation of tetralin at $350^{\circ}C$ and 4 MPa showed an activity of about two orders of magnitude higher for Pd comparing with Ir, where the activity of bimetallic catalysts lies in between of two monometallic counterparts [48]. In the current study, large size of monometallic Pd particles may explain the difference. The bimetallic catalysts with smaller particle size and higher Pd content show higher activities as compared to the monometallic Pd. The Fig. 5.7 inset shows the expected reaction rate decrease with the hydrogen pressure decrease; no selectivity variations were observed.
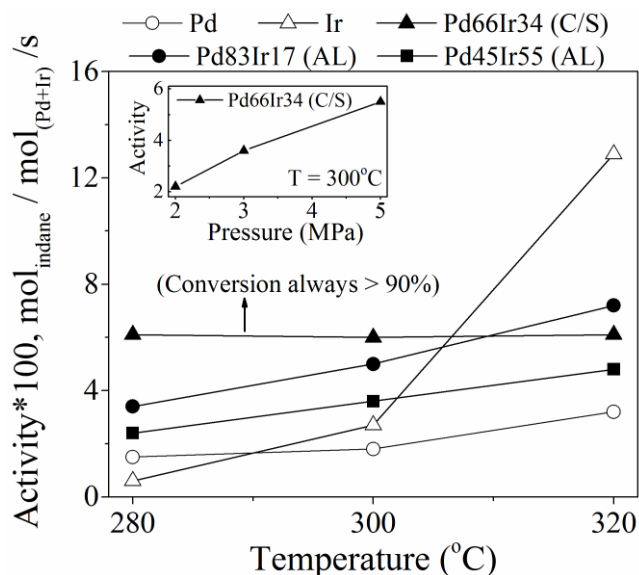
Fig. 5.7. Catalytic activity in high pressure hydrogenation over selected catalysts at various temperatures and 5 MPa (WHSV: 45 h^{-1}, H_2 / liquid: 4 mol /mol). Inset shows the activity of Pd66Ir34 (C/S) at $300^{\circ}C$ and various pressures.

Thus, at the high-pressure conditions, indane is effectively hydrogenated on the studied bimetallic catalysts with activities comparable or even exceeding the values for

154

4,6-DMDBT HDS and thus can serve as a model reaction competing for hydrogenation active sites with the HYD route of the desulfurization process.

5.3.2.3. 4,6-DMDBT hydrodesulfurization in the presence of indane

The effect of indane presence in the feed on HDS of 4,6-DMDBT was investigated for the most active catalysts, i.e. Pd83Ir17 (AL) and Pd66Ir34 (C/S), by introducing 300 ppm sulfur as 4,6-DMDBT to the indane feed at different temperatures of 300, 320 and 350°C, the results are presented in Fig. 5.8. The indane-to-DMDBT molar ratio in the feed was kept high as 18 mol/mol to provide excess of the competing reactant for DMDBT HDS. For each temperature the reactions were monitored first at WHSV of 8.5 h^{-1}, H$_2$ / liquid: 16 mol /mol (Fig. 5.8a) and then at 45 h^{-1}, H$_2$ / liquid: 4 mol /mol (Fig. 5.8b). A complete 4,6-DMDBT HDS was observed for both catalysts at the lower WHSV conditions over the whole temperature range, while the conversion of indane reaches only 5% at 300°C. 4,6-DMDBT HDS resulted in sulfur-free products and the hydrogenation of indane resulted in hexhydroindane only, without any selectivity to ring opening products or cracking. These results show that both catalysts are highly selective to the conversion of 4,6-DMDBT than that of indane. The same tendency has been reported elsewhere in the hydrogenation of tetralin in the presence of 1000 ppm DBT, where it was reported that the electron density of noble metal (Pt) decreases by sulfur poisoning, which increases the bonding strength between aromatics and noble metal [49]. By switching to the higher WHSV (Fig. 8b), ~60% conversion of 4,6-DMDBT is achieved at 350°C and almost no conversion for indane over the whole temperature range.

Thus, the developed catalysts allow for efficient S removal from a refractory sulfur compound without hydrogenolysis or cracking of naphthenic or aromatic rings. The

hydrogenation contribution is not significant; it may bring either positive (cetane number increase by aromatic hydrogenation and decrease of undesirable polycyclic aromatic hydrocarbons to less toxic saturated compounds) or negative effects on the fuel quality (reduction of valuable high-octane aromatics) and must be either reduced or increased on a case-to-case basis for a target product.

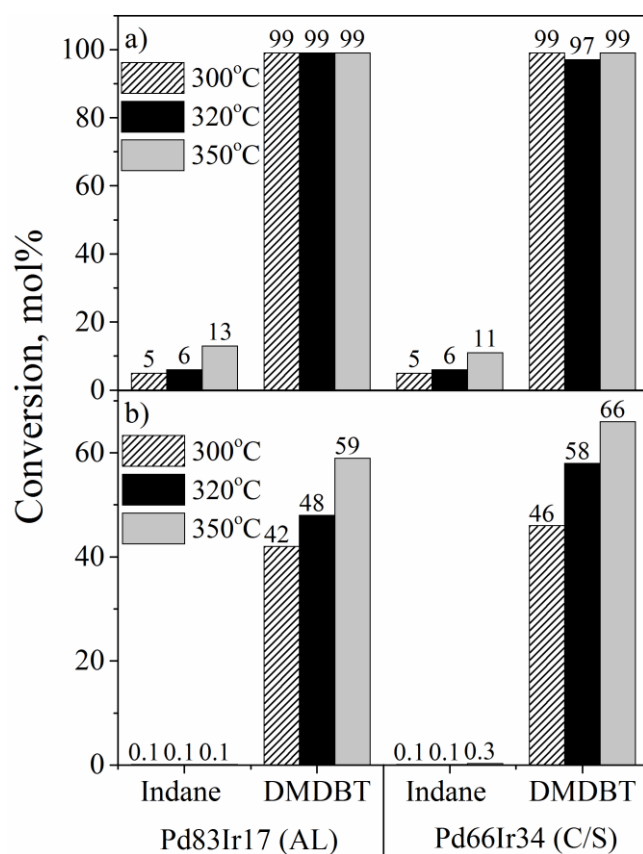Fig. 5.8. Catalytic conversion of a mixture including: 2 wt.% indane and 300 ppm sulfur as 4,6-DMDBT at various temperatures and 5 MPa over selected catalysts: a) WHSV: 8.5 h^{-1}, H_2 / liquid: 16 mol /mol, and b) WHSV: 45 h^{-1}, H_2 / liquid: 4 mol /mol. (Note: metal loadings are different: 0.233 wt.% Pd and 0.047 wt.% Ir in Pd83Ir17, as well as 0.259 wt.% Pd and 0.131 wt.% Ir in Pd66Ir34).

5.4. Conclusions

Bimetallic Pd-Ir nanoparticles were synthesized in the presence of PVP, deposited on γ-Al$_2$O$_3$ and subjected to 400°C calcination-reduction treatment to ensure PVP removal. The treatment did not affect the particle size of Ir-enriched samples, but resulted in severe sintering of Pd-enriched samples. Ir-enriched bimetallic samples were found more active than Pd-enriched samples in 4,6-DMDBT hydrodesulfurization at 5 MPa and 300°C, which was attributed to the large size of the Pd-enriched nanoparticles. The bimetallic samples exhibited the same turnover frequencies calculated per surface Pd as monometallic Pd implying that the Ir with its lower turnover frequencies serves simply as a dispersing agent for Pd in terms of DMDBT conversion. However, Ir presence affected greatly the hydrodesulfurization pathway distribution: while Pd is responsible for hydrogenation, Ir presence provides C-S hydrogenolysis both in direct desulfurization and hydrogenation pathways. As a result, the Ir addition to Pd catalysts enhances the selectivity towards S-free products 3 times and also increases the DDS path selectivity contribution almost 5 times. The effects are attributed both to the known high hydrogenolysis activity of Ir and also to the smaller particle size of Ir-enriched samples. Since the DDS pathway does not require as mush hydrogen as the HYD pathway, when the reaction pressure was reduced from 5 to 3 MPa, no significant changes in activities or selectivities were observed for Pd-Ir catalysts.

The bimetallic catalysts also showed similar activities in indane hydrogenation without any cracking or ring opening, but when the feed consisted of indane and 4,6-DMDBT (18 mol/mol ratio, respectively), no or insignificant indane hydrogenation was observed with full or high conversions of DMDBT (depending on WHSV's) with the same product distribution.

The study may pave the way to the development of ultra-deep desulfurization catalysts that are able to bring down the operating pressure because of the direct desulfurization pathway selectivity enhancement and also remove S efficiently from refractory sulfur compounds in the presence of naphthenic and aromatic compounds. The catalysts remained stable for 3 days on stream and allowed S removal from 300 ppm (4,6-DMDBT) down to 11 ppm.

5.5. References

[1] A. Niquille-Rothlisberger, R. Prins, J. Catal. 235 (2005) 229–240.

[2] A. Ishihara, F. Dumeignil, J. Lee, K. Mitsuhashi, E. W. Qian, T. Kabe, Appl. Catal. A 289 (2005) 163–173.

[3] M. Lewandowski, P. Da Costa, D. Benichou, C. Sayag, Appl. Catal. B 93 (2010) 241–249.

[4] K.-H. Choi, N. Kunisada, Y. Korai, I. Mochida, K. Nakano, Catal. Today 86 (2003) 277–286.

[5] S. K. Bej, S. K. Maity, U. T. Turaga, Energy Fuels 18 (2004) 1227–1237.

[6] M. Houalla, D.H. Broderick, A.V. Sapre, N.K. Nag, V.H.J. de Beer, B.C. Gates, H. Kwart, J. Catal 61 (1980) 523-527.

[7] M. J. Girgis, B. C. Gates, Ind. Eng. Chem. Res. 30 (1991) 2021–2058.

[8] P. T. Vasudevan, J. L. G. Fierro, Catal. Rev.-Sci. Eng. 38 (1996) 161–188.

[9] B. C. Gates, H. Topsoe, Polyhedron 16 (1997) 3213–3217.

[10] D.D. Whitehurst, T. Isoda, I. Mochida, Adv. Catal. 42 (1998) 345–471.

[11] F. Bataille, J.-L. Lemberton, P. Michaud, G. Perot, M. Vrinat, M. Lemaire, E. Schulz, M. Breysse, S. Kasztelan, J. Catal. 191 (2000) 409–422.

[12] T. Kabe, A. Ishihara, Q. Zhang, Appl. Catal. A 97 (1993) L1-L9.

[13] V. Meille, E. Schulz, M. Lemaire, M. Vrinat, J. Catal. 170 (1997) 29–36.

[14] Y. Sun, H. Wang, R. Prins, Catal. Today, 150 (2010) 213–217.

[15] S. T. Oyama, H. Zhao, H.-J. Freund, K. Asakura, R. Włodarczyk, M. Sierka, J. Catal. 285 (2012) 1–5.

[16] D.R. Kilanowski, H. Teeuwen, B.C. Gates, V.H.J.D. Beer, G.C.A. Schuit, H. Kwart, J. Catal. 55 (1978) 129-137.

[17] Q. Zhang, W. Qian, A. Ishihara, T. Kabe, J. Jpn. Petrol. Inst. 40 (1997) 185–191.

[18] T. Kabe, K. Akamatsu, A. Ishihara, S. Otsuki, M. Godo, Q. Zhang, W. Qian, Ind. Eng. Chem. Res. 36 (1997) 5146-5152..

[19] A. B. Bjerre, E. Sorensen, Ind. Eng. Chem. Res. 31 (1992) 1577–1580.

[20] X.L. Ma, K. Sakanishi, I. Mochida, Ind. Eng. Chem. Res. 35 (1996) 2487–2494.

[21] V. Lamure-meille, E. Schulz, M. Lemaire, M. Vrinat, Appl.Catal. A 131 (1995) 143–157.

[22] M. Egorova, R. Prins, J. Catal. 225 (2004) 417–427.

[23] H. Wang, R. Prins, J. Catal. 264 (2009) 31–43.

[24] A. Niquille-Rothlisberger, R. Prins, J. Catal. 242 (2006) 207–216.

[25] I.V. Babich, J.A. Moulijn, Fuel 82 (2003) 607–631.

[26] C. Song, Catal. Today 86 (2003) 211–263.

[27] A. Niquille-Rothlisberger, R. Prins, Catal. Today 123 (2007) 198–207.

[28] H. Guo, Y. Sun, R. Prins, Catal. Today 130 (2008) 249–253.

[29] Y. Sun, R. Prins, Angew. Chem. Int. Ed. 47 (2008) 8478 –8481.

[30] T. Klimova, P. M. Vara, I. P. Lee, Catal. Today 150 (2010) 171–178.

[31] J.L. Carter, G.B. McVicker, W. Weissman, W.S. Kmak, J.H. Sinfelt, Appl. Catal. 3 (1982) 321-346.

[32] G. B. McVicker, M. Daage, M. S. Touvelle, C. W. Hudson, D. P. Klein, W. C. Baird Jr., B. R. Cook, J. G. Chen, S. Hantzer, D. E. W. Vaughan, E. S. Ellis, O. C. Feeley, J. Catal. 210 (2002) 137-148.

[33] U. Nylen, L. Sassu, S. Melis, S. Jaras, M. Boutonnet, Appl. Catal. A 299 (2006) 1-13.

[34] H. Ziaei-azad, C.-X. Yin, J. Shen, Y. Hu, D. Karpuzov, N. Semagina, J. Catal. 300 (2013) 113-124.

[35] V. Calemma, R. Giardino, M. Ferrari, Fuel Process. Technol. 91 (2010) 770–776.

[36] R. M. Navarro, B. Pawelec, J. M. Trejo, R. Mariscal, J. L. G. Fierro, J. Catal. 189 (2000) 184–194.

[37] J. L. Rousset, L. Stievano, F. J. Cadete Santos Aires, C. Geantet, A. J. Renouprez, M. Pellarin, J. Catal. 202 (2001) 163–168.

[38] H. Ziaei-Azad, N. Semagina, Appl. Catal. A 482 (2014) 327–335.

[39] Rostam J. Madon, Michel Boudart, Ind. Eng. Chem. Fundam. 21 (1982) 438–447.

[40] U. Nylen, J.F. Delgado,S. Jaras, M. Boutonnet, 262 (2004) 189–200.

[41] X. Liu, J. Phys. Chem. C 112 (2008) 5066–5073.

[42] M. Zhang, T. Yang, R. Zhao, C. Liu, Appl. Catal. A 468 (2013) 327– 333.

[43] N. Semagina, E. Joannet, S. Parra, E. Sulman, A. Renken, L. Kiwi-Minsker, Appl. Catal. A 280 (2005) 141–147.

[44] S.J. Tauster, S.C. Fung, R. L. Garten, J. Am. Chem. Soc. 100 (1978) 170–175.

[45] T. Kabe, W. Qian, Y. Hirai, L. Li, A. Ishihara, J. Catal. 190 (2000) 191–198.

[46] T.B. Lin, C.A. Jan, J.R. Chang, Ind. Eng. Chem. Res. 34 (1995) 4284–4289.

[47] M. A. Arribas, P. Concepcion, A. Martinez, Appl. Catal. A 267 (2004) 111–119.

[48] L. Piccolo, S. Nassreddine, M. Aouine, C. Ulhaq, C. Geantet, J. Catal. 292 (2012) 173–180.

[49] T.-B. Lin, C.-A. Jan, J.-R. Chanff, Ind. Eng. Chem. Res. 34 (1995) 4284-4289.

6. Concluding remarks and future works

6.1. Conclusions

The current thesis presented results on bimetallic Ir-based nanoparticles to be used as catalysts for ring opening (RO) and hydrodesulfurization (HDS) reactions. Thesis started with a hypothesis that the synergism, which is usually discussed for bimetallic catalysts can be observed through changes in activity and selectivity of bimetallic catalysts compared to their monometallic counterparts. However, a thorough explanation for this phenomenon has to be accompanied by a careful calculation of activities based on surface (and not whole) structure of catalysts. Development of such an understanding was followed as our goal through the thesis and we used a structure-controlled method to synthesize our catalysts, that allowed us to manipulate the surface structure and helped to realize the intrinsic bimetallic functioning. Concluding remarks about the materials discussed in the thesis are summarized in the following paragraphs:

Chapters 2 and 4 explained the colloid chemistry method for the structure-controlled synthesis of Ir-Pd (chapter 2) and Ir-Ni (chapter 4) nanoparticles. Various samples with two structures of alloy and core-shell have been synthesized and it was shown how the use of hydrogen during the synthesis (referred as a hydrogen-sacrificial technique) could serve to build particles with an outer shell of Ir. Formation of nanoparticles was confirmed by UV-vis analysis and TEM images indicated monodispersed nanoparticles in the range of $1.6 - 3.5$ nm. Supported catalysts were further studied with a series of characterization methods including: TPR, XPS, ISS (for Ir-Pd), XANES (Pd only), CO-DRIFTS, CO chemisorption (Ir-Pd) and CO_2-TPD (for Ir-Ni), which verified that new bimetallic particles have been formed in bimetallic catalysts and

confirmed the structural differences between catalysts of same composition but with alloy and core-shell structures. Thus, in the current thesis we successfully synthesized and characterized structured Ir-Pd and Ir-Ni bimetallic nanoparticles as well as supported catalysts. A weakly acidic material, i.e. γ-Al$_2$O$_3$, was used during the whole thesis to prepare the supported catalysts. BET results in chapter 5 indicated that the support has a mesoporous structure with pores of 4.3 nm average diameter and the pyridine adsorption analysis confirmed that acidity originated mainly from the presence of Lewis sites.

Removal of the stabilizing agent, PVP, used for the synthesis of nanoparticles was studied in chapter 3 and the CHN analysis confirmed that thermal treatment at 400°C under air is enough to completely remove the polymeric residues from the surface of active particles, although structural changes may also happen after such treatments. TEM images of supported Ir-Pd and Ir-Ni catalysts after calcination were presented in chapters 3 and 4, respectively, where it was shown that Pd and Ni suffer from sintering after exposure to 400°C, while Ir can stand such a treatment. Subsequently, bimetallic catalysts with Ir to Pd (or Ni) molar ratio of equal or higher than 1:1 as well as samples with a Pd or Ni (core)-Ir (shell) structure did not sinter after calcination at 400°C, while those rich in Pd or Ni presented size increase after the 400°C calcination.

The catalytic activity of synthesized catalysts for selective ring opening of indane was studied in chapters 2-4 to find a highly active Pt-free formulation and to realize the bimetallic functioning. In chapter 2, we explained such a functioning in Ir-Pd catalysts by calculating the activities per surface atoms referring as turnover frequency (TOF). Although activity improvements were observed in Ir-rich bimetallic catalysts compared to their monometallic counterparts, the activity values per surface atoms confirmed that Pd

mainly contributes to dilute the Ir atoms in alloy-type samples or provide 100% dispersion of Ir in the case of core-shell catalyst. Thus, we explained that despite the improvements observed in the activity of bimetallic catalysts, no intrinsic changes in the catalytic behaviour of Ir and/or Pd happened. In another words, it is the surface presence of contiguous Ir sites, which warrants the superb activity and that is why the Pd(core)-Ir(shell) supported catalyst with all Ir atoms placed on outer sites presented the highest activity amongst the Ir-Pd catalysts studied and a batch of the commercial Pt-Ir catalyst.

As was shown in chapter 3, the complete removal of PVP improves the catalytic activity; this effect was found to depend on bimetallic composition. In fact, Pd-rich samples presented a more significant jump of activity for RO of indane after complete removal of PVP residues, but those with Ir-rich composition were found to present a sluggish improvement. However, the presence of PVP residues negatively affected chemisorption of CO on all the catalysts. These results brought us to the conclusion that the removal of stabilizer needed to be considered on a case-by-case basis. It is paramount for some applications like CO chemisorption, but less pronounced for others like RO of indane.

Chapter 4 presented the catalytic activity of Ir-Ni catalysts for ring opening of indane. Similar to the results of chapter 2, Ir-rich bimetallic catalysts were found more active than their monometallic counterparts. A comparison between the activity of Ni(core)-Ir(shell) and monometallic Ir (per surface Ir) revealed that Ni also serves as a dispersing agent for Ir particles without changing their intrinsic activity. These results enabled us to suggest Ni(core)-Ir(shell) as a more economical catalyst than Pd(core)-Ir(shell) for RO of indane, which heavily relies on the hydrogenolysis activity of Ir active

sites and helped us to prove the importance of understanding the bimetallic functioning for design of highly active and cost effective catalysts.

Chapter 5 of the thesis was devoted to the study of Ir-Pd bimetallic catalysts for high-pressure HDS of 4,6-DMDBT. An increased catalytic activity and selectivity toward S-free products together were observed for bimetallic catalysts compared to their monometallic counterparts. However, activity values per surface atoms provided an interesting understanding about the bimetallic functioning. We realized that unlike the SRO of indane, Ir plays the diluting effects for Pd atoms in the HDS of 4,6-DMDBT. In fact, the severe sintering happening in Pd catalysts after calcination at 400°C leaves the catalyst with a poor dispersion, which significantly reduces the activity of Pd for HDS of 4,6-DMDBT and the main role of Ir is preventing and/or reducing the agglomeration of these Pd atoms by providing their higher dispersion. Addition of Ir to Pd was found to increase the selectivity toward S-free products and also increased the selectivity toward DDS pathway five times, which was in line with the hydrogenolysis tendency of Ir. Similar improvements were realized in high-pressure hydrogenation of indane after addition of Ir to Pd, which was discussed at the end of this chapter. Finally, we found that 4,6-DMDBT wins the competition for active sites presented on catalyst surface, when a mixture of indane and 4,6-DMDBT is co-fed to the reactor. With the same amount of catalyst and reactant concentrations in the feed, the conversion of indane drops from about 90% to almost zero over a bimetallic Pd(core)-Ir(shell) catalyst, when 300 ppm sulfur (as 4,6-DMDBT) is added to the mixture. It is mentioned here that more in depth characterization of the catalysts studied in this chapter for investigating parameters such as size changes and/or sintering at reaction conditions will be studied by next students.

In sum, in the presented thesis we studied bimetallic catalysts from an untraditional prospective and focused on a fundamental understanding about true reasons responsible for the observed activity and selectivity changes happening in bimetallic catalysts. Such a vision may contribute to the design of more efficient catalysts for different processes.

6.2. Future works

The structure-controlled synthesis of Ir-Pd and Ir-Ni bimetallic nanoparticles and their catalysis for ring opening and HDS reactions were discussed here. Chapters 2-4 concerned the ring opening of indane, while HDS of 4,6-DMDBT discussed only in chapter 5. More studies on HDS of 4,6-DMDBT using different metallic combinations is a potential future work to be planned after this thesis. Two PhD students are currently involved in such studies and other bimetallic combinations are discussed and published in future works with a vision to: i) reducing the use of noble metals, while maintaining the high catalytic activity and ii) increase the selectivity of DDS pathway, which can accommodate operating at lower pressures.

Furthermore, nanoparticles of the current study were always supported on a weak acidic material, i.e. γ-Al$_2$O$_3$, and studied in ring opening and HDS reactions. With an approach to realize the true bimetallic functioning, we used a support that was not active for either of the reaction to investigate the sole metallic function. However, support acidity and/or porosity can also affect the catalytic activity in ring opening as well as HDS studies. Thus, after realizing the bimetallic functioning in the current thesis, study of the most promising bimetallic candidates on different supports such as mesoporous zeolites, accounts as another potential future work. A PhD student is trying another support for the

ring opening of indane at this time and it is expected that such a study expanded toward the HDS of 4,6-DMDBT in the coming years.

In addition, there are several other details, which have not been studied here. Topics including: study the size effects of most promising catalysts in ring opening of indane and HDS of 4,6-DMDBT, investigation of other techniques for removal of residual polymeric stabilizers preferably at lower temperatures, study the presence of nitrogen containing molecules and/or H_2S on catalytic activity for HDS of 4,6-DMDBT, performing kinetic studies and expanding the HDS studies from one model compound to a pool of model compounds and subsequently to a real feed mixture are only few examples of the potential future works that can be planned and organized in future.

List of publications

- H. Ziaei-Azad and Natalia Semagina, "Bimetallic catalysts: requirements for stabilizing PVP removal depend on the surface composition", Journal of Applied Catalysis A: General 482 (2014) 327–335.

- J. Shen, H. Ziaei-Azad, and N. Semagina, "Is it always necessary to remove a metal nanoparticle stabilizer before catalysis?" Journal of Molecular Catalysis A: Chemical 391 (2014) 36-40.

- H. Ziaei-Azad, and Natalia Semagina, "Nickel boosts ring opening activity of iridium", ChemCatChem 6 (2014) 885–894.

- H. Ziaei-Azad, C.-X. Yin, J. Shen, Y. Hu, D. Karpuzov and N. Semagina, "Size- and structure-controlled mono- and bimetallic Ir-Pd nanoparticles in selective ring opening of indan", Journal of Catalysis 300 (2013) 113–124.

List of presentations

- H. Ziaei-Azad, J. Shen and N. Semagina, "How structure-controlled synthesis of bimetallic nanoparticles may explain observed synergism in catalysis", 23rd Canadian Symposium on Catalysis, Edmonton, Canada, May 11-14, 2014.

- H. Ziaei-Azad and Natalia Semagina, "Pd-Ir nanoparticles with controllable alloy and core/shell structures: Bimetallicity for activity enhancement", 11th European Congress on Catalysis, Lyon, France, September 1-6, 2013.

- H. Ziaei-Azad and Natalia Semagina, "Bimetallic Ni-Ir nanoparticles with controllable alloy and core/shell structures: catalytic activity for selective ring opening", 23rd North American Catalysis Society Meeting, Louisville, Kentucky, US, June 2-7, 2013.

- H. Ziaei-Azad; C.-X. Yin; J. Shen; Y. Hu; N. Semagina, "Platinum-free catalysts for selective ring opening", 62nd Canadian Chemical Engineering conference, Vancouver, Canada, October 14-17, 2012.

Works cited

This list includes all references (total of 225) cited throughout the thesis.

- A. B. Gaspar, L. C. Dieguez, Appl. Catal. A 201 (2000) 241-251.

- A. Chhabra, M.Sc. Thesis, University of Alberta, 2012.

- A. Djeddi, I. Fechete, F. Garin, Appl. Catal. A 413 (2010) 340–349.

- A. Djeddi, I. Fechete, F. Garin, Catal. Commun. 17 (2012) 173–178.

- A. Henglein, C. Brancewicz, Chem. Mater. 9 (1997) 2164–2167.

- A. Ishihara, F. Dumeignil, J. Lee, K. Mitsuhashi, E. W. Qian, T. Kabe, Appl. Catal. A 289 (2005) 163–173.

- A. J. van Dillen, R. J.A.M. Terorde, D. J. Lensveld, J. W. Geus, K. P. de Jong, J. Catal. 216 (2003) 257–264.

- A. Niquille-Rothlisberger, R. Prins, Catal. Today 123 (2007) 198–207.

- A. Niquille-Rothlisberger, R. Prins, J. Catal. 235 (2005) 229–240.

- A. Niquille-Rothlisberger, R. Prins, J. Catal. 242 (2006) 207–216.

- A. Q. Wang, C.M. Chang, C.Y. Mou, J. Phys. Chem. B 109 (2005) 18860–18867.

- A. Singh and B. D. Chandler, Langmuir 21 (2005) 10776–10782.

- A. S. Rocha, E. L. Moreno, G. P. M. da Silva, J. L. Zotin, A. C. Faro Jr, Catal. Today 133 (2008) 394–399.

- A. U. Nilekar, S. Alayoglu, B. Eichhorn, M. Mavrikakis, J. Am. Chem. Soc. 132 (2010) 7418–7428.

- B. Bjerre, E. Sorensen, Ind. Eng. Chem. Res. 31 (1992) 1574–1577.

- B. C. Gates, H. Topsoe, Polyhedron 16 (1997) 3213–3217.

- B. C. Gates, M. J. Girgis, Ind. Eng. Chem. Res. 30 (1991) 2021–2058.

- B. Coq, F. Figueras, J. Mol. Catal. A: Chem. 173 (2001) 117–134.

- B. Gehl, A. Fromsdorf, V. Aleksandrovic, T. Schmidt, A. Pretorius, J. Flege, S. Bernstorff, A. Rosenauer, J. Falta, H. Weller, M. Baumer, Adv. Funct. Mater. 18 (2008) 2398-2410.

- B. J. Hwang, C.-H. Chen, L. S. Sarma, J.-M. Chen, G.-R. Wang, M.-T. Tang, D.-G. Liu, J.-F. Lee, J. Phys. Chem. B 110 (2006) 6475-6482.

- B. J. Kip, J. Van Grondelle, J. H. A. Martens, R. Prins, Appl. Catal. 26 (1986) 353-373.

- B. Moraweck, A. J. Renouprez, E. K. Hlil, R. Baudoing-Savois, J. Phys. Chem. 97 (1993) 4288-4292.

- B. Zhao, N. Toshima, Chem. Express 5 (1990) 721–724.

- C. A. Korgel, B. A. Stowell, Nano Lett. 5 (2005) 1203–1207.

- C. Aliaga, J. Y. Park, Y. Yamada, H. S. Lee, C. K. Tsung, P. Yang, G. A. Somorjai, J. Phys. Chem. C 113 (2009) 6150–6155.

- C.-R. Bian, S. Suzuki, K. Asakura, L. Ping, N. Toshima, J. Phys. Chem. B 106 (2002) 8587–8598.

- C. G. Walter, B. Coq, F. Figueras, M. Boulet, Appl. Catal. A 133 (1995) 95–102.

- C. H. Bartholomew, R. J. Farrauto, Fundamentals of industrial catalytic processes, Wiley Interscience, Hoboken, New Jersey, (2006).

- C.-H. Jun, Y. J. Park, Y.-R. Yeon, J.-R. Choi, W.-R. Lee, S.-J. Ko, J. Cheon, Chem. Commun. 15 (2006) 1619-1621.

- C. Peniche, D. Zaldivar, M. Pazos, S. Paz, A. Bulay, J. San Roman, J. Appl. Polym. Sci. 50 (1993) 485–493.

- C. Song, Catal. Today 86 (2003) 211–263.

- D. Astruc, F. Lu, J. R. Aranzaes, Angew. Chem. Int. Ed. 44 (2005) 7872–7872.

- D. D. Whitehurst, T. Isoda, I. Mochida, Adv. Catal. 42 (1998) 345–471.

- D. G. Duff, P. P. Edwards, B. F. G. Johnson, J. Phys. Chem. 99 (1995) 15934–15944.

- D. Kubicka, M. Kangas, N. Kumar, M. Tiitta, M. Lindblad, D. Yu. Murzin, Top. Catal. 53 (2010) 1438-1445.

- D. Kubicka, N. Kumar, P. Maki-Arvela, M. Tiitta, V. Niemi, H. Karhu, T. Salmi, D. Yu. Murzin, J. Catal. 227 (2004) 313–327.

- D. Kubicka, T. Salmi, M. Tiitta, D. Yu. Murzin, Fuel 88 (2009) 366–373.

- D. R. Kilanowski, H. Teeuwen, B. C. Gates, V. H. J. D. Beer, G. C. A. Schuit, H. Kwart, J. Catal. 55 (1978) 129–137.

- D. S. Deutsch, G. Lafaye, D. Liu, B. Chandler, C. T. Williams and M. D. Amiridis, Catal. Lett. 97 (2004) 139–143.

- D. Teschner, K. Matusek, Z. Paal, J. Catal. 192 (2000) 335–343.

- D. W. Vinokur, E. I. Werst, J. Phys. Chem. B 105 (2001) 1587–1593.

- E. F. Gallei, M. Hesse and E. Schwab, in: G. Ertl, H. Knozinger, F. Schuth and J. Weitkamp (Eds.), Handbook of Heterogeneous Catalysis, Wiley-VCH, Weinheim, (2008) 57–66.

- F. Bataille, J.-L. Lemberton, P. Michaud, G. Perot, M. Vrinat, M. Lemaire, E. Schulz, M. Breysse, S. Kasztelan, J. Catal. 191 (2000) 409–422.

- F. Bernardi, J. D. Scholten, G. H. Fecher, J. Dupont, J. Morais, Chem. Phys. Lett. 479 (2009) 113-116.

- F. Bonet, V. Delmas, S. Grugeon, R. Herrera Urbina, P-Y. Silvert, K. Tekaia-Elhsissen, Nanostruct. Mater. 11 (1999) 1277–1284.

- F. Garin, P. Girard, F. Weisang, G. Maire, J. Catal. 70 (1981) 215–220.

- F. Locatelli, B. Didillon, D. Uzio, G. Niccolai, J. P. Candy, J. M. Basset, J. Catal. 193 (2000) 154-160.

- F. Luck, J. L. Schmitt, G. Maire, React. Kinet. Catal. Lett. 21 (1982) 219–224.

- F. Papa, C. Negrila, G. Dobrescu, A. Miyazaki, I. Balint, J. Nat. Gas Chem. 20 (2011) 537–542.

- F. Schuth, M. Hesse, K. K. Unger, in: G. Ertl, H. Knozinger, F. Schuth and J. Weitkamp (Eds.), Handbook of Heterogeneous Catalysis, Wiley-VCH, Weinheim, (2008) 100–119.

- F. Solymosi, J. Rasko, J. Catal. 62 (1980) 253-263.

- G. B. McVicker, M. Daage, M. S. Touvelle, C. W. Hudson, D. P. Klein, W. C. Baird Jr., B. R. Cook, J. G. Chen, S. Hantzer, D. E. W. Vaughan, E. S. Ellis, O. C. Feeley, J. Catal. 210 (2002) 137–148.

- G. B. McVicker, R. T. K. Baker, R. L. Garten, E. L. Kugler, J. Catal. 65 (1980) 207-220.

- G. C. Bond, A. F. Rawle, J. Mol. Catal. A: Chem. 109 (1996) 261−271.

- G. Diaz, F. Garin, G. Maire, S. Alerasool, R.D. Gonzalez, Appl. Catal. A 124 (1995) 33-46.

- G. G. Couto, J. J. Klein, W. H. Schreiner, D. H. Mosca, A. J. A. de Oliveira, A. J. G. Zarbin, J. Colloid Interface Sci. 311 (2007) 461-468.

- G. Poncelet, M. A. Centeno, R. Molina, Appl. Catal. A 288 (2005) 232-242.

- G. Schmid, H. West, J. O. Halm, J. O. Bovin, C. Grenthe, Chem. Eur. J. 2 (1996) 1099–1103.

- G. Schmid, N. Toshima, B. Corain (Eds.), Metal Nanoclusters in Catalysis and Material Science: The Issue of Size Control, Elsevier Science, Amesterdam (2008).

- H. B. Liu, U. Pal, J. A. Ascencio, J. Phys. Chem. C 112 (2008) 19173-19177.

- H. Bonnemann, K. S. Nagabhushana, in: G. Schmid, N. Toshima, B. Corain (Eds.). Metal Nanoclusters in Catalysis and Material Science: The Issue of Size Control, Elsevier Science, Amesterdam, (2008) 21–48.

- H. Du, C. Fairbridge, H. Yang, Z. Ring, Appl. Catal. A 294 (2005) 1–21.

- H. Guo, Y. Sun, R. Prins, Catal. Today 130 (2008) 249–253.

- H. Hirai, Y. Nakao, N. Toshima, K. Adachi, Chem. Lett. 5 (1976) 905–910.

- H. M. Chen, R. S. Liu, L. Y. Jang, J. F. Lee, S. F. Hu, Chem. Phys. Lett. 421 (2006) 118–123.

- H. R. Aduriz, P. Bodnariuk, B. Coq, F. Figueras, J. Catal. 129 (1991) 47-57.

- H. R. Reinhoudt, R. Troost, A. D. van Langeveld, S. T. Sie, J. A. R. van Veen, J. A. Moulijn, Fuel Process. Technol. 61 (1999) 133–147.

- H. Shi, O. Y. Gutierrez, G. L. Haller, D. Mei, R. Rousseau, J. A. Lercher, J. Catal. 297 (2013) 70–78.

- H. Wang, H. Tang, J. He, Q. Wang, Mater. Res. Bull. 44 (2009) 1676–1680.

- H. Wang, R. Prins, J. Catal. 264 (2009) 31–43.

- H. Zhang, N. Toshima, Appl. Catal. A 447-448 (2012) 81-88.

- H. Ziaei-azad, C.-X. Yin, J. Shen, Y. Hu, D. Karpuzov, N. Semagina, J. Catal. 300 (2013) 113-124.

- H. Ziaei-Azad, N. Semagina, Appl. Catal. A 482 (2014) 327–335.

- H. Ziaei-Azad, N. Semagina, ChemCatChem 6 (2014) 885-894.

- H.-S. Roh, K.-W. Jun, W.-S. Dong, J.-S. Chang, S.-E. Park, Y.-I. Joe, J. Mol. Catal. A: Chem. 181 (2002) 137-142.

- I. V. Babich, J. A. Moulijn, Fuel 82 (2003) 607–631.

- J. A. Horsley, J. Chem. Phys. 76 (1982) 1451-1458.

- J. Batista, A. Pintar, D. Mandrino, M. Jenko, V. Martin, Appl. Catal. A 206 (2001) 113-124.

- J. F. Moulder, W. F. Stickle, P. E. Sobol, K. D. Bomben, Handbook of X-ray Photoelectron Spectroscopy, Ulvac-Phi, Chigasaki and Physical Electronics, Minnesota, (1995).

- J. G. Van Senden, E. H. Van Broekhoven, C. T. J. Wreesman, V. Ponec, J. Catal. 87 (1984) 468–477.

- J. H. Sinfelt, Bimetallic Catalysts: Discoveries, Concepts and Applications, John Wiely & Sons, Inc., New York, (1983) 94.

- J. H. Sinfelt, Catal. Today 53 (1999) 305-309.

- J. Hagen, Industrial Catalysis: A practical approach, Wiley-VCH Weinheim, (2006).

- J. He, I. Ichinose, T. Kunitake, A. Nakao, Y. Shiraishi, N. Toshima, J. Am. Chem. Soc. 125 (2003) 11034–11040.

- J. L. Carter, G. B. McVicker, W. Weissman, W. S. Kmak, J. H. Sinfelt, Appl. Catal. 3 (1982) 327−346.

- J. L. Rousset, L. Stievano, F. J. Cadete Santos Aires, C. Geantet, A. J. Renouprez, M. Pellarin, J. Catal. 202 (2001) 163–168.

- J. Lapujoulade, K. S. Neil, Surf. Sci. 35 (1973) 288–301.

- J. M. Khurana, K. Vij, Catal. Lett. 138 (2010) 104–110.

- J. Monzo, M. T. M. Koper, P. Rodriguez, ChemPhysChem 13 (2012) 709–715.

- J. N. Kuhn, C.-K. Tsung, W. Huang and G. A. Somorjai, J. Catal. 265 (2009) 209–215.

- J.-W. Park, K. Thomas, J. V. Gestel, J.-P. Gilson, C. Collet, J.-P. Dath, M. Houalla, Appl. Catal. A 388 (2010) 37–44.

- J. Shen, Bimetallic catalysts for low pressure ring opening [M.Sc. thesis], University of Alberta, Edmonton, Canada (2011).

- J. Shen, H Ziaei-Azad, N. Semagina, J. Mol. Catal. A: Chem. 391 (2014) 36-40.

- J. Shen, X. Yin, D. Karpuzov, N. Semagina, Catal. Sci. Technol. 3 (2013) 208–221.

- J. Turkevich, P. C. Stevenson, J. Hillier, Discuss. Faraday Soc. 11 (1951) 55–75.

- J. Xian, Q. Hua, Z. Jiang, Y. Ma, W. Huang, Langmuir 28 (2012) 6736-6741.

- J. Yang, J. Y. Lee, L. X. Chen, H. P. Too, J. Phys. Chem. B 109 (2005) 5468–5472.

- J. Zielinski, J. Mol. Catal. 83 (1993) 197-206.

- K. J. Leary, J. N. Michaels, AlChE J. 34 (1988) 263-271.

- K. Nagaveni, A. Gayen, G. N. Subbanna, M. S. Hegde, J. Mater. Chem. 12 (2002) 3147–3151.

- K. S. Kim, A. F. Gossmann, N. Winograd, Anal. Chem. 46 (1974) 197-200.

- L. Cademartiri, A. Ghadimi, G. A. Ozin, Acc. Chem. Res. 41 (2008) 1820–1830.

- L. D. Pachon, M. B. Thathagar, F. Hartl, G. Rothenberg, Phys. Chem. Chem. Phys. 8 (2006) 151-157.

- L. DSouza, S. Sampath, Langmuir 16 (2000) 8510-8517.

- L. Guczi, A. Beck, A. Horvath, Z. Koppany, G. Stefler, K. Frey, I. Sajo, O. Geszti, D. Bazin, J. Lynch, J. Mol. Catal. A: Chem. 204 (2003) 545–552.

- L. Guczi, Z. Schay, Gy. Stefler, L. F. Liotta, G. Deganello, A. M. Venezia, J. Catal. 182 (1999) 456−462.

- L. M. Bronstein, D. M. Chernyshov, I. O. Volkov, M. G. Ezernitskaya, P. M. Valetsky, V. G. Matveeva, E. M. Sulman, J. Catal. 196 (2000) 302–314.

- L. Piccolo, S. Nassreddine, M. Aouine, C. Ulhaq, C. Geantet, J. Catal. 292 (2012) 173–180.

- L. Qiu, F. Liu, L. Zhao, W. Yang, J. Yao, Langmuir 22 (2006) 4480-4482.

- M. A. Arribas, P. Concepcion, A. Martinez, Appl. Catal. A 267 (2004) 111–119.

- M. Booth, J. G. Buglass, J. F. Unsworth, Top. Catal. 16/17 (2001) 39–46.

- M. Cai, J. Wen, W. Chu, X. Cheng, Z. Li., J. Nat. Gas Chem. 20 (2011) 318-324.

- M. Egorova, R. Prins, J. Catal. 225 (2004) 417–427.

- M. Houalla, D.H. Broderick, A. V. Sapre, N. K. Nag, V. H. J. de Beer, B. C. Gates, H. Kwart, J. Catal. 61 (1980) 523–527.

- M. J. Girgis, B. C. Gates, Ind. Eng. Chem. Res. 30 (1991) 2021–2058.

- M. Kangas, D. Kubicka, T. Salmi, D. Y. Murzin, Top. Catal. 53 (2010) 1172-1175.

- M. Lewandowski, P. Da Costa, D. Benichou, C. Sayag, Appl. Catal. B 93 (2010) 241–249.

- M. Liu, W. Yu, H. Liu, J. Zheng, J. Colloid Interface Sci. 214 (1999) 231–237.

- M. Mihaylov, T. Tsoncheva, K. Hadjiivanov, J. Mater. Sci. 46 (2011) 7144-7151.

- M. W. Roberts, Catal. Lett. 67 (2000) 1–70.

- M. Wu, D. M. Hercules, J. Phys. Chem. 83 (1979) 2003-2008.

- M. Zhang, T. Yang, R. Zhao, C. Liu, Appl. Catal. A 468 (2013) 327– 333.

- N. S. Babu, N. Lingaiah, R. Gopinath, P. S. S. Reddy, P. S. S. Prasad, J. Phys. Chem. C 111 (2007) 6447-6453.

- N. Semagina, E. Joannet, S. Parra, E. Sulman, A. Renken, L. Kiwi-Minsker, Appl. Catal., A 280 (2005) 141-147.

- N. Semagina, L. Kiwi-Minsker, Catal. Rev. 51 (2009) 147–217.

- N. Semagina, X. Yin, J. Shen, K. Loganathan, US Patent, 2013, No. US-2013-0248414-A1.

- N. Sheppard, C. D. L. Cruz, Catal. Today 70 (2001) 3-13.

- N. Toshima, H. Yan, Y. Shiraishi, in: G. Schmid, N. Toshima, B. Corain (Eds.). Metal Nanoclusters in Catalysis and Material Science: The Issue of Size Control, Elsevier Science, Amesterdam, (2008) 49–75.

- N. Toshima, K. Hirakawa, Appl. Surf. Sci. 121 (1997) 534–537.

- N. Toshima, K. Hirakawa, Polym. J. 31 (1999) 1127-1132.

- N. Toshima, M. Harada, T. Y. K. Kushibashi, K. Asakura, J. Phys. Chem. 95 (1991) 1448-1453.

- N. Toshima, M. Harada, T. Yonezawa, K. Kushihashi, K. Asakura, J. Phys. Chem. 95 (1991) 7448–7453.

- N. Toshima, M. Kanemaru, Y. Shiraishi, Y. Koga, J. Phys. Chem. B 109 (2005) 16326–16331.

- N. Toshima, Pure Appl. Chem. 72 (2000) 317-325.

- N. Toshima, T. Yonezawa, K. Kushihash, J. Chem. Soc., Faraday Trans. 89 (1993) 2537–2543.

- N. Toshima, Y. Shiraishi, A. Shiotsuki, D. Ikenaga, Y. Wang, Eur. Phys. J. D, 16 (2001) 209–212.

- N. Toshima, Y. Shiraishi, T. Teranishi, M. Miyake, T. Tominaga, H. Watanabe, W. Brijoux, H. Bonnemann, G. Schmid, Appl. Organomet. Chem. 15 (2001) 178–196.

- N. Toshima, Y. Wang, Langmuir 10 (1994) 4574–4580.

- O. Terekhina, E. Roduner, J. Phys. Chem. C 116 (2012) 6973-6979.

- P. Lu, N. Toshima, Bull. Chem. Soc. Jpn. 73 (2000) 751–758.

- P. Lu, T. Teranishi, K. Asakura, M. Miyake, N. Toshima, J. Phys. Chem. B 103 (1999) 9673–9682.

- P. Samoila, M. Boutzeloit, C. Especel, F. Epron, P. Marecot, Appl. Catal. A 369 (2009) 104-112.

- P. Samoila, M. Boutzeloit, C. Especel, F. Epron, P. Marecot, J. Catal. 276 (2010) 237-248.

- P. Sonstrom, B. Jurgens, S. Tambou Djakpou, B. Ritz, K. Ahrenstorf, G. Grathwohl, H. Weller and M. Baumer, Catal. Sci. Technol. 1 (2011) 830–838.

- P. Sonstrom, D. Arndt, X. Wang, V. Zielasek and M. Baumer, Angew. Chem., Int. Ed. 50 (2011) 3888–3891.

- P. Sonstrom, M. Baumer, Phys. Chem. Chem. Phys. 13 (2011) 19270–19284.

- P. T. Do, W. E. Alvarez, D. E. Resasco, J. Catal. 238 (2006) 477–488.

- P. T. Vasudevan, J. L. G. Fierro, Catal. Rev.-Sci. Eng. 38 (1996) 161–188.

- Q. Zhang, W. Qian, A. Ishihara, T. Kabe, J. Jpn. Petrol. Inst. 40 (1997) 185–191.

- R. C. Santana, P. T. Do, M. Santikunaporn, W. E. Alvarez, J. D. Taylor, E. L. Sughrue, D. E. Resasco, Fuel 85 (2006) 643–656.

- R. F. Hampson, Jr., R. F. Walker, J. Res. Natl. Bur. Stand. 66A (1962) 177-178.

- R. F. Hampson, Jr., R. F. Walker, J. Res. Natl. Bur. Stand., Sect. A. 65A (1961) 289-295.

- R. Huang, Y.-H. Wen, Z.-Z. Zhu, S.-G. Sun, J. Phys. Chem. C 116 (2012) 8664-8671.

- R. J. Cvetanovic, Y. Amenomiya, Advan. Catal. 17 (1967) 103-149.

- R. J. Madon, M. Boudart, Ind. Eng. Chem. Fundam. 21 (1982) 438–447.

- R. L. Garten, J. H. Sinfelt, J. Catal. 62 (1980) 127-139.

- R. M. Navarro, B. Pawelec, J. M. Trejo, R. Mariscal, J. L. G. Fierro, J. Catal. 189 (2000) 184–194.

- R. M. Rioux, H. Song, J. D. Hoefelmeyer, P. Yang, G. A. Somorjai, J. Phys. Chem. B 109 (2005) 2192–2202.

- R. M. Rioux, H. Song, M. Grass, S. Habas, K. Niesz, J. D. Hoefelmeyer, P. Yang, G. A. Somorjai, Top. Catal. 39 (2006) 167–174.

- R. Moraes, K. Thomas, S. Thomas, S. V. Donk, G. Grasso, J.-P. Gilson, M. Houalla, J. Catal. 286 (2012) 62-77.

- R. Nyholm, A. Berndtsson, N. Martensson, J. Phys. C: Solid State Phys. 13 (1980) L1091-L1096.

- R. Shafi, G. J. Hutchings, Catal. Today 59 (2000) 423–442.

- R. V. Hardeveld, F. Hartog, Surf. Sci. 15 (1969) 189-230.

- S. Bhlapibul, K. Pruksathorn, P. Piumsomboon, Renewable Energy 41 (2012) 262–266.

- S. C. Yang, N. Chen, P. Nash, Ir-Ni Phase Diagram, ASM Alloy Phase Diagrams Center, P. Villars, editor-in-chief; H. Okamoto and K. Cenzual, section editors;

http://www1.asminternational.org/AsmEnterprise/APD, ASM International, Materials Park, OH, 2006.

- S. Dokjampa, T. Rirksomboon, D. T. M. Phuong, D. E. Resasco, J. Mol. Catal. A: Chem. 274 (2007) 231–240.

- S. J. Cho, R. Ryoo, Catal. Lett. 97 (2004) 71–75.

- S. J. Cho, S. K. Kang, Catal. Today 93 (2004) 561–566.

- S. J. Tauster, S. C. Fung, R. L. Garten, J. Am. Chem. Soc. 100 (1978) 170-175.

- S. K. Bej, S. K. Maity, U. T. Turaga, Energy Fuels 18 (2004) 1227–1237.

- S. K. Ghosh, M. Mandal, S. Kundu, S. Nath, T. Pal, Appl. Catal. A 268 (2004) 61–66.

- S. K. Matam, E. H. Otal, M. H. Aguirre, A. Winkler, A. Ulrich, D. Rentsch, A. Weidenkaff, D. Ferri, Catal. Today 184 (2012) 237-244.

- S. K. Singh, Q. Xu, Chem. Commun. 46 (2010) 6545–6547.

- S. Lecarpentier, J. V. Gestel, K. Thomas, J.-P. Gilson, M. Houalla, J. Catal. 254 (2008) 49–63.

- S. Link, M. A. El-Sayed, J. Phys. Chem. B 103 (1999) 8410-8426.

- S. O. Blavo, E. Qayyum, L. M. Baldyga, V. A. Castillo, M. D. Sanchez, K. Warrington, M. A. Barakat, J. N. Kuhn, Top. Catal. 56 (2013) 1835–1842.

- S. Subramanian, J. A. Schwarz, Appl. Catal. 74 (1991) 65-81.

- S. T. Oyama, H. Zhao, H.-J. Freund, K. Asakura, R. Włodarczyk, M. Sierka, J. Catal. 285 (2012) 1–5.

- T. B. Lin, C. A. Jan, J. R. Chang, Ind. Eng. Chem. Res. 34 (1995) 4284–4289.

- T. C. Deivaraja, J. Y. Lee, J. Electrochem. Soc. 151 (2004) A1832–A1835.

- T. Endo, T. Kuno, T. Yoshimura, K. Esumi, J. Nanosci. Nanotechol. 5 (2005) 1875–1882.

- T. Endo, T. Yoshimura, K. Esumi, J. Colloid Interface Sci. 286 (2005) 602–609.

- T. Kabe, A. Ishihara, Q. Zhang, Appl. Catal. A 97 (1993) L1–L9.

- T. Kabe, K. Akamatsu, A. Ishihara, S. Otsuki, M. Godo, Q. Zhang, W. Qian, Ind. Eng. Chem. Res. 36 (1997) 5146–5152.

- T. Kabe, W. Qian, Y. Hirai, L. Li, A. Ishihara, J. Catal. 190 (2000) 191–198.

- T. Klimova, P. M. Vara, I. P. Lee, Catal. Today 150 (2010) 171–178.

- T. Miyake, M. Teranishi, Chem. Mater. 10 (1998) 594-600.

- T. O. Hutchinson, Y. P. Liu, C. Kiely, C. J. Kiely and M. Brust, Adv. Mater. 13 (2001) 1800–1803.

- T. Teranishi, M. Hosoe, T. Tanaka, M. Miyake, J. Phys. Chem. B 103 (1999) 3818-3827.

- T. Teranishi, M. Miyake, Chem. Mater. 10 (1998) 594–600.

- U. Nylen, B. Pawelec, M. Boutonnet, J. L. G. Fierro, Appl. Catal. A 299 (2006) 14-29.

- U. Nylen, J. F. Delgado, S. Jaras, M. Boutonnet, Appl. Catal. A 262 (2004) 189–200.

- U. Nylen, L. Sassu, S. Melis, S. Jaras, M. Boutonnet, Appl. Catal. A 299 (2006) 1–13.

- V. Calemma, R. Giardino, M. Ferrari, Fuel Process. Technol. 91 (2010) 770–776.

- V. I. Severin, A. V. Tseplayaeva, N. E. Khandamirova, Y. A. Priselkov, N. A. Chernova, l. V. Golubtsov, V. B. Lukyanov, Mendeleev Commun. 2 (1992) 97-100.

- V. Lamure-meille, E. Schulz, M. Lemaire, M. Vrinat, Appl. Catal. A 131 (1995) 143–157.

- V. Meille, E. Schulz, M. Lemaire, M. Vrinat, J. Catal. 170 (1997) 29–36.

- W. Chen, J. Kim, S. Sun and S. Chen, Phys. Chem. Chem. Phys. 8 (2006) 2779–2786.

- W. E. Alvarez, D. E. Resasco, J. Catal. 164 (1996) 467–476.

- W.-R. Lee, M. G. Kim, J.-R. Choi, J.-I. Park, S. J. Ko, S. J. Oh, J. Cheon, J. Am. Chem. Soc 127 (2005) 16090-16097.

- W. Yu, M. D. Porosoff, J. G. Chen, Chem. Rev. 112 (2012) 5780−5817.

- X. Fu, Y. Wang, N. Wu, L. Gui and Y. Tang, J. Colloid Interface Sci. 243 (2001) 326–330.

- X. Huang, Y. Wang, X. Liao, B. Shi, Chem. Commun. 5 (2009) 4687-4689.

- X. L. Ma, K. Sakanishi, I. Mochida, Ind. Eng. Chem. Res. 35 (1996) 2487–2494.

- X. Liu, J. Phys. Chem. C 112 (2008) 5066–5073.

- X. Wang, P. Sonstrom, D. Arndt, J. Stover, V. Zielasek, H. Borchert, K. Thiel, K. Al-Shamery and M. Baumer, J. Catal. 278 (2011) 143–152.

- X. Wang, W. B. Yue, M. S. He, M. H. Liu, J. Zhang, Z. F. Liu, Chem. Mater. 16 (2004) 799–805.

- X. Yan, H. Liu, K. Y. Liew, J. Mater. Chem. 11 (2001) 3387–3391.

- X. Zuo, H. Liu, C. Yue, J. Mol. Catal. A: Chem. 147 (1999) 63-72.

- Y. Borodko, S. M. Humphrey, T. D. Tilley, H. Frei, G. A. Somorjai, J. Phys. Chem. C 111 (2007) 6288-6295.

- Y. Chen, F. Yang, Y. Dai, W. Wang, S. Chen, J. Phys. Chem. C 112 (2008) 1645–1649.

- Y. Chen, K. Y. Liew, J. Li, Mater. Lett. 62 (2008) 1018–1021.

- Y.-J. Huang, J. Xue, J.A. Schwarz, J. Catal. 111 (1988) 59-66.

- Y.-J. Huang, S. C. Fung, W. E. Gates, G. B. McVicker, J. Catal. 118 (1989) 192-202.

- Y. I. Vesnin, A. V. Nikolaev, Y. V. Shubin, S. V. Korenev, Ir-Pd Phase Diagram, ASM Alloy Phase Diagrams Center, P. Villars, editor-in-chief; H. Okamoto and K. Cenzual, section editors; http://www1.asminternational.org/AsmEnterprise/APD, ASM International, Materials Park, OH, (2006).

- Y. Lou, M. M. Maye, L. Han, J. Luo, C.-J. Zhong, Chem. Commun. 5 (2001) 473–474.

- Y. Mizukoshi, T. Fujimoto, Y. Nagata, R. Oshima, Y. Maeda, J. Phys. Chem. B 104 (2000) 6028–6032.

- Y. Sun, H. Wang, R. Prins, Catal. Today 150 (2010) 213–217.

- Y. Sun, R. Prins, Angew. Chem. Int. Ed. 47 (2008) 8478–8481.

- Y. Wang, N. Toshima, J. Phys. Chem. B 101 (1997) 5301–5306.

- Y. Zhao, X. Yang, J. Tian, F. Wang, L. Zhan, Int. J. Hydrogen Energy 35 (2010) 3249–3257.

- Z. D. Wei, Y. C. Feng, L. Li, M. J. Liao, Y. Fu, C. X. Sun, Z. G. Shao, P. K. Shen, J. Power Sources 180 (2008) 84-91.

- Z. L. Wang, J. M. Petroski, T. C. Green, M. A. El-Sayed, J. Phys. Chem. B 102 (1998) 6145–6151.